Finite Element Modelling of CFFT Small-Scale Wind Turbine Towers

YIKAI GONG

Thesis submitted to the University of Ottawa
in partial Fulfillment of the requirements for the
degree of Master of Applied Science in Civil Engineering

Department of Civil Engineering
Faculty of Engineering
University of Ottawa

Abstract

Wind energy has emerged as a promising and renewable solution to reduce reliance on fossil fuels in remote off-grid locations. Conventional wind turbine towers are made from concrete or steel, which present several significant drawbacks in certain applications. The use of lightweight and corrosion-resistant fibre reinforced polymer (FRP) tubes as permanent structural formwork can mitigate these challenges. Existing literature has highlighted the performance of concrete-filled FRP tubes (CFFTs) through experiments and successful applications in the field. However, only a few cantilever CFFTs have been tested, and their sizes were much smaller than required for wind turbine towers. In consequence, this thesis focuses on relatively large cantilever CFFTs at a scale representative of small wind turbine towers. The finite element (FE) method was adopted to simulate the behaviour of CFFT towers using the commercial software ABAQUS.

The first part of this thesis presents the development and validation of CFFT FE models under bending and axial loading conditions, as well as hollow FRP tubes under bending. The models were compared to experimental results reported by Fam (2000) to ensure the selection of appropriate material properties. Good agreements were observed, and the accuracy of the FE modelling approach was proved.

Subsequently, a parametric study was conducted to explore the feasibility of CFFTs for wind turbine towers. The analyses of cantilever towers with different geometric properties and reinforcement configurations under concentrated lateral load were performed first. Then, a cantilever CFFT tower under different loading configurations was tested. It is noted that towers subjected to concentrated load had the lowest load capacity and stiffness. Conclusions were made that with or without axial load, lateral load eccentricity does not affect the behaviour of cantilever CFFTs significantly. Meanwhile, the increase in height-to-diameter ratio decreases the load capacity and stiffness of cantilever CFFTs.

Finally, the CFFT tower results were compared with concrete and steel tubular models with similar geometry. The results suggest that CFFTs have better overall performance than the other two types of towers. They are also superior with respect to flexibility in installation and their durability.

Dedication

To my family for their love and patience throughout the years. To those who encouraged and supported me over the past two years.

Acknowledgements

I would like to first express my sincere thanks to my supervisor, Dr. Martin Noel, for his patience, guidance, and enthusiasm in the process. Without his help and advice this project would not be a success. His support and guidance are significant in the process and helped me in overcoming all the difficulties in the period.

I would also like to thank my friends for their support and encourage during the two years, and their inspiring ideas on the project.

Last but not least, I would like to thank my family for their support and understanding during the two years.

Table of Contents

List of Tables

List of Figures

Chapter 1 Introduction

1.1 General

Wind energy is a growing source of renewable energy in Canada and globally. The energy in wind is converted to electricity using wind turbines. Many communities in the Canadian North continue to rely on unreliable diesel energy and require new sustainable distributed energy solutions. Considering the cost, the installation, the maintenance, and the demand of off-grid electricity, small-scale wind turbines are more useful in remote areas than medium- or large-scale wind turbines. The wind turbine tower is an important component that can significantly affect the constructability and feasibility of wind energy systems, especially in remote areas. Existing wind turbine towers are made of steel or concrete, each of which presents certain drawbacks related to fabrication, transportation, performance, or durability. Concrete-filled fibre-reinforced polymer tubes (CFFTs) present a promising alternative that can be used to improve the behaviour and constructability of wind turbine towers.

Fibre-reinforced polymer (FRP) material has higher tensile strength, lighter weight, and better corrosion resistance than concrete and steel materials. FRP tubes can be used as structurally integrated permanent formwork and filled with concrete to produce an efficient and cost-effective composite structural system that is simple to manufacture. Compared to conventional steel reinforcement, they can also prevent the spalling of the concrete core and provide better confinement, as well as improved durability performance. CFFTs have been previously used in different structures such as piles, bridge girders, and overhead sign structures; however, their use for wind turbine towers has not yet been extensively studied.

Many experiments have been conducted to study the behaviour and failure modes of CFFTs. The tests considered different parameters but were mostly performed under concentric or eccentric axial loads or four-point bending conditions. The time and cost of CFFT tests is considerable due to the long manufacturing process and high FRP material price, especially when the CFFT is large. Wind turbine towers are often higher than 10 m, making them impractical to test in a conventional laboratory. Simulated wind testing requires special facilities and is very expensive. There are not enough studies about large CFFTs, so a large number of variable values of tube geometric shapes and loading conditions need to be tested. Therefore, the use of the finite element analysis method is a useful alternative to experimental studies to understand the performance of large CFFTs.

The finite element method has been used by many researchers to study the performance of different CFFTs. Results obtained using finite element analyses have been validated by experimental results, confirming the reliability of the finite element method. Compared to experimental testing, finite element analysis can provide more details and investigate a wider range of parameters; hence, the financial and time benefits of numerical studies are obvious. Once a reliable model is developed and validated using experimental data, more simulations can be conducted using the same or a similar model, thus improving the effectiveness, and reducing the time and cost.

This study employs the finite element analysis method to study the performance of large CFFTs with and without steel reinforcing bars and prestressing tendons with different geometric details in order to explore the feasibility of CFFTs for small-scale wind turbine towers. A wide range of parameters are considered, including the influence of load scenarios. The conclusions made from this research are used to provide suggestions for the further design and experiments on CFFT wind turbine towers.

1.2 Research scope and objectives

The primary objective of this research was to study the influence of geometric shape, reinforcement configuration, and load scenarios on CFFT wind turbine towers using finite element analysis. Commercial software ABAQUS was adopted to develop the models and conduct analysis. A model validation was first completed by modelling two hollow tubes, four CFFT beams, and four CFFT compression stubs tested by Fam (2000) The models were calibrated to obtain more accurate results. In this progress, different modelling methods and constitutive material models were used and compared, and suitable approaches were adopted in the modelling of CFFT wind turbine towers. Subsequently, a parametric study was developed to compare the behaviour of various CFFT wind turbine tower designs, as well as concrete and steel wind turbine tower models. Although wind loading is transient in nature, it is common practice to use equivalent static loads for design purpose; hence, in this study, dynamic wind effects (including modes of vibration and resonance frequencies) are neglected and static loading is assumed to be representative of overall performance.

The specific objectives of this research include the following:

1. Perform model validation to prove finite element analysis is a reliable and effective method to test the behaviour of CFFTs.
2. Choose the suitable material constitutive models for CFFTs during the model validation.
3. Study the influence of geometric shapes and reinforcement configurations on CFFT wind turbine tower models.
4. Study the influence of load distribution on CFFT wind turbine tower models.
5. Study the load capacity and failure modes of concrete wind tower models.
6. Study the load capacity and failure modes of steel tubular wind tower models.
7. Study the performance of CFFT wind turbine tower models under combined loads.

1.3 Thesis organization

This thesis is organized into five chapters in the following structure:

- Chapter 2 is the literature review. It presents the necessity and advantages of using wind energy and developing small-scale wind turbine in remote areas, as well as the current development, design limits, and loading conditions of wind turbine tower. This chapter also presents the background information and literature on the CFFTs, including the history, the application, the advantages, and the disadvantages of CFFTs compared to conventional reinforced concrete. The experimental tests conducted by different researchers, the results of the influence of different parameters on CFFTs in axial, bending, or composite loading conditions, and the new developments in the CFFT field are all mentioned in this chapter.
- Chapter 3 is the model validation. In this chapter, finite element models developed using commercial software ABAQUS are compared to experimental results reported in literature. It presents the material properties, specimen geometric details, test setups, and results of experiments of hollow tubes, CFFT beams, and CFFT stubs in bending and axial loading conditions. This chapter also provides the constitutive models, finite element modelling method, developed models, and results of finite element analysis.
- Chapter 4 is the parametric study. This chapter presents the constitutive models and finite element type and interaction used during the modelling of CFFT, concrete, and steel wind

turbine towers. It also provides the different geometric shapes and load scenarios of tested models. The influence of tower height, tower diameter, FRP wall thickness, FRP orientation, concrete filling ratio, steel reinforcement ratio, number of prestressing tendons, and taper ratio are discussed in this chapter, as well as the results of selected wind turbine tower models tested under axial, horizontal, and combined load. Models for concrete and steel tubular wind turbine towers also compared to the performance of CFFT wind turbine towers.

- Chapter 5 presents the conclusions and future work. This chapter presents the conclusions of results obtained in Chapter 3 and 4 and possible future work about CFFT wind turbine towers.

Chapter 2 Literature review

2.1 Wind power

Global demand for energy keeps increasing; energy needs are projected to grow nearly 50% between 2008 and 2050 (Capuano, 2019). Increasing the use of renewable energies is a good method to meet the demand. Fossil fuels are non-renewable resources, and therefore their use is not sustainable; meanwhile, renewable energy sources do not produce greenhouse gases like fossil fuels, so they will not cause air pollution and climate change. Wind power is one of the most widely used renewable energy sources all over the world and is still one of the fastest-growing renewable energy technologies in the world and in Canada (Natural Resources, 2017).

In Canada, over 200,000 individuals are living in one of nearly 300 remote communities. These remote communities located in B.C., northern Ontario, northern Quebec (Nunavik), northern Labrador (Nunatsiavut), Yukon, the Northwest Territories, and Nunavut are not connected to the main North American electricity grid, so they lack access to reliable and affordable electricity and need to produce electricity locally. Typically, they are dependent on diesel-powered generation facilities, which means the electricity costs are much higher and the air pollution caused by diesel-powered generators may harm the environment and affect the health of local residents. The electricity rate in remote areas is higher than the Canadian average due to the poor economies of scale, high operational costs, high transportation costs for diesel fuel, high diesel storage costs, and fluctuating diesel fuel price (Knowles, 2016). In those areas, wind power can be a good replacement to diesel energy.

The power of a large-scale wind power generation system is higher than 1000 kW; the power of a medium-scale wind power generation system is between 100 and 1000 kW; the power of a small-scale wind power generation system is lower than 100 kW (Chen et al., 2021).

Unlike medium- and large-scale wind turbines which are often used in wind farms by power producers, small-scale wind turbines are much smaller in size. They can either connect to the electricity grid or be installed off-grid, so they can be used in remote areas to reduce the use of diesel generators and the fuel costs (Shafiei et al., 2016). Moreover, small-scale wind turbines have a simpler structure, are easier to install and control, which means they are more cost-effective than medium- or large-scale wind turbines (Chen et al., 2021).

2.1.1 Wind turbine towers

Wind turbine towers are often made of steel tubes (Fig. 2.1) or concrete (Fig. 2.2). Tubular steel towers are aesthetically pleasing and can be easily fabricated compared to lattice towers comprised of truss elements. Lattice towers are also less appropriate for remote areas since they are likely to require more regular maintenance. Steel tubular towers have high tensile strength and are ductile. Benefits of concrete towers include a longer life span of 40-60 years, and the construction and transportation cost of concrete towers are lower than those of steel towers. However, conventional wind turbine towers also have disadvantages. Steel tubular towers can be very expensive due to the material price, and the transportation of the towers are a significant challenge; for this reason, the maximum base diameter of steel tubes is limited. Steel towers only have a 20-year life span, which is extremely short. Moreover, the corrosion resistance and the operation and maintenance costs during the service life are predicted to be higher than for concrete towers. Concrete towers, on the other hand, are heavier than steel tubular towers, require a larger foundation, and require reinforcement to resist bending stresses as they are weak in tension (de Lana et al., 2021; Veljkovic et al., 2011).

To overcome these disadvantages, concrete-filled FRP tubes (CFFTs) are considered to be a possible alternative to conventional steel tubular and concrete towers that can be prefabricated and are lighter than concrete towers. In addition to acting as a permanent formwork for the concrete, the lightweight outer FRP tube ensures that CFFTs have a good tensile behaviour and are suitable for flexural loading. The tubes can also be used to facilitate segmental construction to simplify transportation and erection of the towers. Compared to steel, FRP material is corrosion resistant and hence it can resist harsh weathering conditions, which means the maintenance costs would be lower, and the life span of the towers can be longer (Burgoyne, 2009; Van Den Einde et al., 2003).

Figure 2.1 Steel tubular tower (Veljkovic et al., 2011)

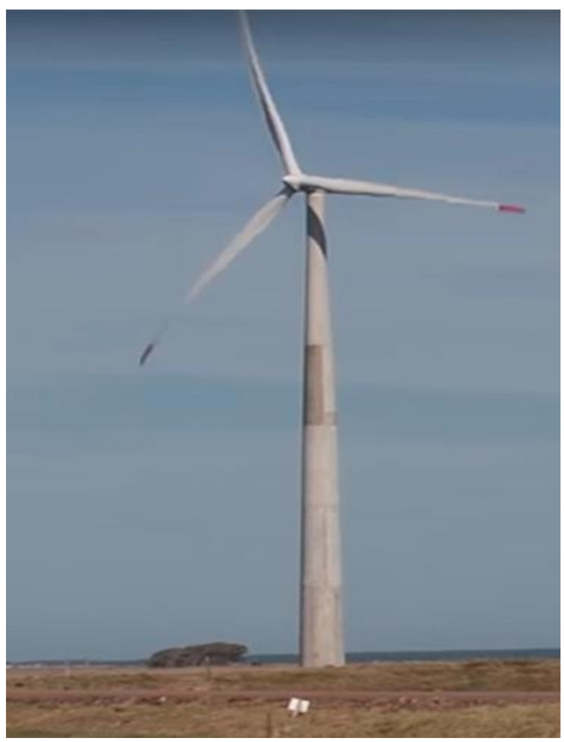

Figure 2.2 Concrete tower (*ACCIONA*, n.d.)

2.1.2 Wind turbine tower design limits

Most available wind turbine tower design guidelines are based on steel, concrete, or latticed towers. While designing wind turbine towers, several parameters should be taken into consideration. There are a limited number of design guidelines available to assist designers in this process.The International Electrotechnical Commission (IEC) Wind Turbine Requirements document 61400-1 (2019) introduces the wind conditions and loads and load cases, and IEC 61400-2 is a simplified standard for small wind turbines. They are international standards and were first developed in 2001. ANSI/TIA 222-G (2005) is developed by the American National Standard Institute, and is not specified for wind turbines, but it provides the analysis/design procedure of steel poles which can be used to design latticed towers. DNVGL-ST-0126 (2016) is a standard for support structures for wind turbines, including concrete structures and steel structures, and was first developed in 2014 by a company that provides technical consultancy and oversight to the global renewable energy sector named Det Norske Veritas (Norway) and Germanischer Lloyd (Germany).

The design limits of wind turbine towers discussed in various design documents include the outer diameter and top deflection. The outer diameter depends primarily on the transportation limitations, while the top lateral deflection is sometimes limited by the manufacturer. In a previous study, the outer diameter was limited to 4.5 m, and the top lateral deflection was limited to 1.25% of the tower height in order to avoid damage (Nicholson, 2011).

2.1.3 Wind turbine tower loads

Wind turbine tower loading consists of four parts: loads from the wind turbine itself, wind load, self-weight, and internal fixtures loading.

Loads from the wind turbine are applied at the top of the tower and can be obtained from the wind turbine manufacturers. In commercial areas, medium- and large-scale wind turbines are more widely used; when it comes to off-grid or battery charging wind turbines, small-scale wind turbines under 5 kW are more efficient. Table 2.1 presents the weight and power rating of battery charging off-grid small wind turbines. Figure 2.3 shows the different rotor diameter, tower height, and total height of different sizes of wind turbine towers (Rhoads-Weaver et al., 2013). Figure 2.4 illustrates the 3-D forces at the top of the tower, in which T_T and M_{RT} represent the torsional and bending moments, F_{vT} and F_{hT} represent the vertical and horizontal forces. Figure 2.5 presents the 2-D forces along the height of the tower, in which w_v is the vertical distributed load calculated by self weight and internal fixtures, and w_h is the horizontal distributed load due to wind force (Nicholson, 2011).

Table 2.1 Different weights and sizes of small wind turbines

Size (W)	200	500	1000	2000	3000	5000
Weight (kg)	10	28	60	125	138	380

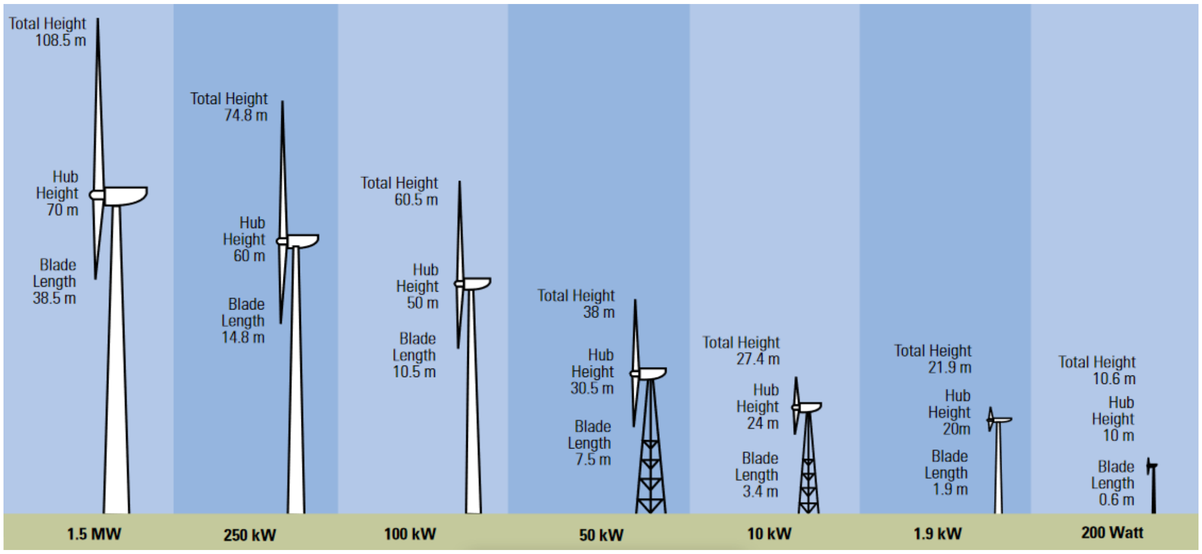

Figure 2.3 Different sizes of wind turbines (Rhoads-Weaver et al., 2013)

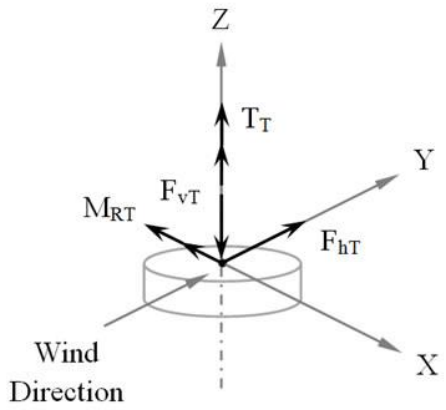

Figure 2.4 3-D forces at the top of the tower (Nicholson, 2011)

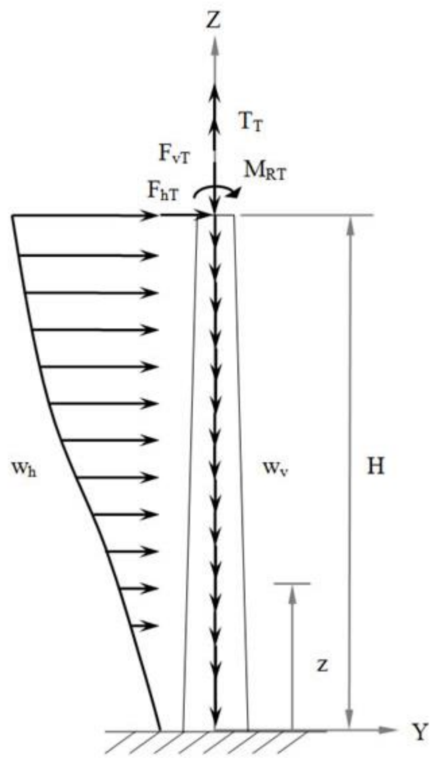

Figure 2.5 Loads applied on the wind turbine tower (Nicholson, 2011)

In this study, loads for small wind turbines were calculated using a simple method provided by IEC 61400-2. This method can be used on small wind turbines satisfying the following requirements:

- Having horizontal axis
- Having 2 or more blades
- Having a rigid hub
- Having cantilever blades

Other parameters such as downwind or upwind rotor, furling or no furling, and variable or constant speed are not restricted by this method.

Six different design situations and ten load cases are considered in this method. Loads at the blade root and shaft of the wind turbine are provided according to some basic wind turbine parameters such as blade and shaft areas and the number of blades, but loads provided at the tower are not specified in one equation, so results at blade root and shaft are calculated to find loads applied on the tower. In a previous study, researchers found that load case D (maximum thrust), load case H (parked wind load), and load case I (parking wind loading, maximum exposure) are most likely to provide the largest load for the wind turbine tower, since compared to the braking torque and moments due to other conditions, the bending moment produced by the horizontal axial-load is more significant (Gwon, 2011). Load case D is calculated under power production situation, load case H is calculated when the parked wind turbine is idling or standstill, and load case I is related to parked wind turbine under fault conditions. As a result, in this study, load case I is ignored; only load case D and load case H are considered.

For load case D, the ultimate shaft thrust load, $F_{x-shaft}$, is calculated using the following equation:

$$F_{x-shaft} = C_T \frac{1}{2} \rho (2.5 V_{ave})^2 A \tag{2.1}$$

In which C_T is the thrust coefficient that is considered to be 0.5 in this equation, ρ is the density of air, which is taken as 1.225 kg/m^3, V_{ave} is the average wind speed, and A is the rotor swept area.

For load case H, survival wind is considered, and no fault is applied. The horizontal drag force, $F_{x-shaft}$, is calculated via the following equation:

$$F_{x-shaft} = C_d \frac{1}{2} \rho V_{e50}^2 (A_{proj,B} B) \tag{2.2}$$

In which C_d is the drag coefficient that is assumed to be 1.5, V_{e50} is the extreme wind speed with a 50-year recurrence time interval, $A_{proj,B}$ is the projected area of the blade, B is the number of blades.

The aerodynamic forces on the tower and nacelle are calculated as follows:

$$F_{tower} = C_{f,tower} \frac{1}{2} \rho V_{e50}^2 A_{proj,tower} \tag{2.3}$$

$$F_{nacelle} = C_{f,nacelle} \frac{1}{2} \rho V_{e50}^2 A_{proj,nacelle} \tag{2.4}$$

In which $C_{f,tower}$ is the force coefficient of the tower and is assumed to be 1.3, $C_{f,nacelle}$ is the force coefficient of nacelle and is assumed to be 1.5, $A_{proj,tower}$ and $A_{proj,nacelle}$ are the projected area of the tower and nacelle, respectively.

The ultimate flap bending moment, M_{yB}, is calculated as follows:

$$M_{yB} = (C_d \frac{1}{2} \rho V_{e50}^2 A_{proj,B})(\frac{1}{2} R) \quad (2.5)$$

In which R is the radius of the wind turbine.

For furling or keep spinning turbines, $F_{x-shaft}$ and M_{yB} change, and can be calculated using the following equations:

$$F_{x-shaft} = (0.34\lambda_{e50}^2) \frac{1}{2} \rho V_{e50}^2 (A_{proj,B} B) \quad (2.6)$$

$$M_{yB} = [C_{l,max} \frac{1}{2} \rho V_{e50}^2 \left(\frac{1}{2} A_{proj,B}\right)](\frac{2}{3} R) \quad (2.7)$$

In which λ_{e50} is the 50-year extreme tip steep ratio, and $C_{l,max}$ is the maximum lift coefficient at the tip, which is assumed to be 2.0.

2.2 CFFT history, application, advantages, and disadvantages

The idea of developing CFFTs emerged from the research of concrete-filled steel tubes (CFSTs). Compared to plain concrete, CFSTs have higher strength, stiffness, ductility, and stability; however, because of the material properties of steel, CFSTs have their own problems such as partial separation and premature buckling. Besides, corrosion is a huge threat to CFSTs in harsh environments (Yu et al., 2013).

Fibre reinforced polymer (FRP) is widely used in civil engineering applications. In the last few decades, FRP materials have become widely used for rehabilitation of concrete structures. FRP jacketing is one of the most popular strengthening methods for concrete columns and beams due to its high strength and ductility. In recent years, use of FRP composites has also been extended to new construction. Prefabricated FRP tubes can be used as structural stay-in-place formwork for concrete structures, presenting a rapid low-waste approach to construction that also results in excellent structural and durability characteristics. Mirmiran and Shahawy first introduced the idea of CFFTs; they developed a new passive confinement model and a composite action model to describe their behaviour (Mirmiran & Shahawy, 1996).

Uniaxial compression experiments were conducted to test the strength of CFFTs, and the results were compared to confinement models developed for conventional reinforced concrete columns, which tended to overestimate the strength of CFFTs because of the lack of consideration of the dilatancy of confined concrete (Mirmiran & Shahawy, 1997). Other early researchers focused on the effects of fibre type, tube thickness, and concrete compressive strength on CFFT column behaviour (discussed in more detail later). Beam-column tests demonstrated that CFFTs have a better performance than prestressed concrete columns (Mirmiran, 2000). Experiments also showed that stress and strain at failure both reduced significantly with the increase of slenderness ratio, and a new equation was then developed for the slenderness limit of CFFTs (Mirmiran et al., 2001). The flexural behaviour of CFFTs was also examined using four-point bending tests to compare the stress, strain, deflection, and moment-curvature behaviour of large-scale concrete-filled glass FRP tubes (Fam & Rizkalla, 2002).

Following promising experimental and numerical studies to understand and characterize the behaviour of CFFTs, they were also successfully applied in construction projects. CFFTs have been used as piles, bridge girders, and piers, and may also be used as large pipes and tunnels, overhead sign structures, and utility poles (Flisak et al., 2001). Figure 2.6 and Fig. 2.7 present some of the applications of CFFTs in the field.

Figure 2.6 Route 40 Bridge over the Nottoway River in Virginia (Fam et al., 2003)

Figure 2.7 Buried CFFT arch bridge in Bradley, Maine, USA (constructed in 2010) (Dagher et al., 2012)

Previous experience has highlighted the advantages and disadvantages of CFFTs. It has been shown that the FRP tubes not only protect the concrete core and reinforcement from corrosion, but also provide reinforcement to the structure. FRP tubes can provide a superior confinement to the concrete core than conventional steel reinforcement to enhance strength and ductility and provide extra shear and flexural resistance (Fam et al., 2007). Fibres can be applied in any orientations, thickness, and number of layers, and FRP tubes will have different failure modes and behaviour under different lamina structures. This means that FRP tubes have an incomparable versatility (Fam & Rizkalla, 2002). Compared with plain concrete and CFSTs, CFFTs also have advantages such as being lightweight and resistant to deterioration due to corrosion and other causes, while the main disadvantage of CFFTs is the initial cost of FRP materials. FRP materials include different composites like glass fibre-reinforced polymer (GFRP), aramid fibre-reinforced polymer (AFRP), and carbon fibre-reinforced polymer (CFRP). For GFRP, the cost is about 3 times as much for steel, and for AFRP and CFRP, the cost can be as much as 10 times higher; however, costs are becoming more competitive. CFFTs also have problems like brittleness and inadequate ductility, which can lead to the rupture of the FRP tube (Burgoyne, 2009; Yu et al., 2013). The strength and ductility of the FRP tubes can often be improved by optimizing the fibre orientation and laminate structure.

2.3 Structural performance

Researchers have studied the structural performance of CFFTs under axial loads, four-point bending tests, and combined loads. The influence of different parameters like geometric shape, fibre orientation, material properties, reinforcement ratio, type of reinforcing bars, and prestressing ratio on the behaviour of CFFTs have been examined. A summary of their behaviour under different loading conditions and the effects of different parameters are presented in this section.

2.3.1 Axial compression

The FRP tube enhances axial performance such as concrete strength, stiffness, and ductility by providing lateral confinement to the concrete core (Fam et al., 2007).

CFFT performance under axial compression is influenced by several parameters. Fibre orientation, type of FRP material, FRP tube thickness, concrete strength, and tube slenderness can each significantly affect the behaviour of CFFTs.

Fibre orientation is an important parameter while studying the behaviour of CFFTs, as it can influence the axial stress and strain behaviour, load capacity, confinement effectiveness, and failure modes. Many experiments and analytical studies were conducted to investigate how the fibre angle influences the performance of CFFTs under axial loading. Figure 2.8 presents a schematic view of a column test setup showing strain gauges installed at various inclination angles. When fibres are aligned in the hoop direction (θ_f = 90°), they are more effective in enhancing the concrete compressive behaviour by increasing the confining stiffness. Both strength and strain enhancements are significant while fibres are aligned in the hoop direction, and this kind of CFFT also displays a ductile behaviour and performs well as columns under axial load. However, when fibre orientations are inclined with respect to the hoop direction (θ_f < 90°), CFFTs tend to have a lower ultimate load capacity, and progressive failure modes may be observed. The CFFTs with fibres aligned in longitudinal direction (θ_f = 90°) have good behaviour as beams under bending. When the fibre angles are below a threshold value (which is different for different FRP materials), the FRP tube will not contribute to the confinement. Based on conventional laminate theory, the threshold winding angle for glass FRPs was found to be ±51.5˚, as measured from the longitudinal axis direction. These theoretical results were compared to experimental results and were found to be in good agreement. The same method was used to calculate the threshold winding angles of carbon FRPs (CFRPs), S-glass FRPs, and E-glass FRPs with different material properties; results were found to be about ±55.5˚, ±55.5˚, and ±50˚, respectively, as shown in Fig. 2.9 (Hain et al., 2019; Vincent & Ozbakkaloglu, 2013).

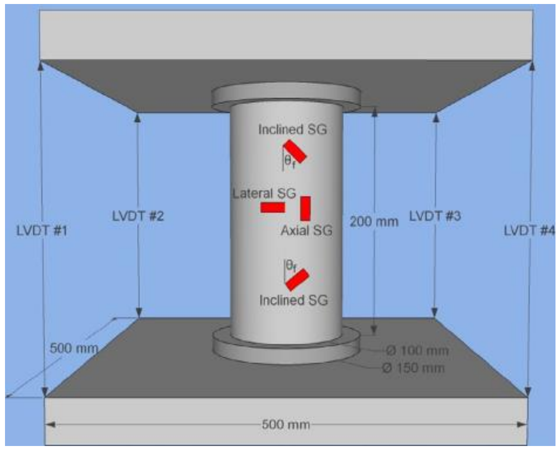

Figure 2.8 Column test setup (Vincent & Ozbakkaloglu, 2013)

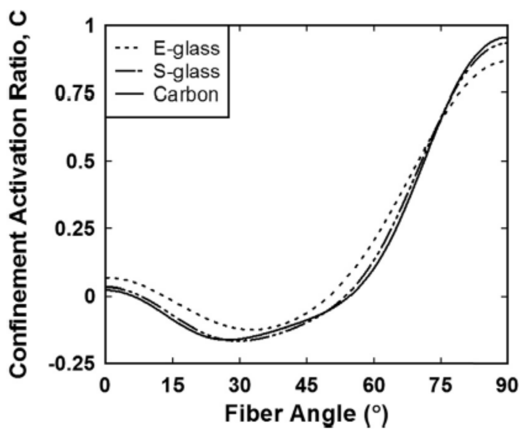

Figure 2.9 Confinement activation ratio-fibre angle relationship (Hain, Motaref, et al., 2019)

The FRP tube material type is another important factor that influences the behaviour of CFFTs significantly. Ultimate compressive strength does not change a lot according to previous research, but ultimate axial strain is strongly dependent on the type of FRP material used. Compared to CFFTs made of CFRP tubes, CFFTs made of aramid FRP (AFRP) have a higher ultimate axial strain, and CFFTs made of high modulus (HM) CFRP tubes have a lower ultimate axial strain. The gap between the minimum and maximum ultimate strain values were about 0.005. Comparing these three materials it is clear that the higher the ultimate rupture strain of the fibres, the higher the ultimate axial strain of CFFTs (Ozbakkaloglu, 2013a). Another research compared CFRP-CFFTs to GFRP-CFFTs and came to the conclusion that CFRP-CFFTs can reach higher ultimate axial strains. The fibre orientations used in this study were ±60˚ in the outer layers and 90˚ in the inner layers (Khan et al., 2020). The two research studies cannot be directly compared to each other, but as indicated, while CFRP-CFFTs have a better performance than GFRP-CFFTs, they are less efficient than AFRP-CFFTs. The FRP tube thickness can influence the ultimate strain as well. Tubes with larger wall thickness always reach higher ultimate strains when the confinement effectiveness is high enough. Previous research has shown that unlike the influence of the tube thickness on the length of the second branch of the stress-strain curve, which is obvious, only a small influence of wall thickness on the slope of the second branch of the stress-strain curve can be observed, as shown in Fig. 2.10 (SP1 represents plain concrete and SR40L3 and SR40L5 represent columns with 3 and 5 FRP layers, respectively) (Ozbakkaloglu & Oehlers, 2008). In another study, results showed that when the winding angle is lower than the threshold, the increase of wall thickness will not increase the performance of CFFTs, since the additional layers of fibres do not provide confinement. However, when fibres are aligned at an angle above the threshold, the peak load, displacement, and post-yield hardening response will all increase with the increase of FRP shell thickness, since CFFTs with thicker FRP walls have better confinement effectiveness which results in an improved axial performance. The results revealed that a GFRP-CFFT with a wall thickness of 5.59 mm and ±55˚ fibre angle resisted about 50% higher axial load than GFRP-CFFT with a 3.05 mm wall thickness (Hain, Motaref, et al., 2019).

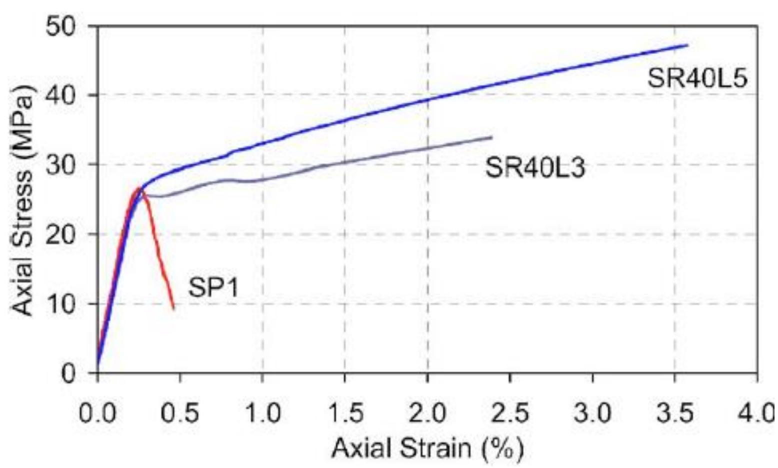

Figure 2.10 Axial stress-strain relationship (Ozbakkaloglu & Oehlers, 2008)

The influence of concrete strength was also studied. Research on rectangular tubes shows that the difference between high-strength concrete (HSC) and normal-strength concrete (NSC) were taken into consideration by some researchers. If the confinement is not sufficient (under a nominal confinement ratio), HSCFFTs have lower strength and strain enhancement ratios than NSCFFTs. In Fig. 2.11 (a), both specimens have 3 FRP layers and the column corner radius is 20 mm; the loss of strength can be observed in both CFFTs, but the rate for the HSC (R2R20L3) is more rapid than for the NSC (R1R20L3). Figure 2.11 (b) shows that when the column corner radius is 40 mm, the performance difference between HSC and NSC becomes less significant, which indicates the effect of confinement. Meanwhile, a study on circular tubes shows that the concrete strength only has a minimal influence on the ultimate axial strain. However, although the confinement requirements increase significantly with concrete strength, when the concrete is confined properly, HSCFFTs have better ductility than NSCFFTs (Ozbakkaloglu, 2013a; Ozbakkaloglu & Oehlers, 2008).

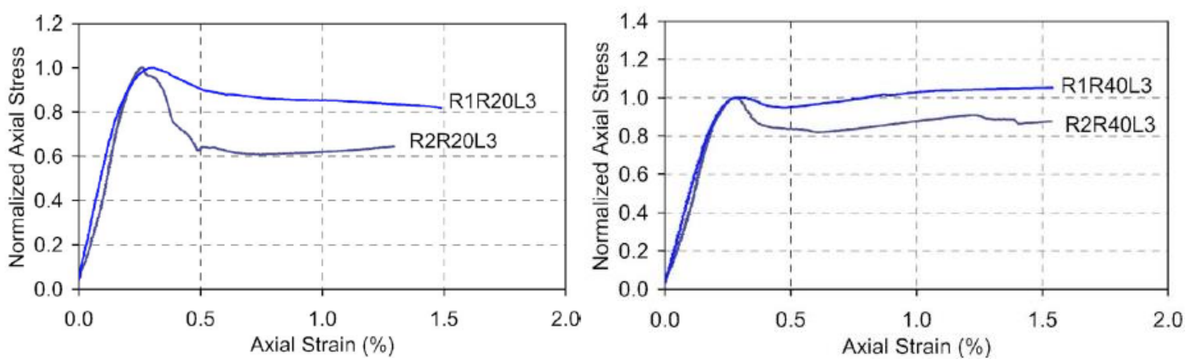

(a) R= 20 mm (b) R = 40 mm

Figure 2.11 Axial stress-strain relationship (a) R = 20 mm (b) R = 40 mm (Ozbakkaloglu & Oehlers, 2008)

The influence of slenderness ratio on axial strength did not reach a consensus, but it is agreed that axial strain will decrease significantly and the failure mode of CFFTs may change to buckling failure if the slenderness ratio increases. Mirmiran's research shows that when the height to diameter (H/D) ratio increased from 11 to 36, a significant decrease (up to 71%) in strength was observed compared to equivalent short columns. In the same study, researchers also found that the influence of slenderness on the column ductility is higher than on the strength, with a slightly higher reduction on hoop strain than axial strain (Mirmiran et al., 2001). Another study agreed with Mirmiran's findings, reporting that when the H/D ratio is larger than 8, axial compressive strength and load capacity will face a significant decrease, since the failure mode is a combination of FRP rupture and local buckling of internal bars. The yield load of a column with a slenderness ratio of 8 was only 53% of the ultimate load, increasing to 90% when the slenderness ratio increased to 20. The study also showed that when the slenderness ratio was higher than 16, the possibility of buckling instability increased as the tube final failure mode changed from rupture of the FRP tube to buckling. Figure 2.12 shows the failure modes of steel-reinforced CFFT columns with slenderness ratio from 8 to 20 (Abdallah et al., 2018). Different results were obtained by other researchers. Park found that the H/D ratio of CFFT only has an insignificant influence on the strength ratio f_{cc}/f_{co} (ultimate compressive strength/unconfined concrete strength). Researchers also compared their results to Mirmiran's, as shown in Fig. 2.13 (Park et al., 2011). FRP tubes with H/D ratio lower than 5 were found to have a significant decrease in axial strain enhancement with the increase of H/D ratio, but the slenderness ratio does not have a huge influence on axial strength enhancement and hoop strains (Vincent & Ozbakkaloglu, 2015a). When the slenderness ratio is the same, small specimens only have slightly better performance than larger equivalents, which means specimen size only has a small influence on the compressive behaviour (Ozbakkaloglu, 2013a).

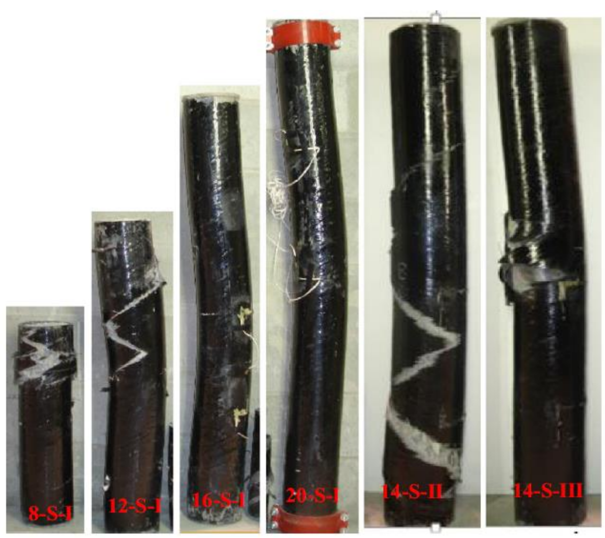

Figure 2.12 Failure modes of slender columns (Abdallah et al., 2018)

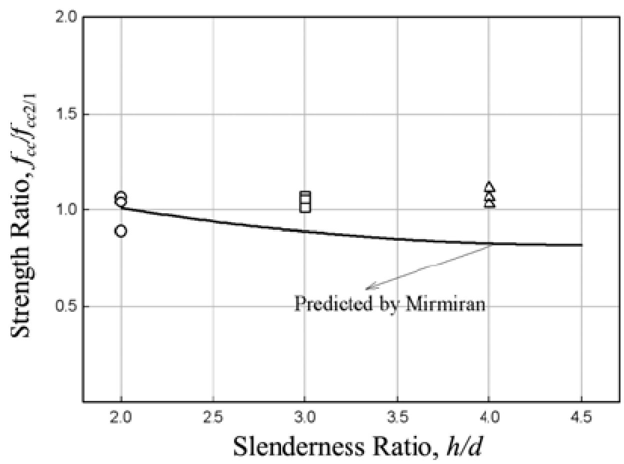

Figure 2.13 CFFT strength ratio and slenderness ratio relationship (Park et al., 2011)

Steel and FRP reinforcing bars in CFFTs both can improve load capacity, ductility, and many other performance indicators. One research study indicated that steel reinforced CFFTs have higher axial deformations at ultimate, which means they have higher ductility. The ultimate capacity of CFRP reinforced CFFTs were 0% to 13% lower than steel reinforced CFFTs, which is not significant (Abdallah et al., 2018).

By introducing prestressing to a concrete member, the concrete can have a greater strength, so the prestressing technique is widely used in concrete construction. A prestressed FRP composite shell has been considered by researchers. Prestressed FRP tubes can lead to an increase in ductility and energy absorption capacity. The ultimate compressive strength also increases, but the ultimate axial strain only increases when the prestressing CFFT is well-confined. When high-strength concrete is used, prestressing CFFT can avoid the problem of strength loss and brittle failure (Vincent & Ozbakkaloglu, 2015).

Circular tubes have better performance than rectangular tubes, but in some situations, rectangular tubes are irreplaceable. Two special parameters that influence rectangular beams are corner radius and sectional aspect ratio. When the corner radius increases and the aspect ratio approaches unity, the confinement effectiveness increases, hence CFFTs tend to have better compressive behaviour (Ozbakkaloglu, 2013a).

Although the influences of CFFT size, manufacturing method, and tube end condition on axial capacity are small, they have been noticed by some researchers. Small CFFTs generally have a higher degree of strength enhancement compared to their larger counterparts, but the improvement in performance is quite small. CFFTs manufactured using automated filament winding process have a higher confinement effectiveness than the manual hand lay-up CFFTs, which is less significant. CFFTs with end plates tend to have a slightly higher ultimate strain and lower peak stress. The effect of taper ratio has not been sufficiently studied (Abdallah et al., 2018; Ozbakkaloglu, 2013a; Ozbakkaloglu & Oehlers, 2008; Vincent & Ozbakkaloglu, 2013).

2.3.2 Performance in bending

Performance in bending has primarily been examined under four-point bending tests. Figure 2.14 indicates the test setup and instrumentation of one of the experiments presented in the literature (Mohamed & Masmoudi, 2010). Different researchers have focused on different parameters such as the effect of internal reinforcing bars, fibre orientation, concrete strength, concrete-filling ratio and so on.

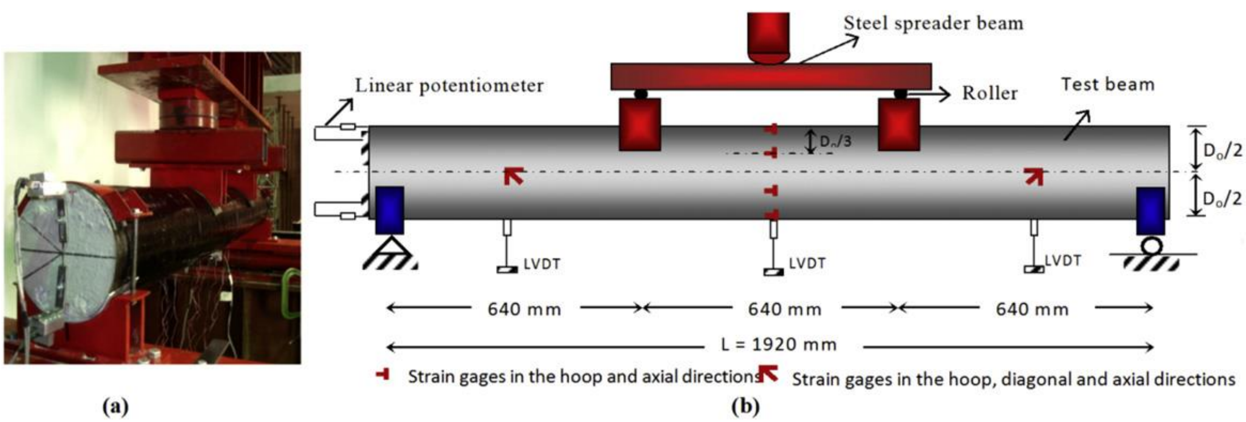

Figure 2.14 (a) Side view (b) Schematic of test setup (Mohamed & Masmoudi, 2010)

Comparing GFRP tubes with conventional steel spiral reinforcement, it is clear that beams with GFRP tubes had higher flexural strength, with increases up to 113% compared to beams with steel spiral reinforcement. The ductility of CFFTs is also higher. The main reason for the better performance of CFFTs is the larger confinement area that consists of the entire concrete core. Unlike steel spiral reinforcement, which is affected by spalling and crushing, GFRP tubes provide reinforcement in the longitudinal direction while also confining the concrete core continuously

(Fam et al., 2007). Similar results were observed in another research. When the concrete strength was 45 MPa, CFFTs had about 60% higher post-cracking flexural stiffness than steel spiral reinforced beams; the improvement of flexural strength and energy absorption were about 9% and 7%, respectively (Mohamed & Masmoudi, 2010).

Apart from transverse reinforcement, the presence of internal longitudinal reinforcing bars also influences experiment results. CFFTs with steel reinforcing bars showed lower deflection, higher stiffness, and approximately 64% higher strength than similar beams with GFRP reinforcing bars when the concrete strength was 30 MPa. On the other hand, the ductility of beams with steel reinforcing bars was found to be 5.6 times the indices of beams with GFRP reinforcing bars, which is much higher (Mohamed & Masmoudi, 2010). Steel-reinforced CFFTs tend to be superior to FRP-reinforced CFFTs because their failure is more gradual, while those with FRP bars tend to fail at the same time as the FRP tubes and result in a sudden failure (Cole & Fam, 2006).

A parametric study was done to obtain the analytical axial-flexural (P* – M*) interaction of CFFTs with different fibre orientations at 30˚, 45˚, and 60˚ along the longitudinal direction. The results are shown in Fig. 2.15 and indicate that unlike CFFTs under concentric axial loads, fibre orientations only have a limited influence on CFFTs under bending (Khan et al., 2018). On the contrary, FRP tube thickness proved to have a larger effect on the performance of CFFTs under bending. When the concrete strength was 30 MPa, beams with 2.2 times thicker tubes had slightly lower deflection, 22.3% higher flexural strength, and 52% higher ductility index. Besides, the increase of the FRP tube thickness resulted in the decrease of the compression and tension strains of the FRP tubes (Mohamed & Masmoudi, 2010).

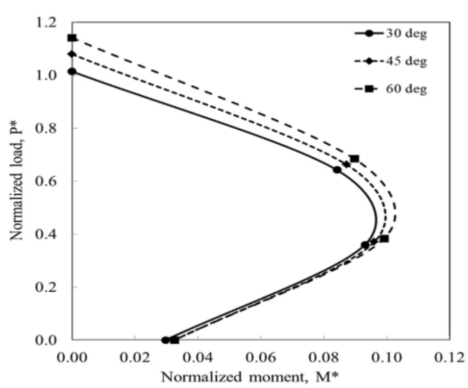

Figure 2.15 Normalized P* - M* interactions (Khan et al., 2018)

According to previous research, for normal and medium strength concrete, concrete compressive strength does not affect the flexural behaviour of beams significantly. When the concrete compressive strength increased from 30 MPa to 45 MPa, the flexural strength only increased 4.8% and 14%, respectively, depending on the different wall thicknesses. The main reason is concrete compressive strength does not influence the failure mode of beams, which is typically FRP rupture at the tension side. As is shown in Fig. 2.16, the concrete core at the compression side did not crush for both concrete strengths, so the increase does not have a huge effect (Mohamed & Masmoudi, 2010).

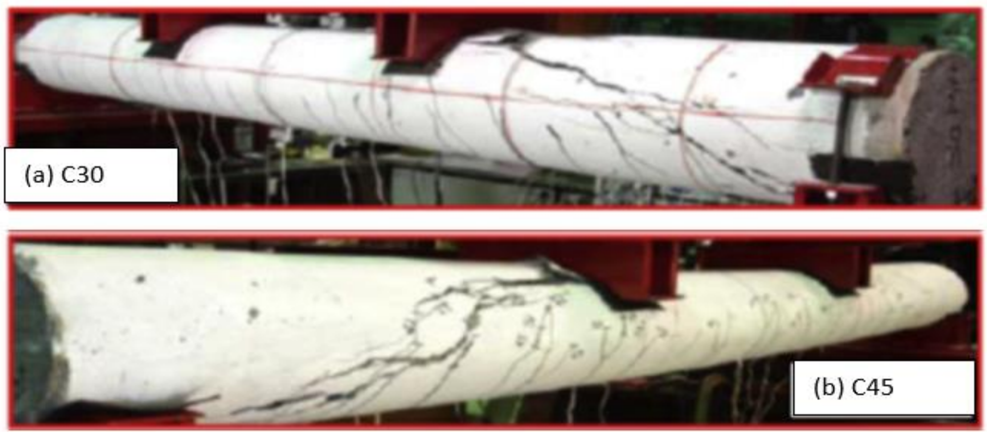

Figure 2.16 concrete core of CFFTs (Mohamed & Masmoudi, 2010)

The effect of prestressing in bending was considered by researchers and prestressed concrete-filled FRP tubes (PCFFTs) have been shown to have higher flexural strength, initial stiffness, moment capacity, and better confinement effect than steel spiral reinforced tubes and CFFTs (Fam et al., 2007). Compared to conventional prestressed steel reinforced beams, PCFFTs had 2.43 times their ultimate strength, 1.89 times their deformation capacity, 1.63 times their deformation ductility, and 3.87 times their energy absorption. Similar to non-prestressed CFFTs, by increasing tube thickness and having more fibres aligned in the hoop direction, the tube ultimate capacity and stiffness was increased. Increasing the number of strands also improves the performance, but the concrete strength has an insignificant influence on PCFFTs (Ahmed et al., 2020). Another study also proved that PCFFTs have higher flexural strengths and initial stiffness than CFFTs. Figure 2.17 shows the influence of prestress level, in which PCFFT-1 had 11.0 MPa effective prestress level and 26% effective prestressing ratio while PCFFT-2 had 4.81 MPa effective prestress level and 12.5% effective prestressing ratio. It indicated that the increase of prestress level does not increase the initial stiffness and the ultimate load significantly, but the cracking load had a 67% increase (Fam & Mandal, 2006).

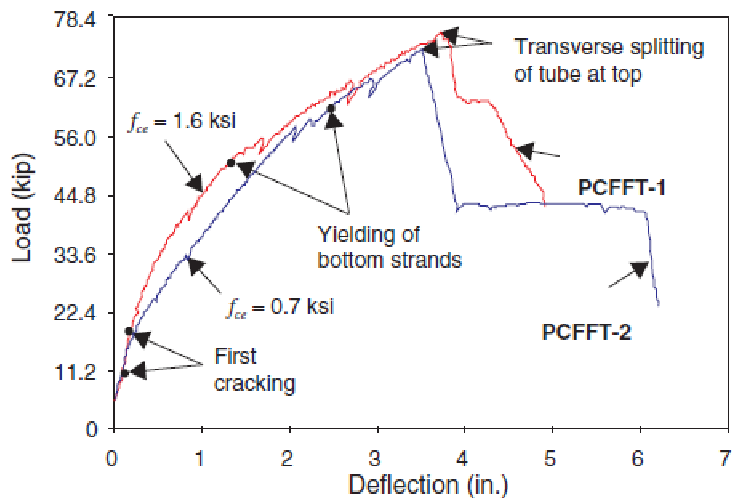

Figure 2.17 Load-deflection curves of different prestress level (Fam & Mandal, 2006)

Rectangular partially- and fully-filled CFFT beams were examined by different researchers. Compared to fully-filled concrete beams, partially-filled beams decrease the weight significantly. Partially-filled CFFTs with or without inner FRP tubes have different behaviour in bending. With an inner circular hollow FRP tube, the flexural strength of a partially-filled CFFT tube was 115% higher than steel spiral beams, while the flexural strength of a fully-filled CFFT tube was only 97% higher. The failure modes were also different. The former ones had a gradual compression failure due to the effective confining action by the circular hollow tube, but the latter ones had tension or balanced tension and compression failure (Masmoudi & Abouzied, 2018). Another research studied the rectangular partially-filled CFFT beams without an inner FRP tube, but still came to a similar conclusion: fully-filled CFFT beams often fail by rupture of FRP on the tension side, while partially-filled CFFT beams fail by inward buckling and fracture of the concrete compressive flange. Though the flexural strength of partially-filled CFFT beams was about 22% lower than fully-filled CFFT beams, the strength-to-weight ratio is 77% higher (Fam et al., 2005).

The end conditions of CFFTs were also tested. Capped beams had 40% to 67% higher energy absorption ability than uncapped beams because of the crushing of the concrete core. They also had higher ratios of hoop to longitudinal strain, which shows the confinement pressure was influenced by the end condition (Hain, et al., 2019).

2.3.3 Performance under combined loads

In practical applications, piles, columns, and wind turbine towers are often exposed to axial compression loads and bending loads at the same time, so it is important to know the performance and failure modes under combined loading, although for wind turbine towers, bending loads are the dominate. Considering the interaction between axial loads and moment, tensile rupture occurs before the balance point is reached, then, with the increase of axial loads, the failure would be governed by compression. A similar axial load-bending moment interaction curve between CFFTs with GFRP tubes and conventional reinforced concrete was found in previous research (Fam, 2000).

Different parameters like eccentricity and internal reinforcement can affect the performance of CFFTs. The larger the eccentricity, the lower the peak axial load and ductility, since with the increase of axial load eccentricity, the confinement effectiveness of the GFRP tube will be decreased. Besides, it is also known that GFRP bar or CFRP bar reinforced CFFTs have better axial load-bending moment capacity than unreinforced CFFTs (Hadi et al., 2016). Similar results were also obtained in Khan's research, which shows that GFRP bar reinforced CFFTs can resist higher axial and flexural loads as well as lateral deformations at peak axial loads than CFFTs without reinforcing bars (Khan et al., 2017).

As previously mentioned, GFRP is cheaper than many other FRP materials, so GFRP tubes were most commonly used in experiments, but some researchers also studied the performance of CFRP-CFFTs. For CFRP-CFFTs with and without CFRP bar reinforcement, axial load and bending moment capacity both decreased with the increase of eccentricity, which is the same as GFRP-CFFTs. It is important to note that CFRP bar reinforced CFFTs have a superior axial load and bending moment capacity, but unreinforced CFFTs do not perform well and only under concentric axial load they can have a better behaviour than conventional steel reinforced tubes, as is shown in Fig. 2.18. The peak axial loads of CFRP bar reinforced CFFTs were 36.2% and 56.6% higher and the bending moments were 75.3% and 96.9% higher than CFFT without reinforcement at 50 mm and 25 mm eccentricity, respectively (Khan et al., 2018).

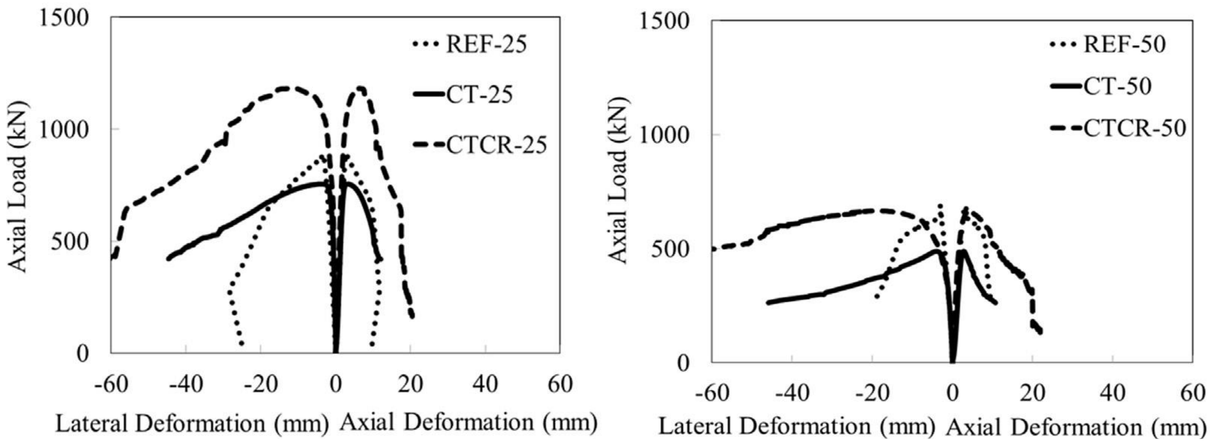

(a) 25 mm eccentricity (b) 50 mm eccentricity

Figure 2.18 Load-deflection curves of eccentric (a) 25 mm (b) 50 mm (Khan et al., 2018)

According to the experimental results, GFRP-CFFTs with GFRP bar reinforcement always had a better axial load-bending moment interaction and higher ductility than CFRP-CFFTs reinforced with CFRP bars. The peak axial load, moment capacity and ductility of the former one were 36.5%, 37.7%, and 20.3% higher than the latter one, when the eccentricity was 50 mm. However, for tubes without reinforcement, the performance of CFRP-CFFTs and GFRP-CFFTs were similar. For example, when the eccentricity was 50 mm, GFRP columns only had 7.0% higher peak axial load, 4.2% higher moment capacity, and 19.4% higher ductility than CFRP columns. Figure 2.19 shows the axial load-deflection curves of different columns under 50 mm eccentric axial load (Hadi et al., 2016).

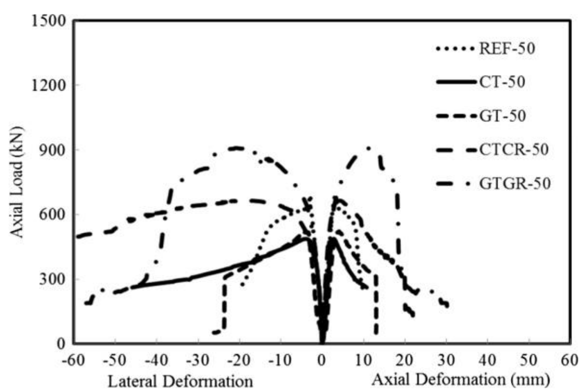

Figure 2.19 Axial load-axial deformation and axial load-lateral deformation behaviour (Hadi et al., 2016)

2.4 Finite element models

The finite element method has been employed to study the performance of FRP tubes and CFFTs for a long time. Some researchers also use this method to study wind turbines and their towers. Widely used finite element method software include ANSYS, OpenFOAM, LS-DYNA, and ABAQUS.

Son and Fam's study employed ANSYS to model hollow FRP tubes and CFFTs under uniform loading and four-point bending. In this study, an eight-node 3-D Reinforced Concrete Solid (SOLID65) element was used to simulate the concrete, and a four-node quadrilateral layered shell element (SHELL181) was used to simulate the FRP tube. Load-deflection responses and stress-strain response were obtained using the finite element method to verify the model with experimental results. The model was then used in the parametric study to examine the influence of parameters including fibre orientation, FRP tube thickness, concrete-filling ratio, and tube diameter. The results showed that the decrease of fibre angle leads to the increase of flexural strength and the effectiveness of concrete-fill. It also indicated that in thin-walled tubes, fibre orientation does not have a significant influence on flexural strength and the effectiveness of concrete-fill is higher. Partially filled FRP tubular poles in flexure were also studied according to the finite element model. A simple design method that can predict the optimum concrete filling length was also developed in this research (Fam & Son, 2008; Son & Fam, 2008).

Hawileh's study also used ANSYS to develop finite element models to study the effectiveness of a side-bonded FRP system used to strengthen reinforced concrete beams in flexure. The concrete element type used in this study was the same as the one Son and Fam used, but the FRP laminates were modeled using SOLID185 elements and considered as orthotropic materials. This element has eight nodes with 3 degrees of freedom for each node. Model validation was done using experimental results, and the models were used to study the influence of critical parameters like concrete strength, type of FRP materials, and steel reinforcement ratio. The results indicated that the effectiveness of externally bonded FRP system was proven by the finite element analysis (Hawileh et al., 2019).

The application of using CFFTs as deep foundations in sandy soil was studied using the finite element method as well. In this study, researchers used ABAQUS to see the influence of different types of FRP materials and the slenderness ratio. During the analysis, FRP tubes were considered as five layers of orthotropic unidirectional laminates, and [0/90] cross-ply laminates were used in this study. For concrete, an eight-node linear brick element type C3D8R was chosen. Results indicate that CFRP tubes had lower settlement than GFRP tubes, due to the higher elastic modulus, but the increase of CFRP pile's length has a slightly better improvement on the settlement than the increase of GFRP pile's strength (El-Nemr et al., 2016).

Another research used ABAQUS to study the performance of FRP-reinforced concrete columns. Columns were tested under axial concentric and eccentric loadings, CFRP and GFRP materials were both studied, and the results were compared to experimental results and presented a close agreement. In this study, C3D8R element was also used for concrete. A reduced deformable four-node doubly curved shell element (S4R) was used to model the FRP tube. This element has six degrees of freedom at each node. The FRP bars were simulated using 3-D truss elements. After the model validation, the finite element models were used to examine the influence of important parameters including the number of reinforcing bars, the thickness of FRP tube, the concrete strength, and the diameter of columns. The results agreed with the analytical results, and proved that both the finite element model and analytical model can be used (Raza et al., 2020).

A prestressed concrete tower for wind turbines was studied using the finite element method using OpenSees and ABAQUS. The ABAQUS model was used to validate the beam-column model built in OpenSees. In the ABAQUS program, a cylinder segment taken from an entire supporting tower was simulated to obtain the rotation-moment relationship. C3D8R elements were used to model the concrete while truss elements were used to simulate the reinforcing bars. The beam-column model simulated in OpenSees was defined as a fibre section. Confined and unconfined concrete fibres and reinforced steel fibres were used. The results presented good agreement with the field test results (Cao et al., 2020).

2.5 New developments

As the range of applications for CFFTs continue to expand, new approaches for optimizing their design continue to be developed. The new developments of CFFTs can be broadly categorized within two groups: the improvement of materials, and the improvement of manufacturing methods.

Hybrid glass/steel fibre-reinforced tube was considered as a new type of FRP tubes to improve the energy absorption of CFFTs. According to the study results, the steel fibres in the shell increases the specimen performance in high-seismic regions (Hain et al., 2019).

New manufacturing methods like prestressed FRP composite shell have also been developed to improve the behaviour of CFFTs filled with high-strength concrete (Vincent & Ozbakkaloglu, 2015). Apart from this method, for circular tubes, a new composite column was also considered. Columns consisting of an inner concrete-filled FRP tube, outer concrete, polymer girder, and concrete cover was developed to increase the strength and ductility of CFFTs (Wang et al., 2017).

Compared to circular tubes, rectangular and square tubes have weaker performances, but in some conditions, rectangular and square beams are necessary, so another new manufacturing method was developed to solve the confinement effectiveness problem of rectangular and square tubes. The method called corner strengthening was used to provide additional reinforcement at the corners to avoid premature failure. Internal panels were incorporated to rectangular tubes, resulting in significant improvement of confinement effectiveness (Ozbakkaloglu, 2013b).

2.6 Summary

With the increasing use of wind power, the number of wind turbines will increase as well. Small-scale wind turbines are different from medium- and large-scale wind turbines; they have smaller size so the installation and maintenance costs are lower; they are easier to transport and can be installed off-grid. In consequence, remote areas that are not connected to the electricity grid can use wind power as a replacement to diesel energy in order to get access to reliable and affordable electricity. Current wind turbine towers are mostly made of steel or concrete materials, and many researchers focused on the large-scale wind turbines. These wind turbine towers have their disadvantages, so a possible alternative for steel and concrete materials is considered. FRP materials have several advantages and the material performance of FRP tubes and CFFTs have been studied by many researchers. The use of CFFTs as bridge girders, piles, and poles has been widely known by many people, but few studies have explored their potential for wind turbine towers. Experimental results are lacking for wind turbine towers made of CFFT for small-scale wind turbines. Considering the high cost of FRP materials and the cost, time, and field requirements of wind turbine field test, the finite element method can be a good method for studying the performance of wind turbine towers made of CFFTs.

When it comes to the CFFT structural performance, the experimental results of the influence of critical parameters such as FRP tube thickness, type of FRP materials, concrete strength, and prestressing on CFFTs under concentric and eccentric axial loads and four-point bending can be found in many studies. Enough results were obtained in this area, especially for the conditions when the parameters were considered individually. However, few studies about the effect of other parameters were conducted. For example, the influence of slenderness ratio was only considered when concentric load was applied; only a few researchers have considered the effect of fibre orientations; it is difficult to find research about taper ratio or prestressing level; though there are studies about partially-filled concrete, researchers only studied the difference between totally filled concrete and partially-filled concrete without exploring the influence of different concrete filling ratios. Various combination of these parameters may also influence the performance of CFFTs, but few of them have been considered, especially for relatively large-scale cantilever towers.

Due to the cost, field and manufacturing restrictions, large columns and beams are difficult to build and test in the laboratory. The largest CFFTs found in experimental data was 942×10400 mm, and the beam was tested under four-point bending (Fam, 2000). Compared to beams, it is even more difficult to test large columns under axial loading. Finite element method can help study the performances of large specimens; this is another reason why finite element analysis is important.

In practical applications, CFFTs used as piles, columns, and beams are usually subjected to complex loading. A large portion of available research has focused on the performance of CFFTs under uniaxial loading, as shown in Section 2.3.1, while other studies have focused on the performance of CFFTs under pure bending or eccentric axial loading, which combines bending and axial loading together, as shown in Sections 2.3.2 and 2.3.3. Few studies have investigated the torsional behaviour of CFFTs, let alone the combination of axial, bending, and torsion loads.

This study aims to fill these current knowledge gaps by building a finite element model for CFFT cantilever towers in order to investigate the influence of key parameters on their performance. This work contributes to the overall goal of improving the feasibility of wind energy solutions for remote areas.

Chapter 3 Model validation

The commercial software ABAQUS was used to model the behaviour of selected experimental results reported in literature in order to validate the modelling approach and parameters. To capture a range of behaviours, selected studies include hollow FRP tubes and CFFTs that were tested in flexure under pour-point bending, as well as CFFT columns that were tested under axial loads. In this chapter, modelling outputs are compared to the experimental results to verify the accuracy of the model.

3.1 Experimental studies

Fam tested the structural behaviour of hollow FRP tubes, CFFTs in flexure, and short columns under axial loads (Fam, 2000). FRP and concrete material properties measured during the experiments are presented below along with specimen geometries.

3.1.1 Measured FRP material properties

Material properties have a significant influence on the behaviour of CFFTs. Table 3.1 shows the properties of the FRP tubes used in the modelling. Though the material properties of a single lamina were the same, the material properties of tubes were different due to the different FRP architecture. The Poisson's ratio for tube 3 and axial compressive strength for tube 4 were not provided. The other reported properties are based on lamination theory and were obtained by Fam (2000). Concrete compressive strength ranged from 37 MPa to 58 MPa depending on the test specimen, as detailed in the following sections.

Table 3.1 Material properties of FRP tubes (Fam, 2000)

Tube number	Properties in the axial direction				Properties in the hoop direction	
	$E(GPa)$	$f_{u(Ten.)}(MPa)$	$f_{u(Comp.)}(MPa)$	υ	$E(GPa)$	$f_{u(Ten.)}(MPa)$
3	31	480	136	/	23	398
4	37.7	629	/	0.24	8.7	193
5	17.4	348	78	0.09	27.7	547
6	17.8	318	74	0.08	27.8	536
9	16.6	250	104	0.32	17.7	353
10	17	244	104	0.39	15	216

3.1.2 Specimens and test setup

Lamina structure, stacking sequence, and geometry of the FRP tubes are shown in Table 3.2 and Table 3.3. The fibre angles are measured with respect to the longitudinal axis of the tube. All of the tubes were made of GFRP with E-glass fibres and epoxy resin with a fibre volume of 51%.

Table 3.2 Geometry of hollow tubes (Fam, 2000)

Tube number	Outer diameter (mm)	Tube thickness (mm)	Number of layers
3	100	3.08	9
4	100	3.09	1
5	168	2.56	9
6	219	2.21	9
9	626	5.41	5
10	942	8.93	7

Table 3.3 Lamina structure and stacking sequence (Fam, 2000)

Tube number		Layer								
		1	2	3	4	5	6	7	8	9
3	Thickness (mm)	0.32	0.35	0.27	0.48	0.26	0.51	0.19	0.51	0.19
	Angle (degrees)	-88	+3	-88	+3	-88	+3	-88	+3	-88
4	Thickness (mm)	3.09								
	Angle (degrees)	0								
5	Thickness (mm)	0.08	0.36	0.28	0.25	0.38	0.25	0.36	0.25	0.35
	Angle (degrees)	+8	-86	-86	+8	-86	+8	-86	+8	-86
6	Thickness (mm)	0.23	0.23	0.23	0.25	0.25	0.28	0.25	0.24	0.25
	Angle (degrees)	+15	-82	-82	+15	-82	+15	-82	+15	-82
9	Thickness (mm)	0.94	0.95	1.63	0.94	0.95				
	Angle (degrees)	+34	-34	+85	+34	-34				
10	Thickness (mm)	1.14	1.15	2.07	1.14	1.15	1.14	1.14		
	Angle (degrees)	+34	-34	+86	+34	-34	+34	-34		

Two hollow FRP tubes and two CFFTs were tested by Fam in flexure under four-point bending. Two rollers supported the beams at each end and two concentrated loads were applied to the beams using a steel spreader beam to create pure bending, as shown in Fig. 3.1. Table 3.4 shows the span length, spacing between loads, number of tubes used, and concrete strength. Four longitudinal and four transverse strain gauges were attached to the surface at mid-span to obtain the strains in the two directions; four displacement gauges (PI gauges) were also installed at mid-span to obtain axial strains; a Linear Motion Transducer (LMT) was placed under the mid-span to monitor the mid-span deflection; mechanical dial-gauges were applied to the ends to monitor the relative slip between the concrete core and the FRP tube.

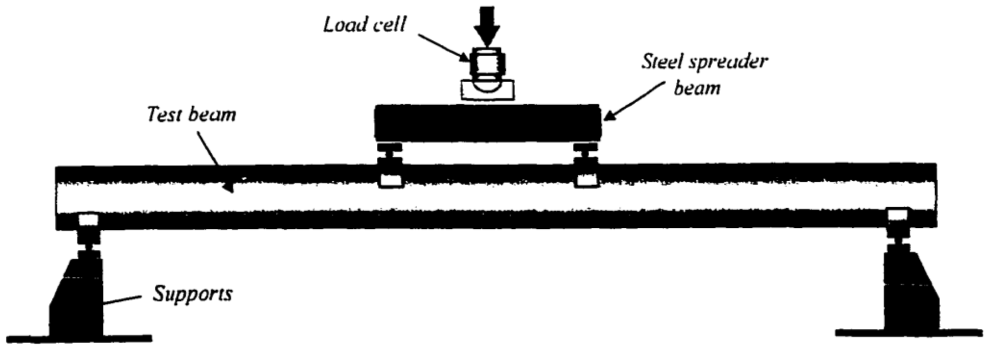

Figure 3.1 Schematic of beam test setup (Fam, 2000)

Table 3.4 Geometry of hollow tubes and CFFTs (Fam, 2000)

Beam number	Beam type	Span L (m)	Spacing between loads (m)	Tube number*	Concrete strength f_c' (MPa)
2a	Hollow tube	1.3	0.2	3	/
3a	Hollow tube	1.3	0.2	4	/
2b	CFFT	1.3	0.2	3	37
4	CFFT	2.9	0.4	5	58
12	CFFT	5.0	1.5	9	33
13	CFFT	10.4	1.5	10	58

Tube number* : Table 3.2 and 3.3.

Short CFFT columns (i.e. stubs) were also tested by Fam under uniaxial compression loading. In total, 12 stubs were examined during the experiment, four of which were selected and modeled using ABAQUS (Table 3.5). Stub 1, Stub 8, and Stub 11 are fully-filled CFFT stubs, and Stub 4 is a partially-filled CFFT without an inner FRP tube. The axial loads were applied to both the concrete core and the FRP tube. To ensure uniform loading pressure, two layers of quick-set plaster were placed between the stub surfaces and the loading and supporting plate. Two axial strain gauges, two hoop strain gauges, and two axial PI-gauges were installed on the surface at the mid height of the stubs. Figure 3.2 shows the stub test setup.

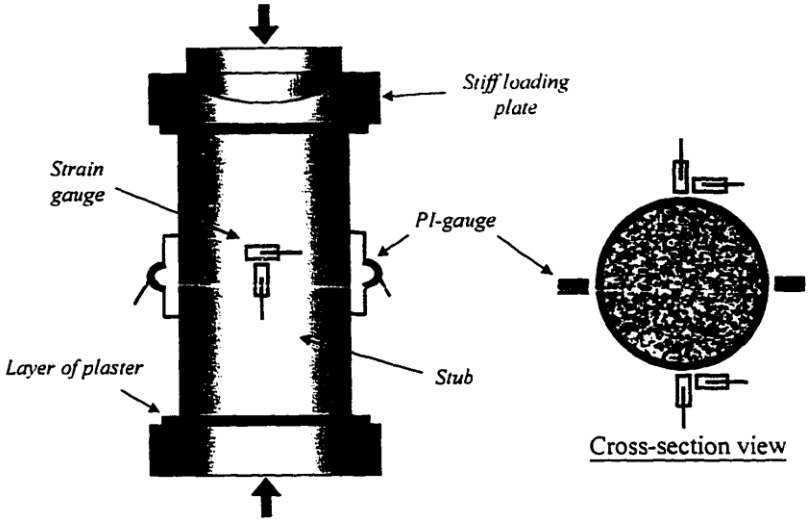

Figure 3.2 Stub test setup and cross-section view (Fam, 2000)

Table 3.5 Geometry of stubs (Fam, 2000)

Stub number	Outer/ inner diameter (mm)	Height (mm)	Tube number*	Concrete strength f_c' (MPa)
1	168/0	336	5	58
4	168/95	336	5	58
8	219/0	438	6	58
11	100/0	200	3	37

Tube number* : Table 3.2 and 3.3.

3.2 Finite element models

The finite element models were built using commercial software ABAQUS/CAE. Two hollow FRP beams, four CFFT beams, and four CFFT stubs were simulated according to Fam's experiments. The material models, element types, interaction between different parts, and other model details are presented below.

3.2.1 Constitutive material models

The FRP material and failure criteria and concrete models are discussed in this section.

3.2.1.1 FRP

The FRP material was defined as a lamina structure. In order to simulate the failure, Tsai-Wu failure criteria was used. The Tsai-Wu criterion was developed for anisotropic materials and can predict failure in a lamina (Tsai & Wu, 1971). It can be described by Equation 3.1:

$$f(\sigma_k) = F_i\sigma_i + F_{ij}\sigma_i\sigma_j = 1 \qquad (3.1)$$

In which contracted notation is used, indices $i, j, k = 1, 2, \ldots 6$, σ_i and σ_j are stresses, and F_i and F_{ij} are the strength tensors that are calculated using tensile and compressive strengths parallel to the fibres or in the transverse direction.

In this case, FRP was considered as an orthotropic material, so the Tsai-Wu criterion can be expressed by Equation 3.2 (ABAQUS, 2016):

$$I_F = F_1\sigma_{11} + F_2\sigma_{22} + F_{11}\sigma_{11}^2 + F_{22}\sigma_{22}^2 + F_{66}\sigma_{12}^2 + 2F_{12}\sigma_{11}\sigma_{22} = 1 \qquad (3.2)$$

In which

$$F_1 = \frac{1}{\sigma_{1t}} + \frac{1}{\sigma_{1c}}, F_2 = \frac{1}{\sigma_{2t}} + \frac{1}{\sigma_{2c}}, F_{11} = -\frac{1}{\sigma_{1t}\sigma_{1c}}, F_{22} = -\frac{1}{\sigma_{2t}\sigma_{2c}}, F_{66} = \frac{1}{\tau_{12}^2} \qquad (3.3)$$

where σ_{1t} and σ_{1c} are tensile and compressive stress limits in 1-direction; σ_{2t} and σ_{2c} are tensile and compressive stress limits in 2-direction; τ_{12}^2 is the shear strength in the $X - Y$ plane.

In Equation 3.2, if the biaxial stress limit σ_{biax}, which is obtained when two perpendicular principal stresses act in the same plane, is given, F_{12} can be expressed in the following form:

$$F_{12} = \frac{1}{2\sigma_{biax}^2}[1 - \left(\frac{1}{\sigma_{1t}} + \frac{1}{\sigma_{1c}} + \frac{1}{\sigma_{2t}} + \frac{1}{\sigma_{2c}}\right)\sigma_{biax} + (\frac{1}{\sigma_{1t}\sigma_{1c}} + \frac{1}{\sigma_{2t}\sigma_{2c}})\sigma_{biax}^2] \qquad (3.4)$$

Otherwise, the cross-product term coefficient ${}^*f$, which depends on the material, was used in the following equation:

$$F_{12} = {}^*f\sqrt{F_{11}F_{22}} \qquad (3.5)$$

where $-1.0 \leq {}^*f \leq 1.0$

Failure stress data is needed for single lamina layers. Although details of a single lamina layer were not presented in Fam's study in 2000, they are reported elsewhere by Son & Fam (2008). Table 3.6 provides the mechanical properties of a single lamina (Son & Fam, 2008).

Table 3.6 Material properties of a single lamina

E1 (GPa)	E2 (GPa)	G12 (GPa)	υ_{12}	σ_{1t}^{f} (MPa)	σ_{1c}^{f} (MPa)	σ_{2t}^{f} (MPa)	σ_{2c}^{f} (MPa)	σ_{12}^{f} (MPa)
38	7.8	3.5	0.28	795	-533	39	-128	89

Where E1 and E2 represent the elastic moduli along and perpendicular to the fibres, G12 represents the shear modulus, υ_{12} represents the Poisson's ratio, σ_{1t}^{f} and σ_{1c}^{f} are the tension and compression stresses in the direction of the fibres, σ_{2t}^{f} and σ_{2c}^{f} are the tension and compression stresses in the direction perpendicular to the fibres, and σ_{12}^{f} is the shear stress.

3.2.1.2 Concrete

For concrete, two elastic material properties were defined: Young's modulus (E) and Poisson's ratio (υ). Properties of concrete in its plastic state were defined using the concrete damaged plasticity model in ABAQUS. This model has been widely used by researchers and the effectiveness of the model has been proven (Al-Ilani & Temsah, 2019; Raza et al., 2020; Ren et al., 2015). The stress-strain relationship for the concrete in compression was obtained using the Hognestad concrete model as described in Eq. (3.6)-(3.8) (Fig. 3.3) (Hognestad, 1951).

$$f_c = f_c' \left[\frac{2\varepsilon_c}{\varepsilon_0} - \left(\frac{\varepsilon_c}{\varepsilon_0}\right)^2\right] \text{ , } \varepsilon_c \leq \varepsilon_0 \quad (3.6)$$

The elastic modulus, E_c, is calculated by Eq. 3.7:

$$E_c = 12680 + 460 f_c' \text{ (MPa)} \quad (3.7)$$

The strain at maximum compressive stress (ε_0) is calculated by Eq. 3.8:

$$\varepsilon_0 = \frac{2f_c'}{E_c} \quad (3.8)$$

where f_c represents compressive stress, ε_c represents the corresponding compressive strain, f_c' represents ultimate compressive stress, and ε_u is the strain when stress equals to $0.85f_c'$, which is considered to be 0.0038.

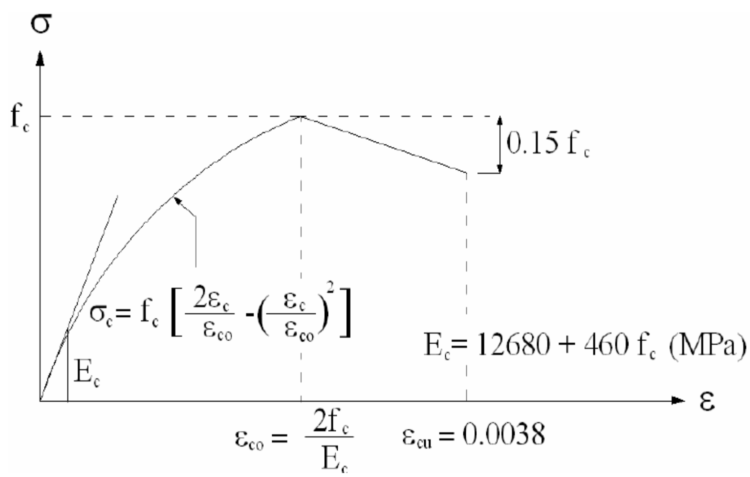

Figure 3.3 Hognestad concrete model (1951)

Figure 3.4 shows the tensile stress-strain relationship given by Eq. 3.9. T_c is the tensile relaxation multiplier, which was set to the default value of 0.6, ε_t represents the tensile strain, f_t represents the tensile stress, ε_t' represents the tensile strain at maximum tensile stress (f_t') and is considered to be 0.0001.

$$f_t = \varepsilon_t \times E_{co}\ ,\ \varepsilon_t < \varepsilon_t' \tag{3.9a}$$

$$f_t = T_C \times f_t'\left(\frac{\varepsilon_t - 6\varepsilon_t'}{\varepsilon_t' - 6\varepsilon_t'}\right),\ \varepsilon_t \geq \varepsilon_t' \tag{3.9b}$$

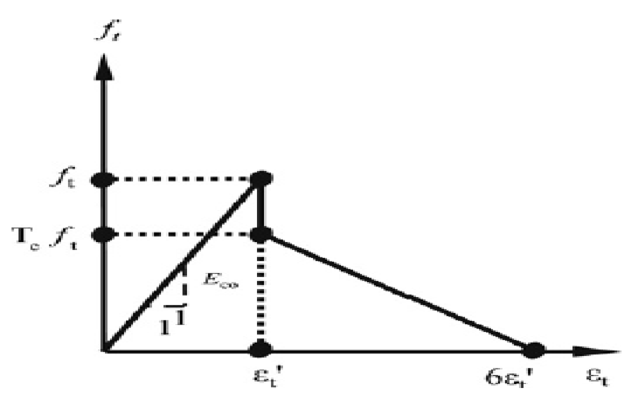

Figure 3.4 Tensile behaviour of concrete (Son & Fam, 2008)

Other important properties including concrete dilation angle, flow potential eccentricity, the ratio of initial equibiaxial compressive yield stress to initial uniaxial compressive yield stress, the ratio of the second stress invariant on the tensile meridian, and viscosity parameter were all set to default values (30˚, 0.1, 1.16, 0.667, and 0.00001, respectively). The sensitivity test for CDP model was not conducted since the results agree with experimental results well.

To examine the influence of concrete constitutive models, another concrete model was also used to simulate the beams and the columns. The stress-strain relationship for confined concrete can be applied to both circular and rectangular shaped reinforced concrete. The model shown in Fig. 3.5 and given by Eqs. 3.10 to 3.14 was developed by Mander and other researchers and is based on Popovics concrete model (Mander et al., 1988; Popovics, 1973):

$$f_c = \frac{f_c' \cdot x \cdot r}{r-1+x^r} \tag{3.10}$$

where

$$x = \frac{\varepsilon_c}{\varepsilon_c'} \tag{3.11}$$

$$r = \frac{E_c}{E_c - E_{sec}} \tag{3.12}$$

where the tangent modulus (E_c) and the secant modulus (E_{sec}) of elasticity of the concrete are calculated by:

$$E_c = 5000\sqrt{f_c'} \text{ (MPa)} \tag{3.13}$$

$$E_{sec} = f_c'/\varepsilon_c' \tag{3.14}$$

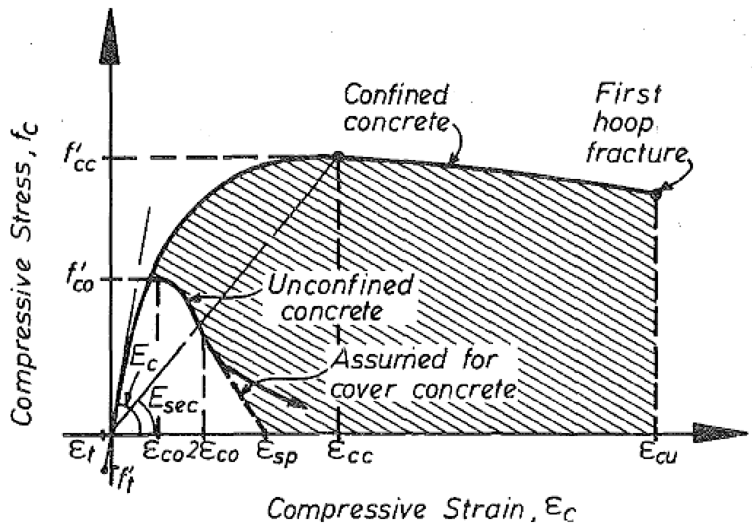

Figure 3.5 Mander's concrete model (Mander et al., 1988)

Figure 3.6 shows the concrete stress-strain relationships introduced in the models using Hognestad concrete model and Mander's concrete model.

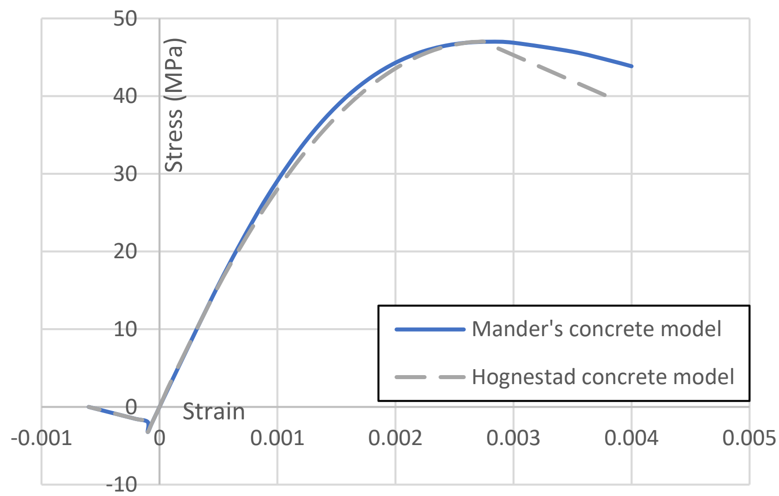

Figure 3.6 Applied concrete stress-strain relationships (a) Hognestad concrete model (b) Mander's concrete model

3.2.2 Element type

Two different elements were used during the analysis. Full integrated elements may suffer from shear locking behaviour when subjected to bending and leads to over-estimation of the stiffness matrix, especially when the element length is of the same order of magnitude as or greater than the wall thickness, which happens during the simulation. Besides, using reduced integration can reduce the computational time (ABAQUS, 2016). Therefore, the concrete was modeled using a 3D eight-node element with hourglass control with reduced integration (C3D8R, Fig 3.7 (a)) and the FRP tube was modeled using a four-node quadrilateral shell element with reduced integration (S4R, Fig. 3.7 (b)).

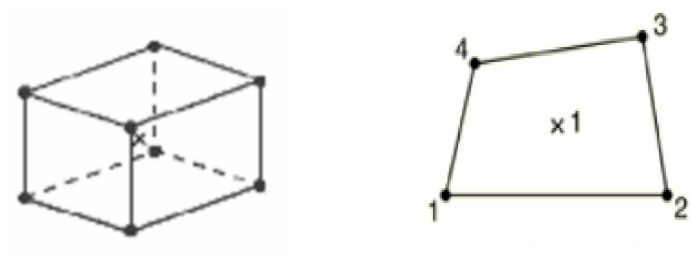

(a) C3D8R (b) S4R

Figure 3.7 Element types (a) C3D8R (b) S4R

3.2.3 Element interaction

The FRP tube and concrete core were connected using surface-to-surface contact, which describes contact between two deformable surfaces. The concrete core was selected as the master surface while the FRP tube was the slave surface since the concrete core has higher stiffness. This contact can prevent large, undetected penetrations of concrete into the FRP. The relative sliding of the two surfaces is assumed to be small, so instead of finite sliding, small sliding was used to build the model. Comparing to finite sliding, small sliding can save computational time and cost and is more robust. Contact cohesive behaviour option was selected as the surface interaction property which assumes that the interface thickness is negligible, and the default values were applied in this case (ABAQUS, 2016; Al-Ilani & Temsah, 2019).

3.2.4 Models

Three different kinds of finite element models were built, including hollow tubes, CFFTs beams, and CFFT stubs, as shown in Table 3.7. In the following section, the mesh size, boundary conditions, and loading conditions will be discussed.

Table 3.7 Models for validation

Specimen type	Specimen name	Model name	Model type
Hollow tube	Beam 2a	Beam 2a	Full
	Beam 3a	Beam 2a	Full
CFFT beams	Beam 2b	Beam 2b	Full
		Beam 2b-M	Quarter, Mander's model
		Beam 2b-Q	Quarter, Hognestad model
	Beam 4	Beam 4	Full
	Beam 12	Beam 12	Full
	Beam 13	Beam 13	Full
CFFT stubs	Stub 1	Stub 1-D	Full, displacement-controlled
		Stub 1-L	Full, load-controlled
	Stub 4	Stub 4-D	Full, displacement-controlled
		Stub 4-L	Full, load-controlled
	Stub 8	Stub 8-D	Full, displacement-controlled
		Stub 8-L	Full, load-controlled
	Stub 11	Stub 11-D	Full, displacement-controlled
		Stub 11-L	Full, load-controlled

3.2.4.1 Hollow tubes

The only difference between Beam 2a and Beam 3a was the lamina structure, so they have the same mesh size, applied load, and boundary conditions. A mesh sensitivity test was conducted to find out the appropriate approximate global mesh size, which was found to be 7 mm based on convergence of load-deflection and load-strain results. Table 3.8 shows the results of the test for Beam 2a. Figure 3.8 shows the load-deflection and the load-strain relationships of models with different mesh sizes. The models simulated four-point bending tests, so loads were applied at the top of the beams near the mid-span in the x direction, as shown in Fig. 3.9. To simulate the boundary condition for a four-point bending test, a single line of nodes at the bottom of the tube at the left support was restricted in the x and y directions. The sliding and rotation were allowed to simulate the roller condition. At the right support, a single line of nodes at the bottom of the tube was restricted in x, y, and z directions. The rotation was still allowed at this support, but the sliding was constrained. Figure 3.10 shows the boundary conditions of the two supports.

Table 3.8 Mesh sensitivity test for Beam 2a

Mesh size	Failure load (kN)	Strain (Tension/Compression)	Deflection (mm)
14	18	0.00924/-0.00915	35.4
7	17	0.00854/-0.00847	33.4
3	17	0.00867/-0.00858	33.2

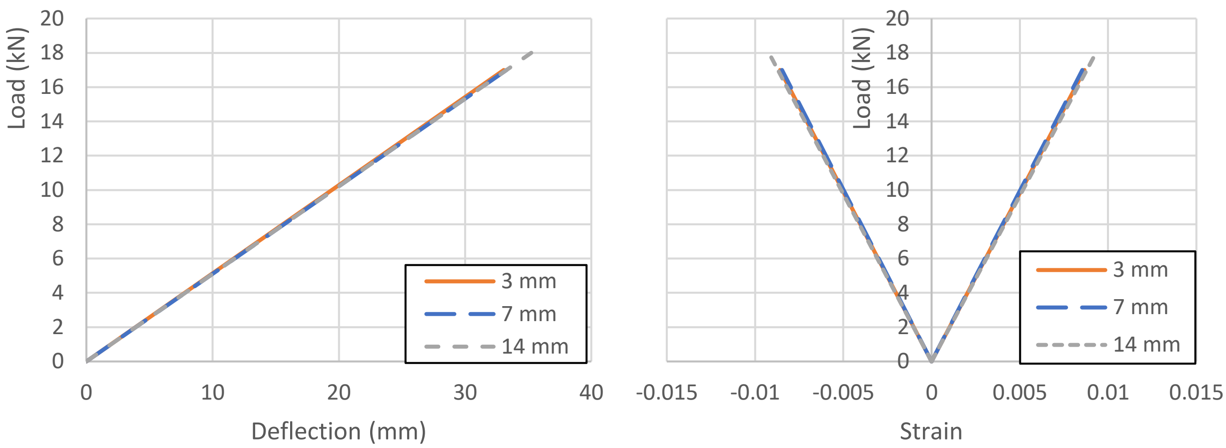

Figure 3.8 Mesh sensitivity test (a) Load-deflection relationship (b) Load-strain relationship

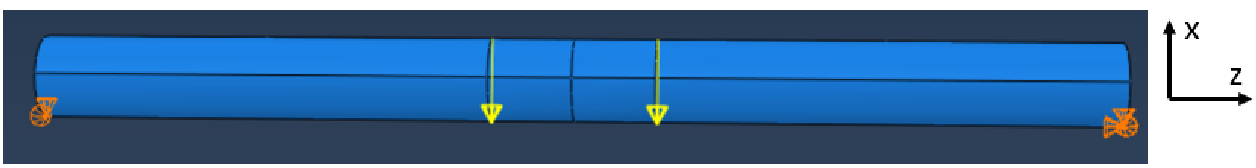

Figure 3.9 Applied loads of Beam 2a

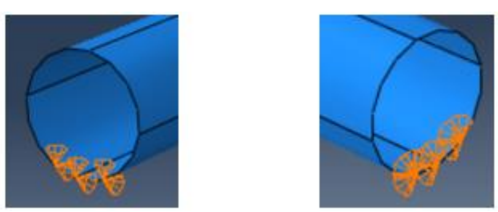

(a) (b)

Figure 3.10 Boundary conditions of Beam 2a at (a) Left support (b) Right support

3.2.4.2 CFFT beams

Four different CFFT beams were modeled, but due to the different modelling methods and parameters used, six beam models were examined in total. The smallest beam was modeled as a whole beam (Beam 2b) and a quarter of the beam (Beam 2b-Q). Meanwhile, the quarter model was tested using two different concrete models (Hognestad concrete model and Mander's concrete model) to see the effect of concrete constitutive models and to save time and computational cost since the beams are symmetric with both the x-y plane and x-z plane. The quarter beam was cut both in length and in the cross-section. The slight asymmetry in the laminate structure in the quarter beam was ignored to simplify the modelling step and satisfy the requirement of symmetric models, since the angle-ply was [3/88] and was close to [0/90]. The results of model Beam 2b-Q were compared to model Beam 2b to verify this assumption and test the influence of the laminate structure. Three larger beams (Beam 4, Beam 12, and Beam 13) were only modeled as full beams due to fibre orientations which were not symmetric, as mentioned in Table 3.3. They were also only modeled using Hognestad's concrete model.

For the four whole beams (Beam 2b, Beam 4, Beam 12, and Beam 13), loading conditions were the same as those used for the hollow tube models. However, local stress concentrations were observed at the right support. To reduce these concentrations, the z-direction constraint at the right support was released, and the nodes at the mid-span were restricted in the z-direction to avoid sliding (Fig. 3.11). Mesh sensitivity tests were conducted, and the approximate global mesh size of Beam 2b was set to 15 mm (Fig. 3.12).

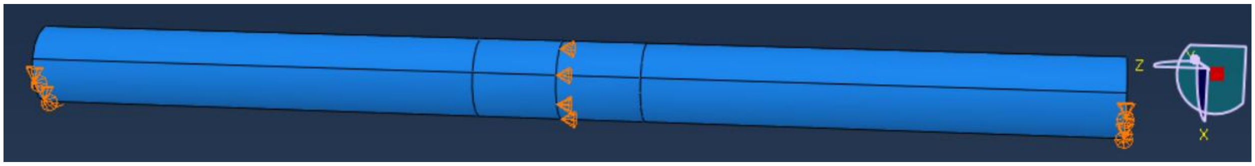

Figure 3.11 Constraints on Beam 2b

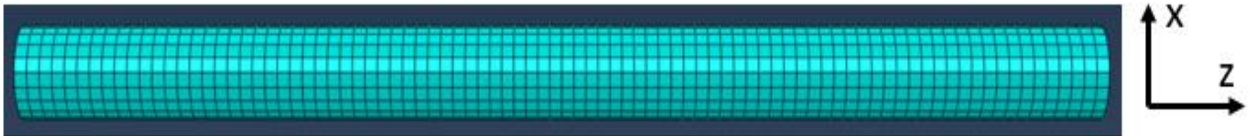

Figure 3.12 The meshed model of Beam 2b

For the two quarter models Beam 2b-Q and Beam 2b-M, only a quarter of the loads was applied. Figure 3.13 shows the constraints and load applied on model Beam 2b-Q. At the mid-span, all nodes at the cross-sectional plane were constrained in the z-direction to produce a symmetry condition. All the nodes at the x-z symmetry plane were also constrained in a similar way in the y-direction. At the bottom of the right end (support), the model was restricted in x and y direction at a single line of nodes, so sliding and rotation were allowed.

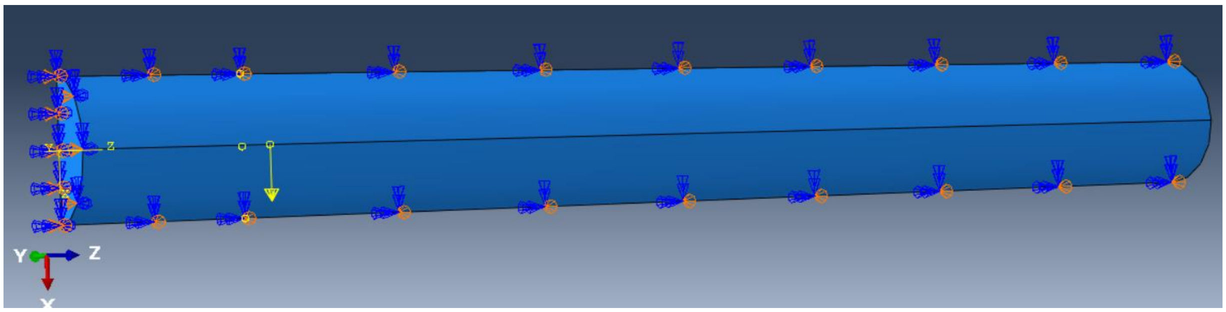

Figure 3.13 Constraints and load on Beam 2b-Q

The size difference between the four beams was huge, so different mesh sizes were used for each model. Mesh sensitivity tests were done for each beam in the same way as those conducted for the hollow tubes, and following some preliminary simulations, the mesh sizes between the mid-span and the loading point were further reduced for Beam 2b-Q and Beam 2b-M to avoid stress concentrations, as shown in Fig. 3.14 (a) and summarized in Table 3.9. Beam 12 was much larger than Beam 2b, so the mesh sizes were also larger; hence, to satisfy the accuracy requirement, as well as save computational time, a finer mesh was used for two parts of the beam model. The width of the fine mesh area at the top of the model was 100 mm, and the width of the fine mesh area near the load point was 200 mm centred around the loading point. For Beam 13, one more fine mesh area was selected near the mid-span with a width of 100 mm. Between the midspan and loading point, the mesh size used there for model Beam 13 was 50 mm.

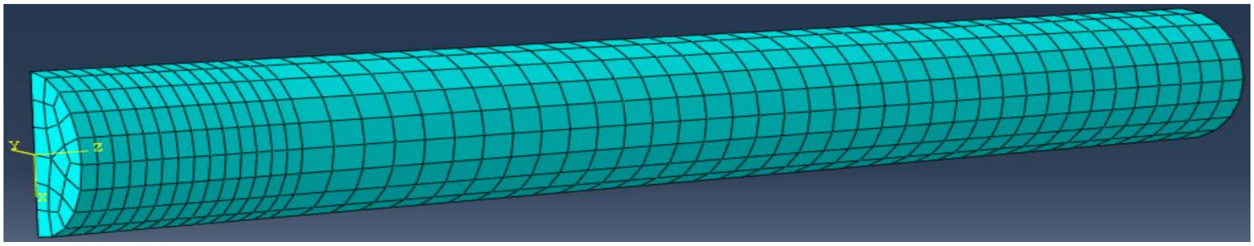

(a)

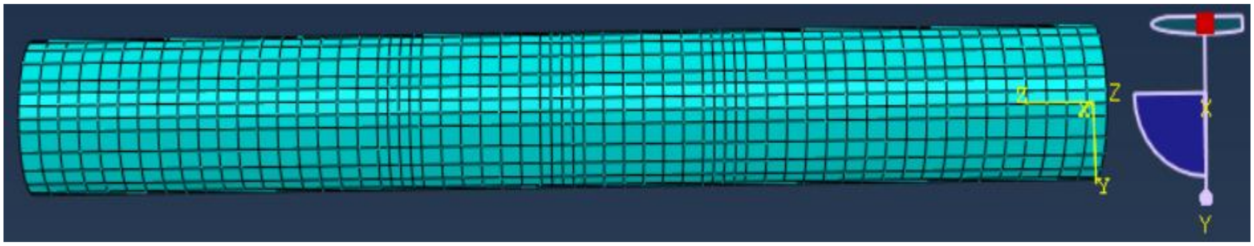

(b)

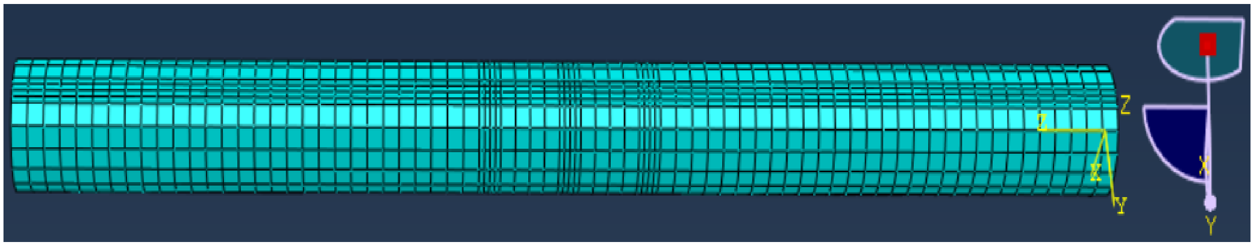

(c)

Figure 3.14 Mesh for (a) Beam 2b-Q (b) Beam 12 (c) Beam 13

Table 3.9 Mesh size of five models

Beam number	Mesh size coarse/fine (mm)
2b-Q	15/7
2b-M	15/7
4	15/7
12	90/50
13	150/50

3.2.4.3 CFFT stubs

Eight different models (Stub 1-D, Stub 1-L, Stub 4-D, Stub 4-L, Stub 8-D, Stub 8-L, Stub 11-D, and Stub 11-l) were developed and compared to experimental results of four different stub geometries (Stub 1, Stub 4, Stub 8, and Stub 11). Two different loading methods were used: load-controlled loading (model -L) and displacement-controlled loading (model -D).

Two different concrete constitutive models were used to model Stub 1, Stub 4, Stub 8, and Stub11.

Mesh sensitivity tests were conducted for each stub; the deflection was not considered for the stub models, since it was not an important parameter for stubs. Figure 3.15 presents the load-strain relationships of Stub 1 with different mesh sizes. Table 3.10 shows the results for Stub 1, and Table 3.11 shows the approximate global mesh size of the different stubs. Figure 3.16 (a) shows the meshed Stub 11.

Figure 3.16 (b) shows the applied load or displacement and constraints on Stub 11. RP-1 and RP-2 in the figure were coupled with the top surface and bottom surface of the stub, respectively, so that the entire bottom surface of the stub was vertically fixed, which means the stub cannot rotate or move. Meanwhile, load or displacement was applied to the entire top surface of the stub.

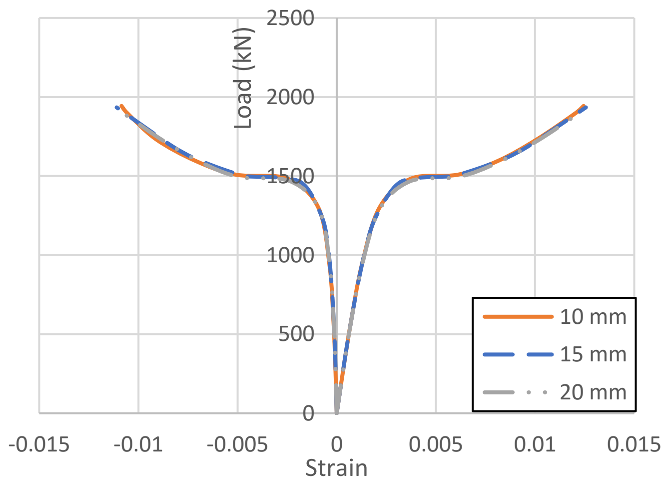

Figure 3.15 Mesh sensitivity test for Stub 1: load-strain relationships

Table 3.10 Mesh sensitivity test for Stub 1

Mesh size	Strain (10^{-3}) (Tension/Compression)	Failure load (kN)
20	12.0/-10.6	1889
15	12.5/-11.1	1934
10	12.4/-10.8	1943

Table 3.11 Mesh sizes of stubs

Stub number	Mesh size (mm)
1	15
4	12
8	20
11	7

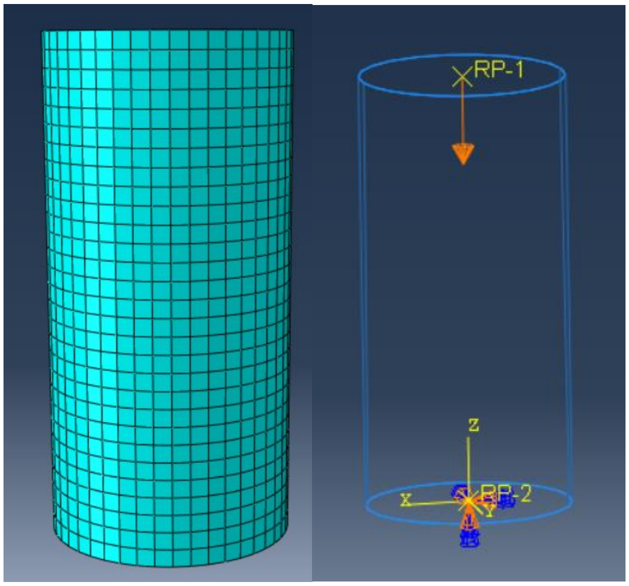

(a) (b)

Figure 3.16 Stub 11 (a) Meshed model (b) Load and constraints

3.3 Results

Finite element results were obtained after the simulations and are compared to experimental results in this section. The primary model outputs used for comparison with the experimental results include mid-span deflection, and longitudinal strain at the top and bottom of the tubes in the maximum moment region.

3.3.1 Hollow tubes

Both experimental and finite element results show that Beam 2a, which was a filament-wound tube with nine layers, can resist a higher load than Beam 3a, which was a pultruded tube and only had one layer. Overall, the modelling results were promising as the load-deflection relationships obtained were in excellent agreement with the experimental results. Regarding the load-strain relationships, the finite element results of Beam 3a were close to the experimental results up to the failure load, with the exception of some non-linear behaviour immediately prior to failure that was not captured. On the other hand, at the top of the tube, the compressive strain obtained from the model Beam 2a was 22.0% larger than the experimental result, while at the bottom of the tube, the tensile strain obtained from the FEM result was 56.9% larger than the experimental result. The possible reason for the error might be the possible local damage/instability that occurred during the experiments which was not obtained by the model.

The failure modes shown in Fam's study for Beam 2a was shell crushing on the compression side near the loading point. Ovalization of the cross-section occurred before the failure. Beam 3a, though it had the same tube thickness and geometric shape as Beam 2a, had a different failure mode because of the different laminate structure. It failed at the loading point due to local crushing and lateral splitting of the shell. Figure 3.17 shows the experimental failure mode, finite element deflected shape, and strain distribution at failure for Beam 2a. Figure 3.18 shows the Tsai-Wu failure index of Beam 2a. It is clear that failure occurred at the loading point, which is the same as the experimental result.

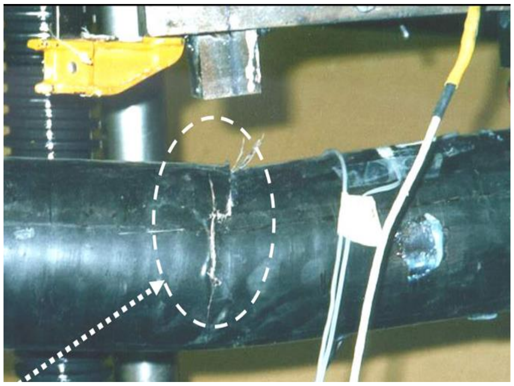

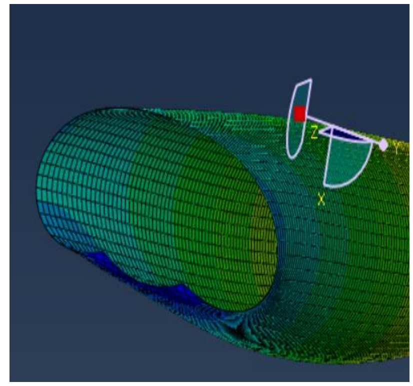

(a) (b)

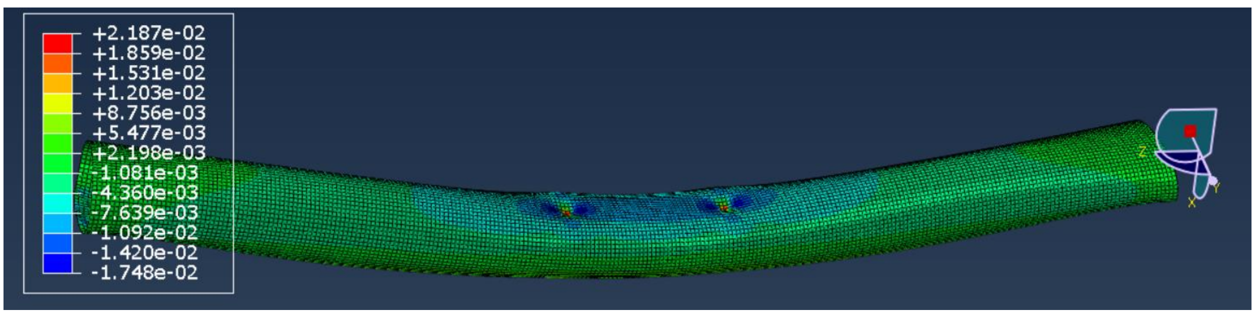

(c)

Figure 3.17 Beam 2a (a) Failure (b) Ovalization (Fam, 2000) (c) Strain distribution at failure

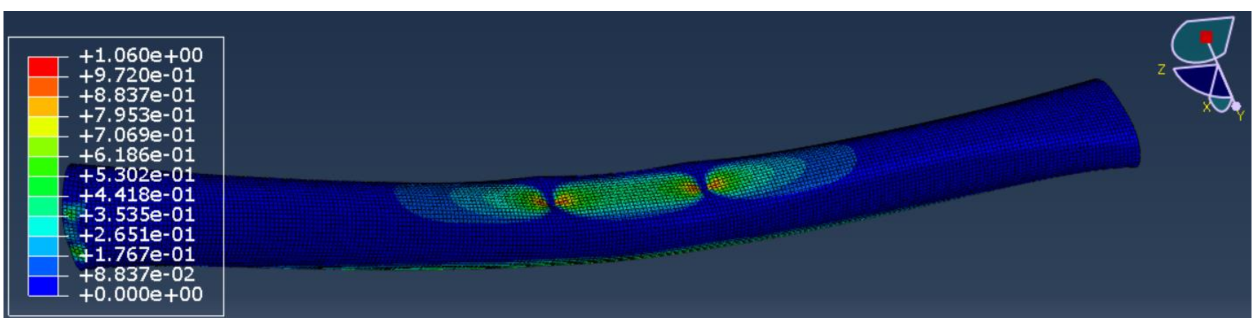

Figure 3.18 Tsai-Wu failure criterion of Beam 2a

Table 3.12 compares the finite element modelling results to the experimental results in displacement and load capacity.

Table 3.12 Comparison of load capacity and displacement

	Beam 2a	Beam 3a
L_e (N)	17000 (100%)	11912 (99%)
L_a (N)	17000	12000
D_e (mm)	33.3 (98%)	20.5 (98%)
D_a (mm)	34.0	21.0
D_{e40} (mm)	13.2 (102%)	8.4 (93%)
D_{a40} (mm)	13.0	9.0

In which L_e is estimated load capacity calculated using Tsai-Wu failure criterion using FEM; L_a is the actual load capacity obtained in Fam's study; D_e is the estimated ultimate displacement obtained using the models; D_a is the actual ultimate displacement according to experiments; D_{e40} is the estimated displacement at 40% of ultimate load using FEM; D_{a40} is the actual displacement at 40% of ultimate load in experiments.

Figure 3.19 and Fig. 3.20 show the FEM and experimental load-deflection relationships and load-axial strain relationships of Beam 2a and Beam 3a at mid-span, respectively.

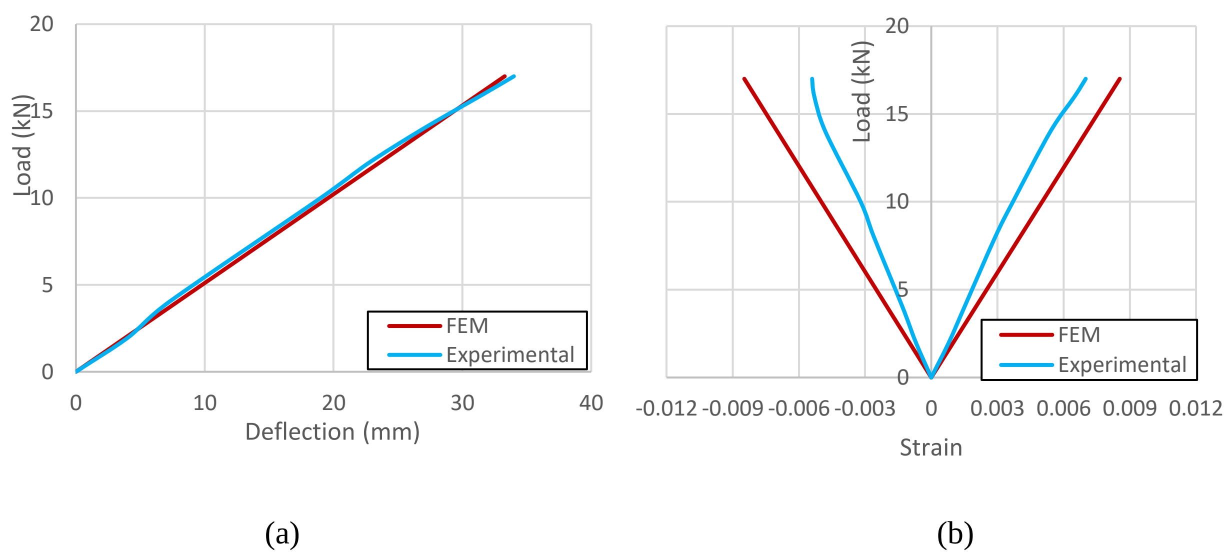

Figure 3.19 Beam 2a (a) Load-deflection relationship (b) load-axial strain relationship

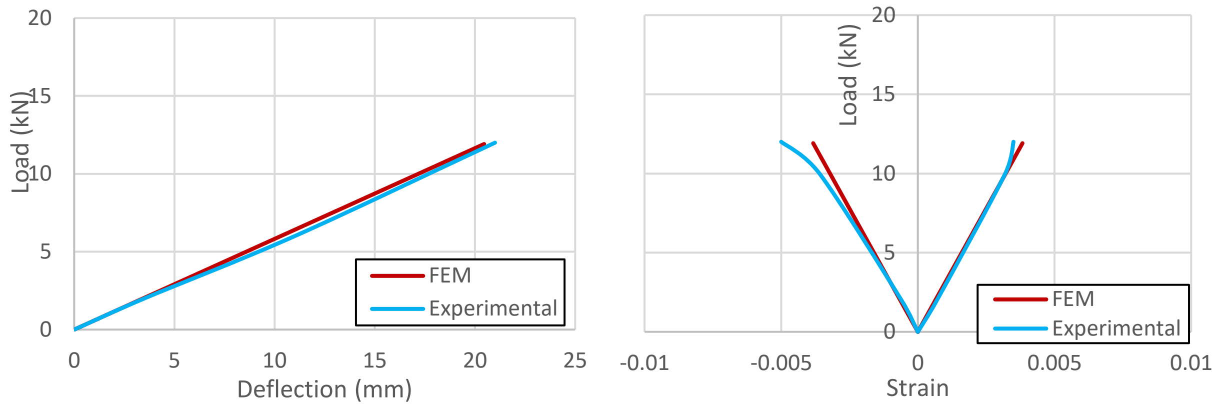

(a) (b)

Figure 3.20 Beam 3a (a) Load-deflection relationship (b) Load-axial strain relationship

3.3.2 CFFT beams

The results of Beam 2b-Q are compared to another quarter beam model, Beam 2b-M, which was developed using Mander's concrete model to examine the influence of different concrete constitutive models. The load-deflection relationship and load-axial strain relationship are shown in Fig. 3.21. The results of the two models using different concrete constitutive models agree well, but the failure load of model Beam 2b-Q is 5.0% larger than model Beam 2b-M, as shown in Table 3.10.

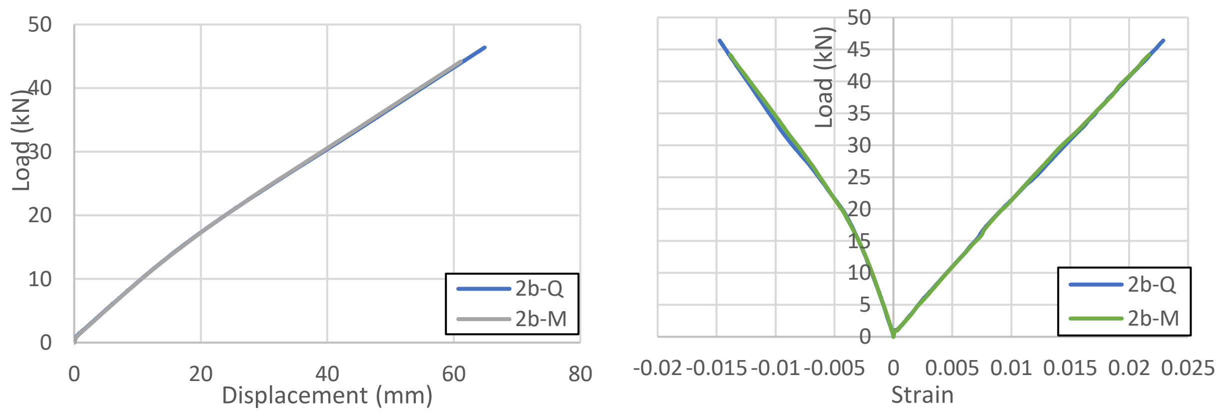

(a) (b)

Figure 3.21 Beam 2b-Q and Beam 2b-M (a) Load-deflection relationship (b) Load-axial strain relationship

To test the difference of the full model and the quarter model, results of Beam 2b and Beam 2b-Q were compared to each other. As shown in Fig. 3.22, the two models had virtually identical mid-span deflections. The mid-span compressive strain of the two models at the top surface were similar, but model Beam 2b-Q had a 6.5% higher mid-span tensile strain at the bottom surface, and a 3.9% lower failure load. Nonetheless, the error between the quarter model and the full model was acceptable. The reason for the difference might be the slight difference in the laminate structure since the full model had a slightly asymmetric [3/88] laminate structure. Another possible reason for the error might be the different mesh sizes since Beam 2b-Q had a finer mesh at the mid-span.

The FEM ultimate loads of model Beam 2b, Beam 2b-Q, and Beam 2b-M were 4%, 7.2%, 11.6% lower than experimental results, respectively. Model Beam 2b had the best agreement with actual results, with a 4.9% lower deflection at the ultimate load, 5.0% higher deflection at 40% of the ultimate load, 8.9% lower tensile strain, and 2.5% lower compressive strain than actual results. While the results of model Beam 2b-Q are acceptable with a 7.3% lower deflection at the ultimate load, 0.5% lower deflection at 40% of the ultimate load, 2.3% and 8.1% lower tensile and compressive strain at the mid-span, respectively, than actual results. However, the error of model Beam 2b-M is larger, as shown in Table 3.10, due to the low estimated ultimate load. Taking time and computational cost into consideration, using quarter model and Hognestad concrete constitutive model is considered a suitable method to model the beams.

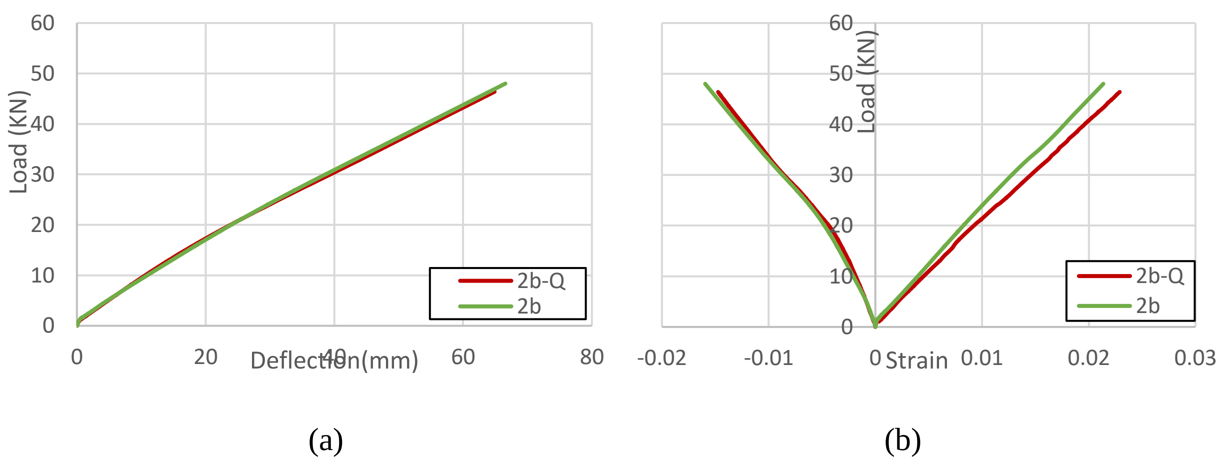

Figure 3.22 Beam 2b and Beam 2b-Q (a) Load-deflection relationship (b) Load-axial strain relationship

In general, good agreement was observed between the experimental and numerical results for all six models, especially for the load-deflection relationship and load-strain relationship in tension. The experimental tests tended to show a slightly greater stiffness likely associated with tension stiffening that was not captured by the models. However, though the four models of smaller beams (Beam 2b, Beam 2b-Q, Beam 2b-M, and Beam 4) had good results for the compressive strain at the top surface, the compression strain at failure of the two larger beams (Beam 12 and Beam 13) was slightly less accurate compared to the experimental compressive strain results. The estimated ultimate load of Beam 12 was 1% lower than actual ultimate load, while for Beam 13, the estimated value was 2.6% higher. The corresponding error in the results of these two beams in terms of ultimate deflection were 2% and 26.0% lower than actual deflection at ultimate load, respectively. The tensile strain of Beam 12 was about 13.6% higher than the actual strain, while for Beam 13, it was about 1.4% lower. The compressive strain of the two beams was 26.5% and 40.8% lower than experimental results, respectively. The main reason for the error might be the slip between the tube and the concrete core that occurred during the experiments that did not happen during the finite element analysis, since non-slippery connection was used between the FRP tube and concrete core. Other possible reasons for the observed error include inaccuracies associated with the selected constitutive models for the constituent materials and/or contact interactions, the large aspect ratio in meshes, as well as possible local damage in the FRP tube in compression that was not captured by the model. In any case, the overall behaviour of the models was judged to be satisfactory for the purpose of this study. The load capacity, displacement at ultimate load and 40% of ultimate load, and compressive and tensile strain at the mid-span of six models are presented in Table 3.13. Figures 3.23-3.26 indicate the experimental and FEM results of load-deflection relationship and load-axial strain relationship of Beam 2b-Q, Beam 4, Beam 12, and Beam 13.

Table 3.13 Comparison of load capacity, displacement, and strain

	Beam 2b	Beam 2b-Q	Beam 2b-M	Beam 4	Beam 12	Beam 13
L_e (kN)	48.0 (96%)	46.4 (93%)	44.2 (88%)	31.0 (95%)	535.1 (99%)	718.6 (103%)
L_a (kN)	50.0	50.0	50.0	32.5	540.0	700.0
D_e (mm)	66.6 (95%)	64.9 (93%)	61.1 (87%)	103.6 (90%)	105.7 (98%)	200.0 (74%)
D_a (mm)	70.0	70.0	70.0	115.0	108.0	270.0
D_{e40} (mm)	23.1 (105%)	21.9 (99%)	20.6 (94%)	36.6 (131%)	31.1 (120%)	54.3 (121%)
D_{a40} (mm)	22.0	22.0	22.0	28.0	26.0	45.0
ε_{te}	0.0214 (91%)	0.0229 (97%)	0.0217 (92%)	0.0153 (84%)	0.0159 (114%)	0.0146 (99%)
ε_{ta}	0.0235	0.0235	0.0235	0.0182	0.0140	0.0148
ε_{ce}	-0.0156 (98%)	-0.0147 (92%)	-0.0139 (87%)	-0.00543 (72%)	-0.00610 (73%)	-0.00503 (59%)
ε_{ca}	-0.0160	-0.0160	-0.0160	-0.00750	-0.00830	-0.00850

In which ε_{te} is the estimated tensile strain at the bottom of the beam at mid-span obtained using FEM; ε_{ta} is the actual tensile strain obtained in Fam's experiments; ε_{ce} is the estimated compressive strain at the top of the beam at mid-span; ε_{ca} is the actual compressive strain according to experiments.

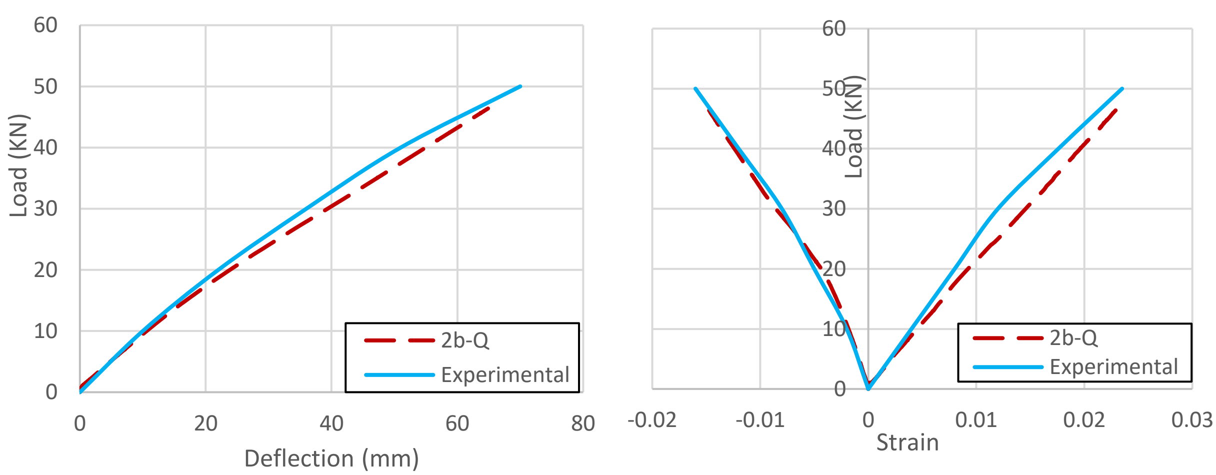

(a) (b)

Figure 3.23 Beam 2b-Q (a) Load-deflection relationship (b) Load-axial strain relationship

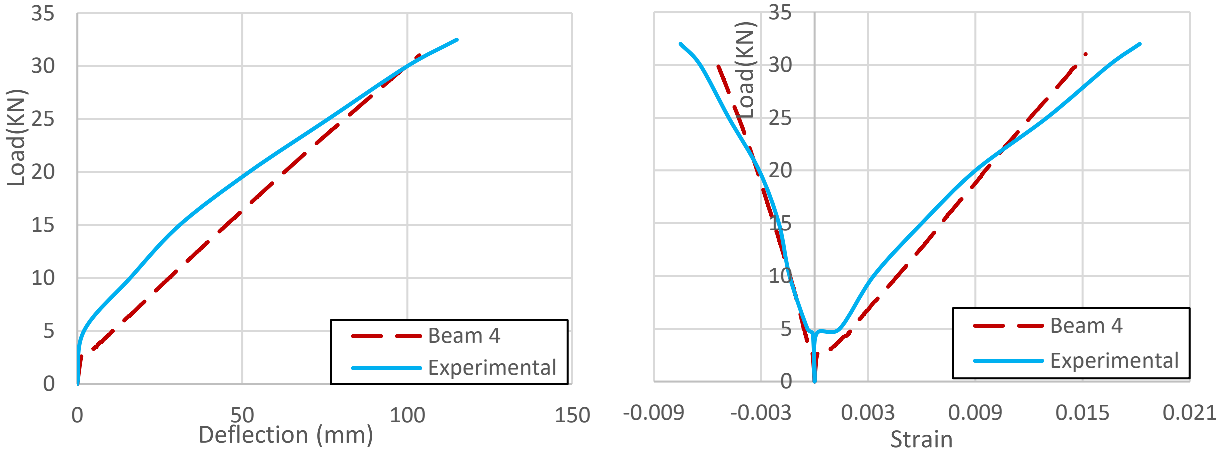

(a) (b)

Figure 3.24 Beam 4 (a) Load-deflection relationship (b) Load-axial strain relationship

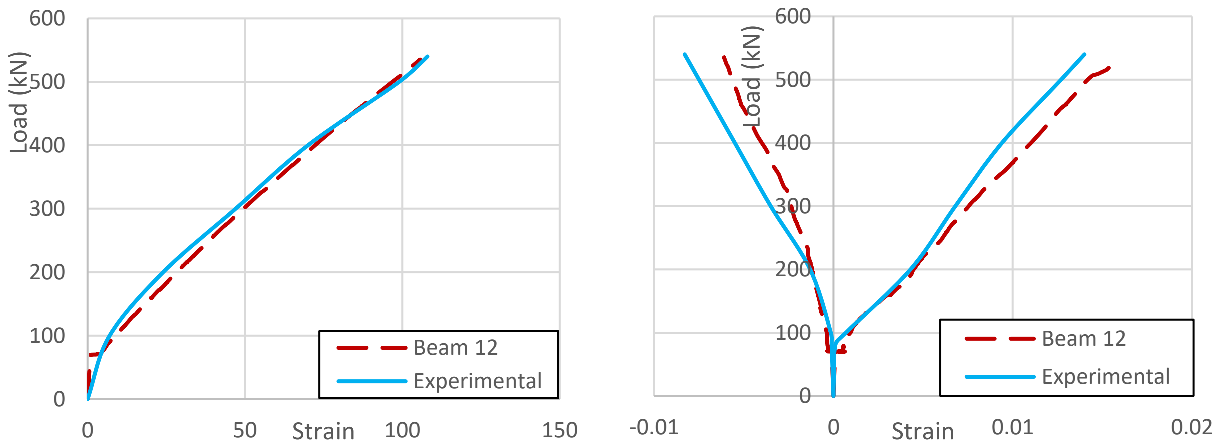

(a) (b)

Figure 3.25 Beam 12 (a) Load-deflection relationship (b) Load-axial strain relationship

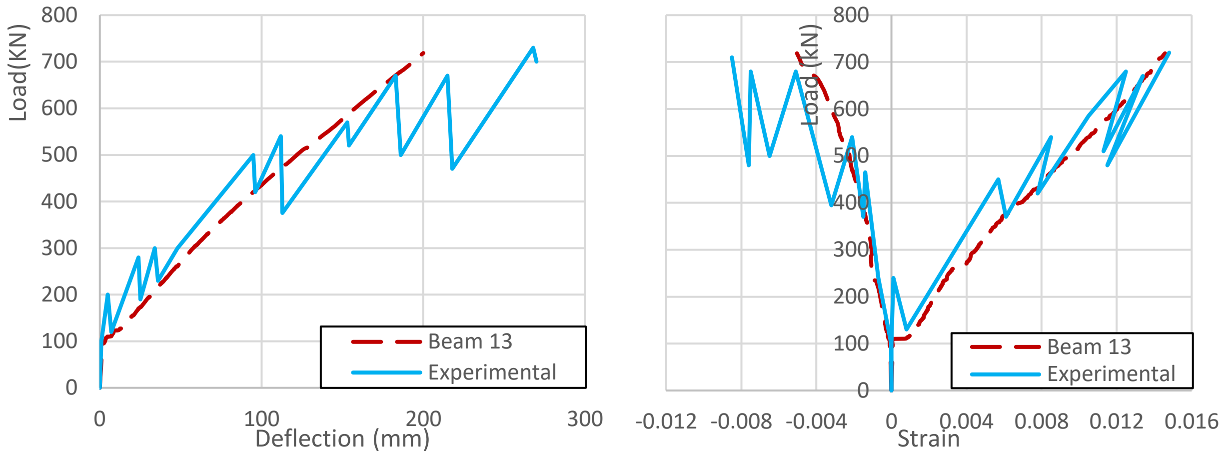

(a) (b)

Figure 3.26 Beam 13 (a) Load-deflection relationship (b) Load-axial strain relationship

In Fam's study (2000), Beam 2b had the same FRP laminate structure as Beam 2a and failed by FRP rupture at the tension side. Beam 4 failed in the same way as Beam 2b and the failure area was near the mid-span. In the finite element analysis, failures were obtained using Tsai-Wu criterion. Figure 3.27 (a) shows the failure mode and Tsai-Wu criterion of Beam 2b-Q, which is similar to Beam 2b-M and Beam 4 and agrees well with experimental results. Beam 12 and Beam 13, however, unlike the two smaller beams, failed at the loading point during the finite element analysis, as shown in Fig. 3.27 (b). In the experiment, Beam 12 failed between two loading points, which is slightly different from the FEM result, while Beam 13 failed at the left loading point. Both beams experienced a flexural tension failure, and the slip was also observed after the experiments. At each end, the slip in Beam 12 was measured as 9.0 and 10.0 mm, respectively. In Beam 13, the total slips measured at right and left ends were 14.0 and 22.0 mm at the top of the beam, and 10.0 and 15.0 mm at the bottom. During the simulations, the slip was not considered, so this is one important reason for the errors observed in the FE results. It should be noted that various methods have been developed to minimize slip between the FRP tube and concrete, and thus a no-slip assumption would be reasonable for those applications.

(a)

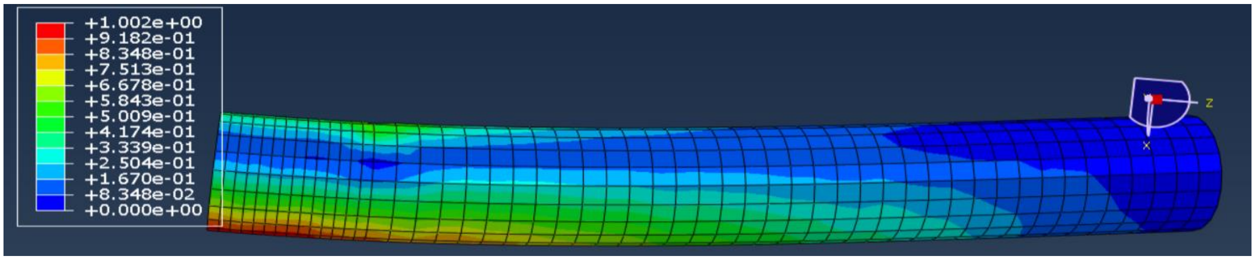

(b)

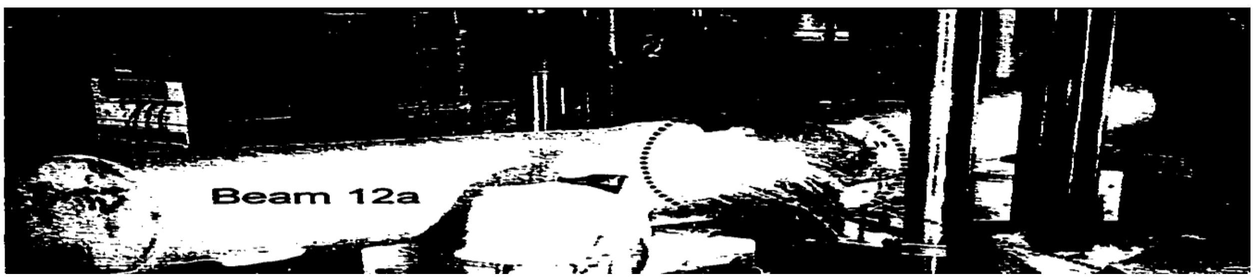

(c)

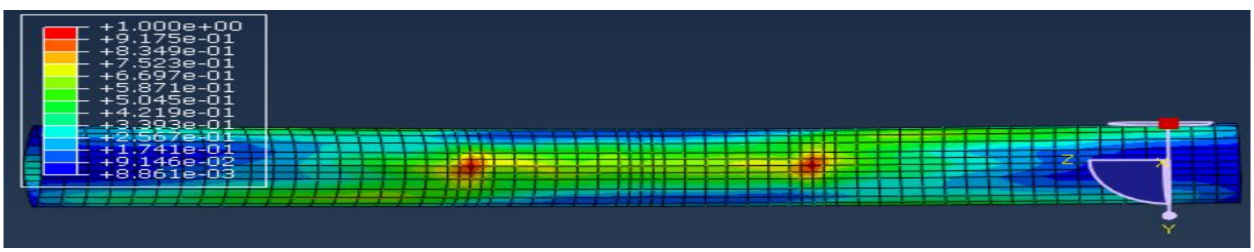

(d)

Figure 3.27 Failure mode and Tsai-Wu criterion (a) Experiment: Beam 2b (b) FEM: Beam 2b-Q (c) Experiment: Beam 12 (d) FEM: Beam 12

Figure 3.28 (a) and (b) show the strain distribution and deformed shape of Beam 2b-Q and Beam 12, respectively. For the two beams, the maximum tensile and compressive strain areas were both between the loading points near the mid-span.

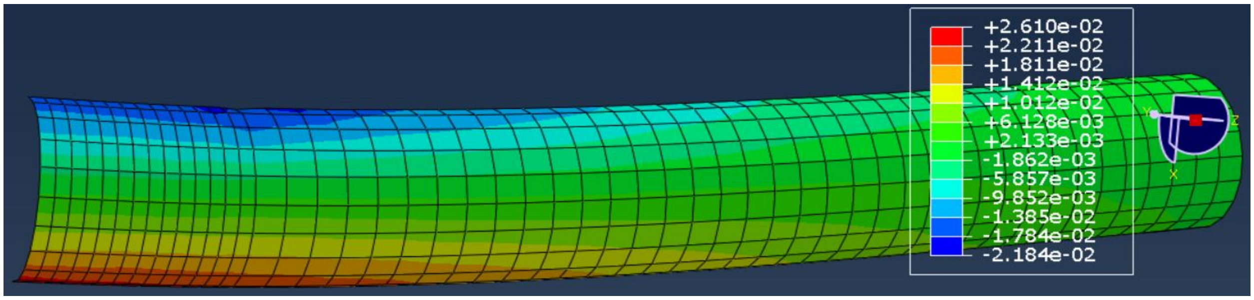

(a)

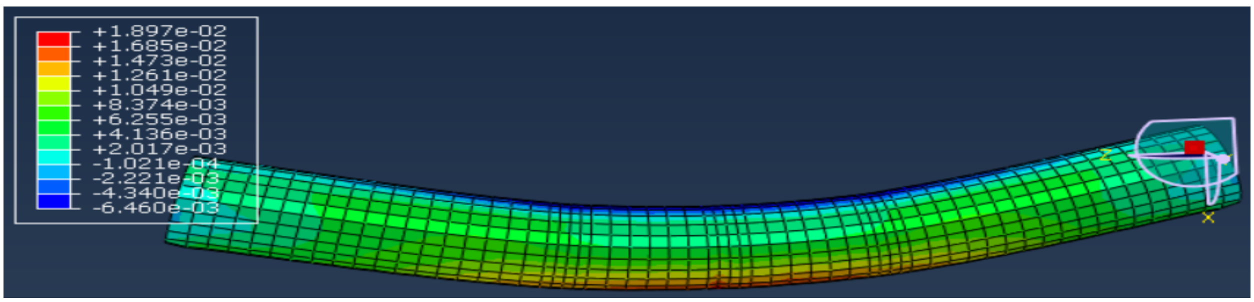

(b)

Figure 3.28 Strain distribution (a) Beam 2b-Q (b) Beam 12

3.3.3 CFFT stubs

Four stubs were modelled under load-controlled and displacement-controlled loading conditions, as shown in Table 3.5 and Table 3.7. The two methods were compared to each other since the wind turbine tower models can only be developed using load-controlled method to test the effect of the wind loads and the weight of wind turbine. Figure 3.29 shows the load-deflection relationship of eight models. The deflection of the CFFT stubs were not compared to experimental studies since they were not recorded, but the results present some differences between load-controlled loading and displacement-controlled loading methods. For Stub 1 and Stub 11, similar results were obtained using the different loading methods, but for Stub 4 and Stub 8, the displacement-controlled model exhibited a slight drop in load following an initial peak which was not captured by the load-controlled model. Instead, the load-controlled model showed a constant-load plateau region. For Stub 4, the load-deflection curve also experienced a further linear increase after the plateau. The reason for the zero slope is a sudden deformation that happened when the load was still the same. Taking the phenomenon into consideration, load-controlled models cannot simulate the decrease in applied load, so displacement-controlled models are more appropriate when post-peak behaviour is important.

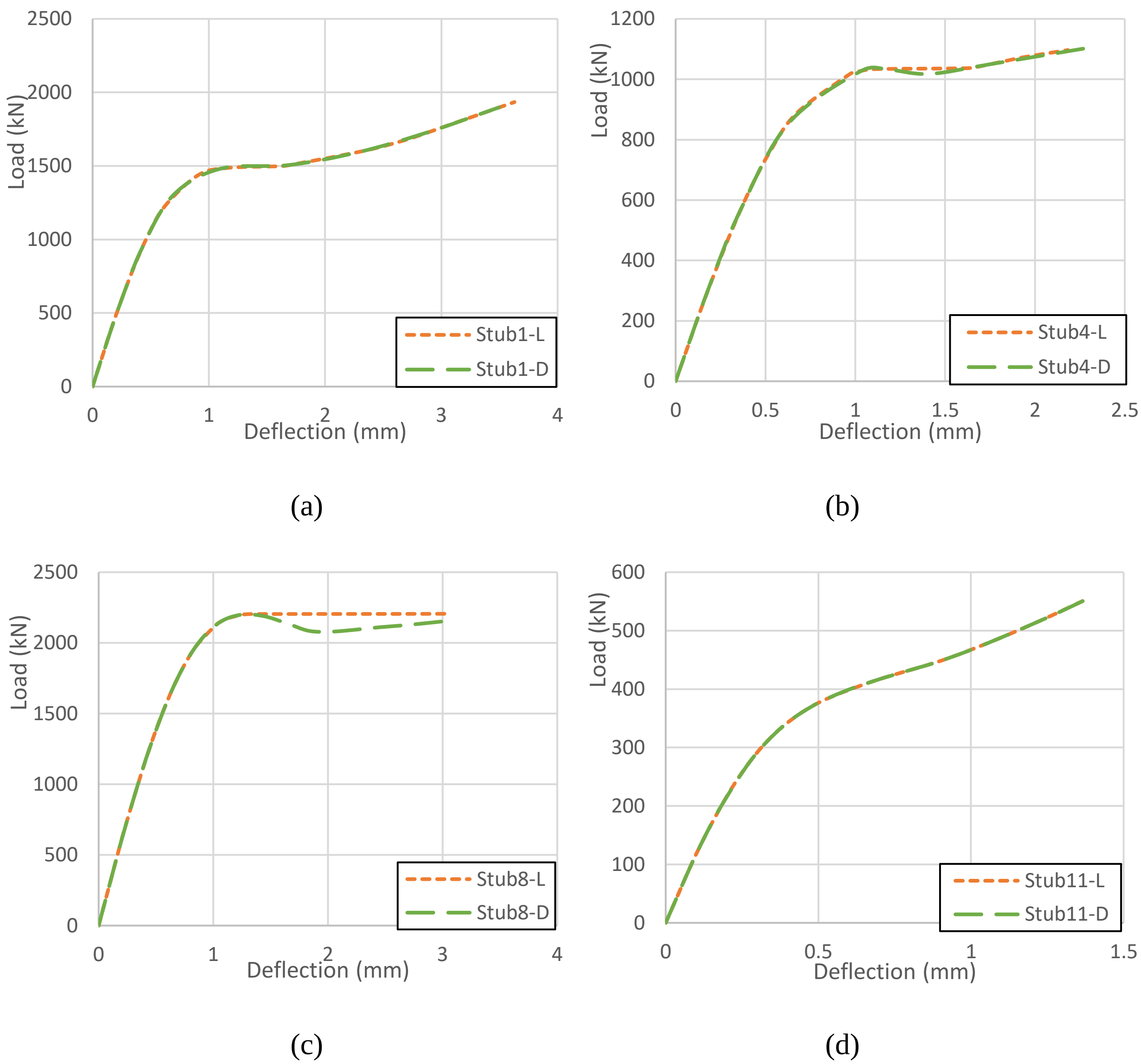

Figure 3.29 Load-deflection relationship of (a) Stub 1 (b) Stub 4 (c) Stub 8 (d) Stub 11

Figure 3.30 shows the concrete stress-strain relationships of Stub 4 and Stub 8. Figure 3.31 shows the stress distribution of Stub 4-D and Stub 8-D. Average concrete stress and strain at the mid-span were calculated in this section. The concrete stress-strain relationship of Stub 4 obtained using two different methods were similar, the estimated maximum stresses were both about 3.5% lower than the actual result. Prior to the plastic deformation stage, FEM results were the same as the experimental results. The estimated peak loads were both slightly lower than the experimental result. The FEM results of Stub 8 had a better agreement with the experimental result in maximum stress. Before the plastic strain region, the estimated value and actual value were close, which is the same as Stub 4. But after the yield point, the load-controlled model actually had a better agreement than displacement-controlled model, though the difference is slight. Stub 4 is a hollow CFFT stub without inner FRP tube; this is one possible reason for the error in the maximum stress and the behaviour after the yield point, since the results for Stub 8, which is a fully-filled CFFT stub, agreed better with experimental results, as shown in Fig. 3.30 (b). Other possible explanations for observed discrepancies include the inaccuracy of the constitutive model and the use of an ideal contact interaction that did not take slip into consideration. Nevertheless, the results were quite satisfactory overall.

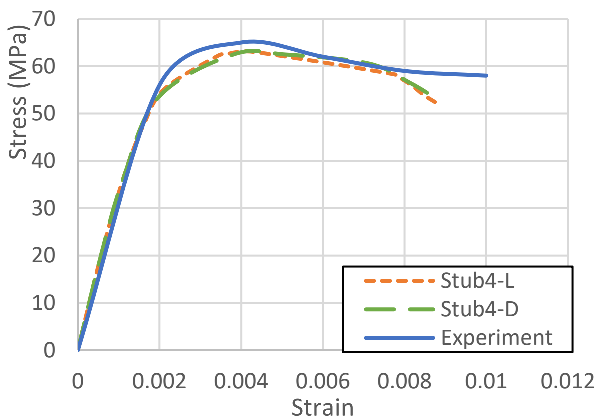

(a)

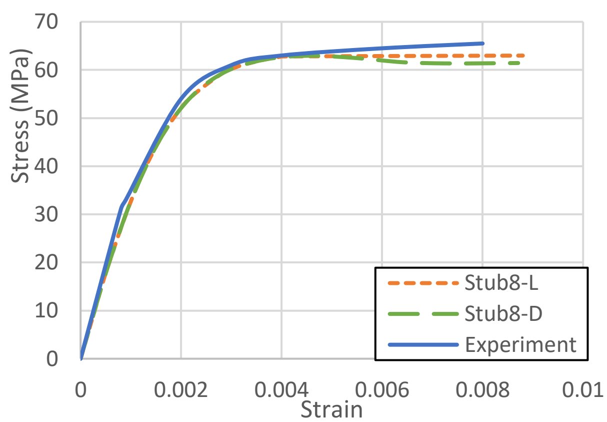

(b)

Figure 3.30 Concrete stress-strain relationship of (a) Stub 4 (b) Stub 8

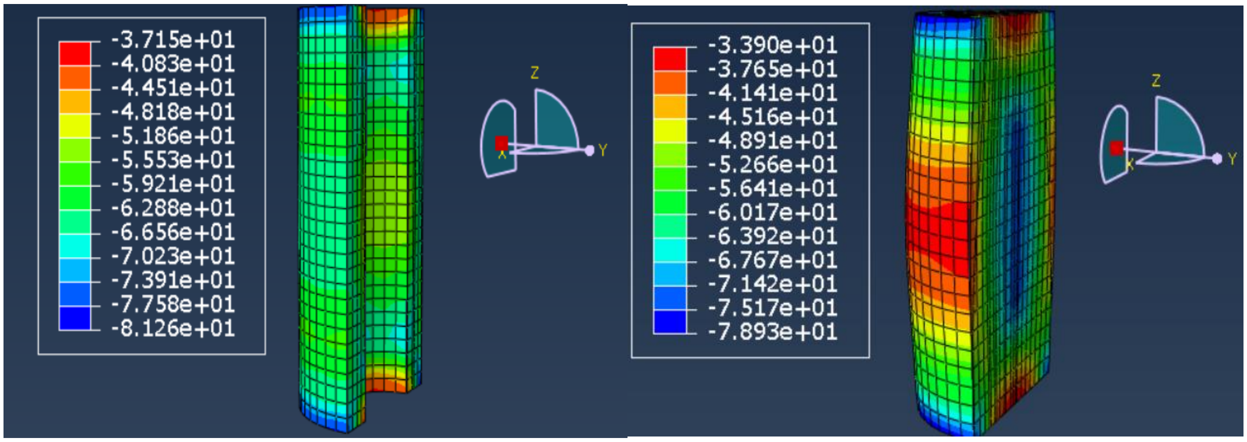

(a) (b)

Figure 3.31 Concrete axial stress (MPa) distribution (a) Stub 4-D (b) Stub 8-D

The concrete load-strain relationships of Stub 11 calculated using different methods had a good agreement with experimental results, as shown in Fig. 3.32. There is no difference in the two estimated load-strain curves, agreeing with the previous conclusion that different loading methods do not affect the concrete behaviour significantly.

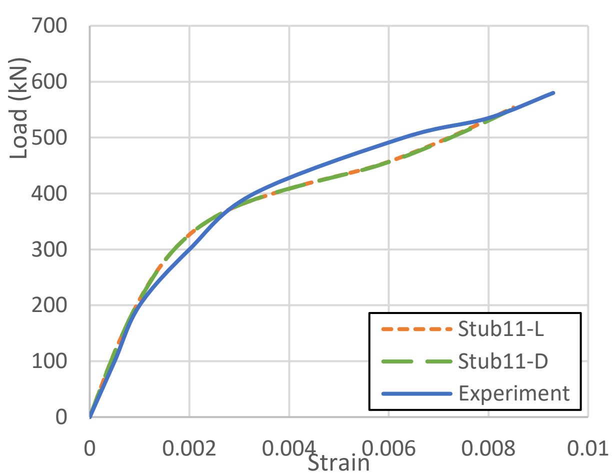

Figure 3.32 Concrete load-strain relationship of Stub 11

The failure was obtained using the Tsai-Wu criterion. All eight different models had the same failure mode, which was FRP rupture at the mid-height of the column. The Tsai-Wu index distribution of these models were also similar. Figure 3.33 presents the failure index of Stub 11-D and Stub 11-L using different loading methods, as well as the failure mode of Stub 11 obtained in the experiment. FRP rupture at the mid height was observed in the figure. Both models failed at the mid height, which were the same as the experimental result. In the experiments, the four stubs had a similar failure mode. They failed in a brittle manner because of shell fracture under the combination of hoop tensile stresses resulting from lateral expansion of the concrete core, and axial compressive stresses resulting from the applied load.

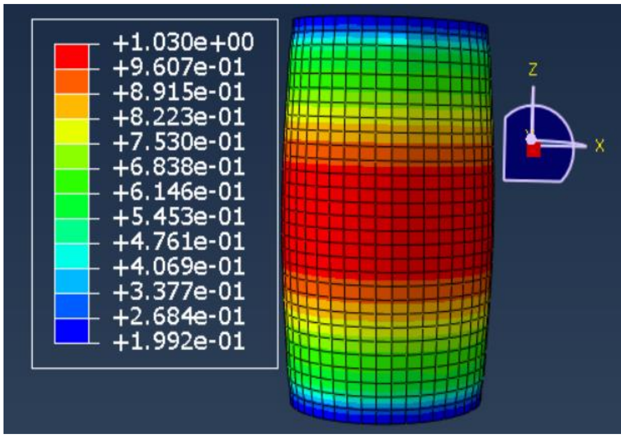

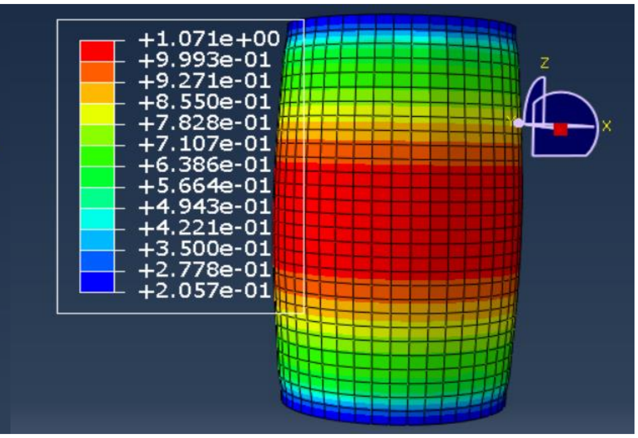

(a) (b)

(c)

Figure 3.33 Tsai-Wu failure index of (a) Stub 11-L (b) Stub 11-D (c) failure mode

Results of stub models using Hognestad concrete model and Mander's concrete model were compared to each other, as shown in Fig. 3.34. All the stubs were analyzed under displacement-controlled models. It is clear that Mander's concrete model had better results than Hognestad concrete model, especially for two fully-filled stub models, Stub 1 and Stub 8. This result is attributed to the fact that Mander's model is more suitable for concrete under confinement, which is more significant for axially loaded specimens. As a result, models made of Mander's concrete model were used in the following comparison between finite element results and experimental results.

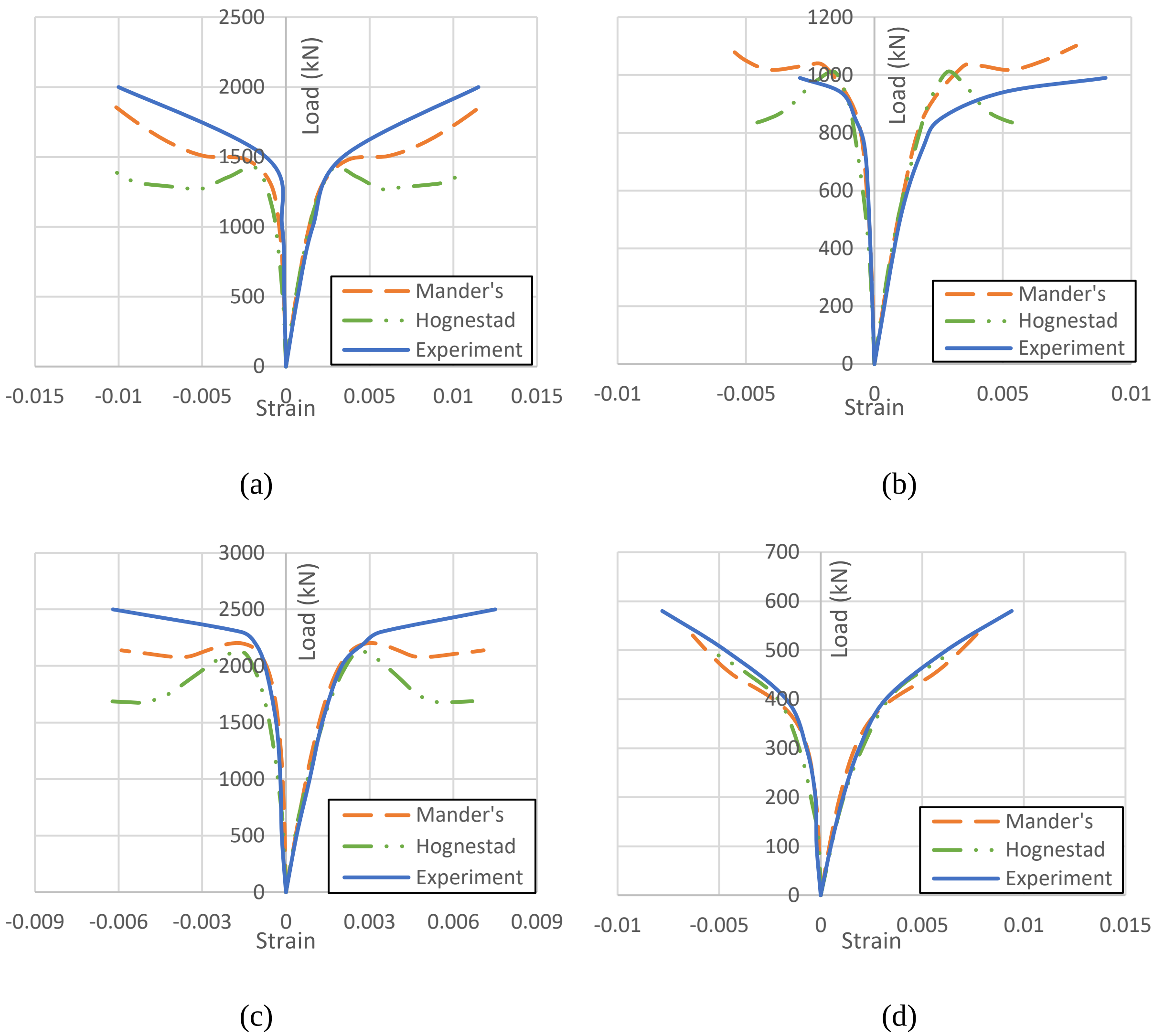

Figure 3.34 Load-strain relationship using different concrete models (a) Stub 1 (b) Stub 4 (c) Stub 8 (d) Stub 11

Figure 3.35 shows the load-FRP strain relationship for all eight models using Mander's concrete model, with axial strains in compression and hoop strains in tension. All the stubs failed due to FRP rupture, which was the same as the experimental results. Except for Stub 4 and Stub 8, FEM results obtained using two different loading methods tended to be similar, which was the same as the load-deflection relationship. Considering the results of Stub 4 and Stub 8, displacement-controlled model results were adopted in this section to compare to experimental results. For Stub 1, Stub 8, and Stub 11, the estimated load capacity of displacement-controlled models were about 3.3%, 11.6%, and 4.5% lower than actual load capacity, respectively. The actual tensile and compressive strain of Stub 1 were 8% and 9.9% lower than estimated results of Stub 1-D. Model Stub 8-D had better results. The estimated tensile strain was the same as experimental tensile strain, and the compressive strain was only 1.6% larger than actual compressive strain. The errors in Stub 11-D were 12.7% and 12.8% for tensile and compressive strain, respectively. The difference between model Stub 4-D and other models were significant. As shown in Fig. 3.35, the estimated load capacity of the other three models were lower than actual load capacity, but Stub 4-D had an 8.8% higher estimated load capacity. The actual tensile and compressive strain of Stub 4-D were 14.4% and 48.1% lower than simulated results. The error in model Stub 4-D is larger than in other models. A possible reason for the difference might be the structure of Stub 4, since it is a hollow stub without inner FRP tube, the confinement effect of the model might be different from other fully-filled stub models. Other possible reasons for the errors in all the models include the inaccuracy of constitutive models and contact properties. The overall behaviour of the models is acceptable for the purpose of the study.

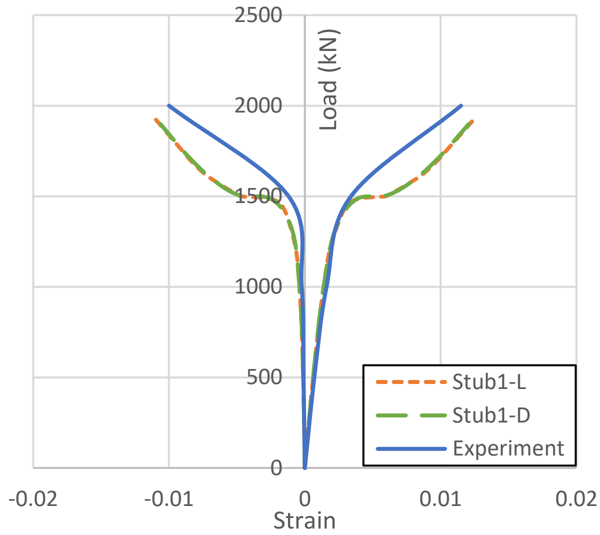

(a)

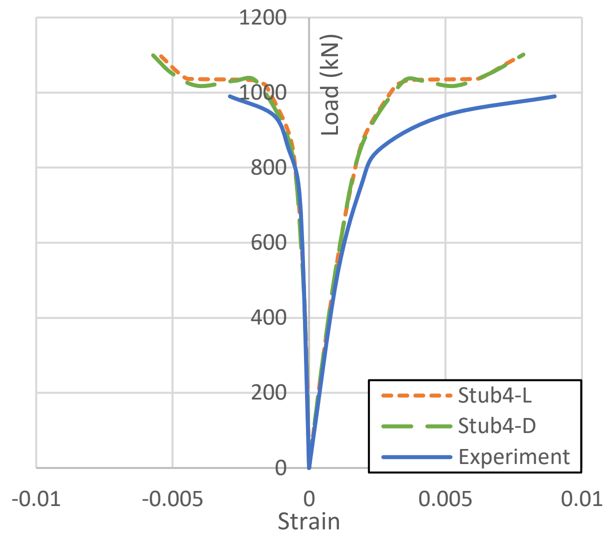

(b)

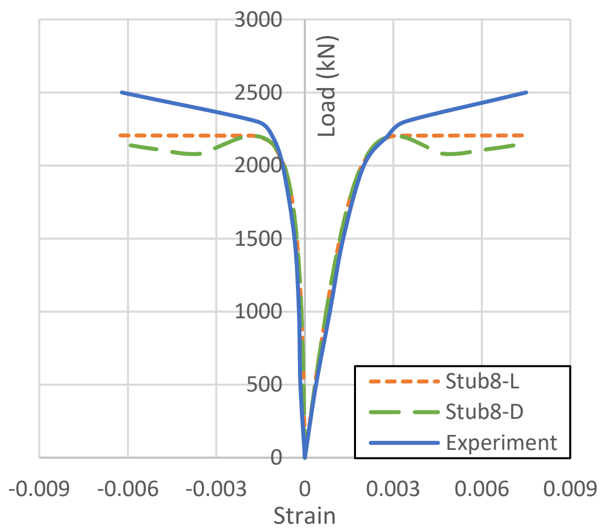

(c)

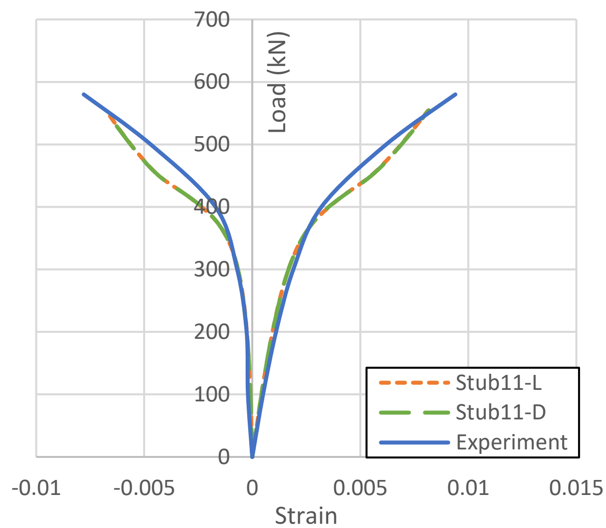

(d)

Figure 3.35 Load-strain relationship of (a) Stub 1 (b) Stub 4 (c) Stub 8 (d) Stub 11

Fig. 3.36 shows the tensile (hoop) and compressive (axial) strain distribution in the FRP of Stub 4-D and Stub 11-D.

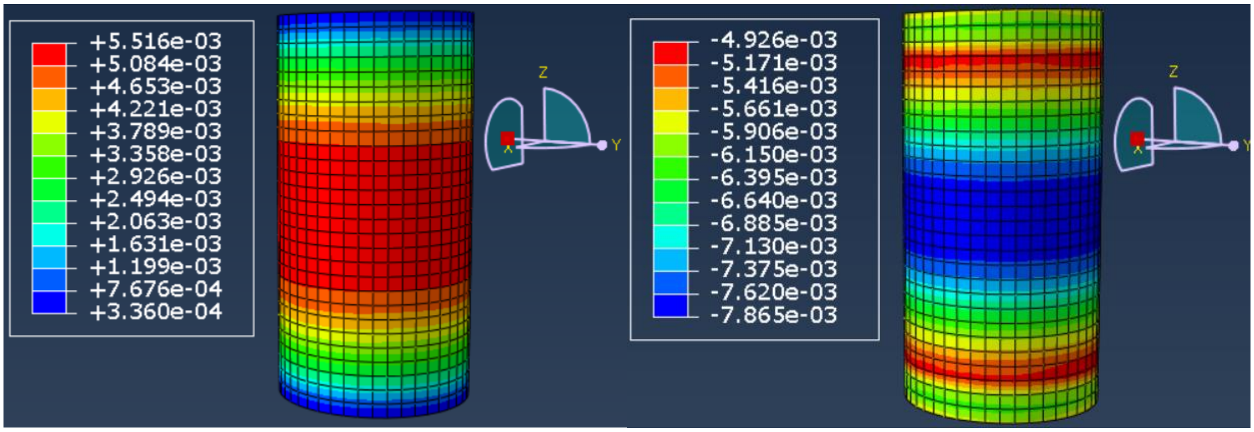

(a) (b)

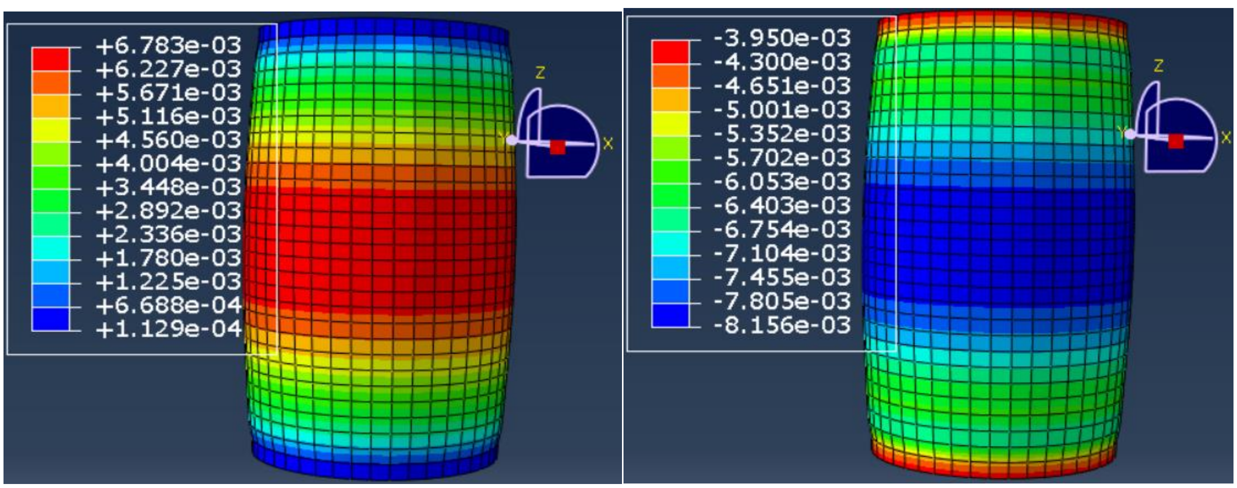

(c) (d)

Figure 3.36 Strain distribution (a) Stub 4-D tensile strain (b) Stub 4-D compressive strain (c) Stub 11-D tensile strain (d) Stub 11-D compressive strain

Table 3.14 presents the estimated and actual load capacity, hoop tensile strain, and axial compressive strain of four stubs and the estimated axial deflection and hoop expansion at the mid-height. The stress and strain presented were the average value around the circumference.

Table 3.14 Actual and estimated values of four stubs

Stub Number	1-L	1-D	4-L	4-D	8-L	8-D	11-L	11-D
L_e (kN)	1900 (95%)	1934 (97%)	1101 (110%)	1097 (110%)	2200 (88%)	2210 (88%)	555 (96%)	554 (95%)
L_a (kN)	2000	2000	1000	1000	2500	2500	580	580
ε_{te} (10^{-3})	12.1 (105%)	12.5 (109%)	7.9 (88%)	7.7 (86%)	7.6 (101%)	7.5 (100%)	8.2 (87%)	8.1 (89%)
ε_{ta} (10^{-3})	11.5	11.5	9.0	9.0	7.5	7.5	9.4	9.4
ε_{ce} (10^{-3})	-10.6 (106%)	-11.1 (111%)	-5.7 (204%)	-5.4 (193%)	-6.4 (103%)	-6.3 (102%)	-6.8 (87%)	-6.8 (87%)
ε_{ca} (10^{-3})	-10.0	-10.0	-2.8	-2.8	-6.2	-6.2	-7.8	-7.8
D_{ae} (mm)	3.50	3.63	2.27	2.18	3.0	3.1	1.38	1.38
D_{he} (mm)	1.0	0.97	0.45	0.49	0.87	0.88	0.34	0.35

In which D_{ae} is the axial deflection, D_{he} is the hoop expansion at mid-height.

Chapter 4 Parametric study

The commercial software ABAQUS was used to conduct a parametric study for small-scale wind turbine towers to investigate the influence of FRP laminate structure, concrete filling ratio, steel reinforcement ratio, prestressing ratio, and taper ratio. A selected model was also used to test the effect of load distributions. The result of a CFFT wind turbine tower under concentrated horizontal load at the top of the tower was compared to the performance of concrete wind turbine towers and steel tubular wind turbine towers. Later, the weight of wind turbine towers made of different materials were considered as a potential factor affecting foundation design and transportation requirements.

4.1 Materials

FRP, steel, and concrete material properties are discussed in this section.

4.1.1 Constitutive models

4.1.1.1 FRP

FRP material properties and failure criterion were assumed to be the same as the material properties of Tube 5, which is a GFRP tube with average material properties and has been discussed in Section 3.2.1.1, except that the laminate structure was changed from [3/88] to [0/90] to satisfy the symmetry requirement.

4.1.1.2 Steel rebar

Steel reinforcing bars were used while modelling concrete wind turbine towers and CFFT wind turbine towers. They were modeled as a perfectly elasto-plastic material, as shown in Fig. 4.1. It has linear elastic properties before yielding and then has plastic properties. After reaching the yield stress, unloading the material can leave deformations.

The elastic modulus E was considered as 200 GPa, Poisson's ratio υ was 0.3, yield stress f_y and the corresponding strain ε_y were 400 MPa and 0.002, respectively. Table 4.1 shows the sizes and material properties of each bar type used in this study.

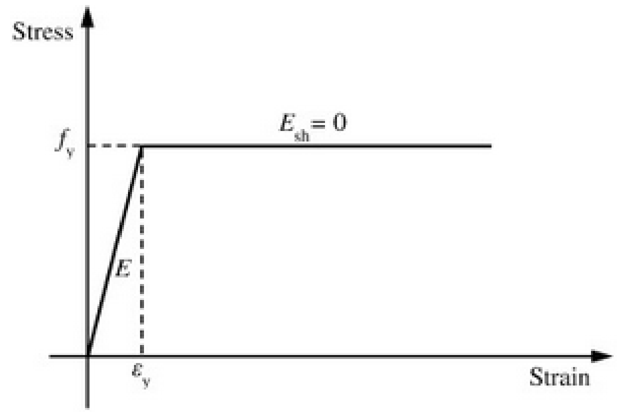

Figure 4.1 Steel stress-strain relationship

Table 4.1 Steel rebar sizes and material properties

Metric bar size	Nominal diameter (mm)	Cross-sectional area (mm^2)	Yield stress f_y (MPa)	Young's modulus (MPa)	Poisson's ratio
30M	29.9	700	400	200000	0.3
45M	43.7	1500	400	200000	0.3

4.1.1.3 Steel tendon

Prestressed tendons were used in the concrete wind turbine tower models and CFFT wind turbine tower models. The elastic modulus and Poisson's ratio were the same as steel reinforcing bars, which are 200 GPa and 0.3, respectively. Prestressing tendons do not have a typical yield point, so according to ASTM standard, the yield stress is obtained at a total strain of 1% for wires and strands. Figure 4.2 indicates the stress-strain curve of prestressing steel, in which f_{pp} is the proportional limit and is considered as the stress at the 0.01% offset; $f_{p0.1}$ is the stress at the 0.1% offset; f_{py} is the yield stress measured at the 1% extension; $f_{p0.2}$ is the stress at the 0.2% offset; f_p is the tensile strength; ε_u is the ultimate strain. Table 4.2 shows the sizes and material properties of the prestressing tendons.

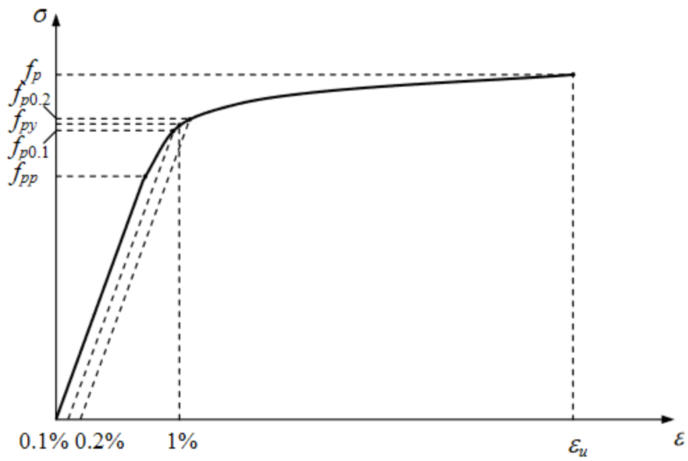

Figure 4.2 Stress-strain relationship of prestressing steel (JCSS, 2005)

Table 4.2 Tendon sizes and material properties

Tendon type	Ultimate stress f_{pu} (MPa)	Size designation	Nominal diameter (mm)	Nominal area (mm^2)	Expansion coefficient (MPa/ ˚C)	Young's modulus (MPa)	Poisson's ratio
Seven-wire strand	1860	15	15.24	140	1.0×10^{-5}	200000	0.3

To introduce prestressing in ABAQUS, the initial temperature load method was used. This method works by applying an initial temperature to the prestressing tendons. The temperature is first defined at the initial step at the tendons, then modified in the next step so the temperature change can create a force which is equal to the prestressing force.

The prestressing force was applied by specifying an equivalent change to the tendons according to Equation 4.1 (Ren et al., 2015):

$$C = -\frac{P}{c \cdot E \cdot A} \tag{4.1}$$

In which C is the applied temperature (˚C), c is the coefficient of linear expansion which is 1.0×10^{-5} (MPa/ ˚C) for steel tendons, E is the prestressing tendon elastic modulus, A is the tendon cross-sectional area in mm^2, and P is the applied force in N.

4.1.1.4 Steel tower

The steel elastic modulus and Poisson's ratio used for modelling steel tubular towers were similar to those of steel reinforcing bars; however, the yield stress f_y and the corresponding strain ε_y were considered to be 350 MPa and 0.00175, respectively. The steel stress-strain curve was also considered to be different. A bilinear elastic-plastic steel material property was adopted in order to simulate the failure in a better way, and the strain-hardening rate used here was E/65, as shown in Fig. 4.3 (Khedmati et al., 2012).

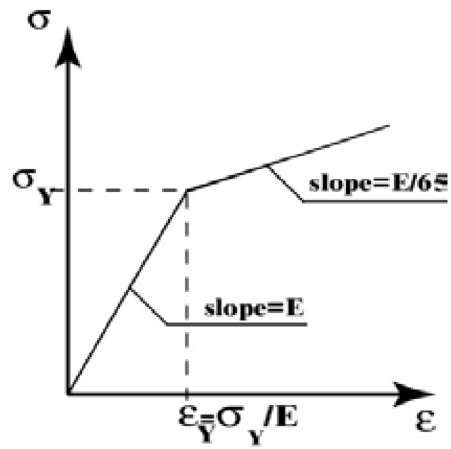

Figure 4.3 Bilinear elastic-plastic steel stress-strain relationship (Khedmati et al., 2012)

4.1.1.5 Concrete

The concrete compressive strength used for the model simulations was 47 MPa. The behaviour of concrete in the CFFT tower models was predicted to be influenced mainly by bending, so the Hognestad concrete model was adopted for the stress-strain response as discussed in Section 3.2.1.2.

4.1.2 Element types

Three different element types were used during the analysis. The concrete and FRP tube were modeled using the same elements used for the model validations presented in Section 3.2.2, which were C3D8R and S4R elements, respectively. The steel towers were also modeled using C3D8R elements. The steel reinforcing bars and prestressing tendons were modeled using 3D two-node linear truss (T3D2) elements that can simulate two-node linear displacement, as shown in Fig. 4.4.

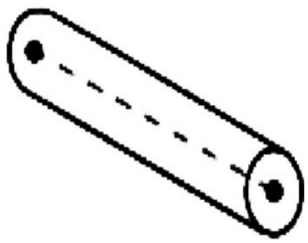

Figure 4.4 T3D2 element

4.1.3 Element interaction

The FRP tube and concrete core were connected using surface-to-surface contact, which was the same as the validation models in Section 3.2.3.

The steel reinforcing bars and prestressing tendons were connected to the concrete core using embedded region constraints. This method is used to embed a region of the model within a "host" region of the model. The host elements and the embedded elements are considered to be perfect bonded. Figure 4.5 shows the exterior tolerance for embedded elements, which means embedded nodes must lie within the distance; otherwise, an error will be caused. In this case, the steel reinforcing bars and steel tendons were selected as the embedded regions, while the concrete core was selected to be the host region. Default values were used to define the weight factor roundoff tolerance and fractional exterior tolerance; they were 1E-06 and 0.05, respectively (ABAQUS, 2016).

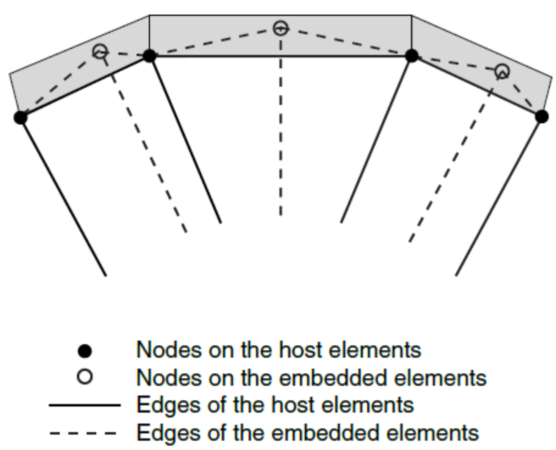

Figure 4.5 The exterior tolerance for embedded region (ABAQUS, 2016)

4.1.4 Parametric study Part A: Geometry and reinforcement

Nineteen CFFT wind turbine tower models, including one control specimen (D1), were created to test the influence of different parameters. All of the models were subjected to a horizontal concentrated load applied at the top of the tower. The parameters of interest included the tower diameter (Group 1: D2 and D3), tower height (Group 2: D4 and D5), FRP tube thickness (Group 3: D6, D7, and D8), taper ratio (Group 4: D9 and D10), steel reinforcement ratio (Group 5: D11 and D12), prestressing level (Group 6: D13 and D14), FRP fibre orientation (Group 7: D15 and D16), and concrete filling ratio (Group 8: D17, D18, and D19). Table 4.6 shows the geometric properties of the nineteen models. Table 4.4 and Table 4.5 show the FRP laminate structure of the nineteen models. Table 4.3 shows the reinforcement and prestressing details for Group 5 and Group 6.

A model with 50% concrete filling ratio was considered as the control model according to results of model D1, D17, D18, and D19, since the improvement in model performance reduced while increasing the concrete filling ratio when it is larger than 50%.

Table 4.3 Reinforcement and prestressing details of CFFT models

Model number	Group number	Steel rebar type	Area of steel (% A_c)	Tendon type	Prestressing tendons	Prestressing level (% f_{pu})
D1 to D10 D15 to D19	/	/	0	/	0	0
D11 D12	5	6#30M 6#45M	1.07 2.30	/ /	0 0	0 0
D13	6	6#45M	2.30	Seven-wire strand	6	50
D14	6	6#45M	2.30	Seven-wire strand	12	50

Table 4.4 FRP lamina structure of CFFT models

Number of FRP	1	2	3	4	5	6
FRP thickness (mm)	10	7.5	15	15	10	10
Number of layers	10	8	15	10	10	10

Table 4.5 FRP stacking sequence of CFFT models

Number of FRP	Lamina structure and stacking sequence														
	Layers														
	1	2	3	4	5	6	7	8	9	10	11	12	13	14	15
1	1	1	1	1	1	1	1	1	1	1					
	0	90	0	90	0	90	0	90	0	90					
2	1	1	1	1	1	1	1	0.5							
	0	90	0	90	0	90	0	90							
3	1	1	1	1	1	1	1	1	1	1	1	1	1	1	1
	0	90	0	90	0	90	0	90	0	90	0	90	0	90	0
4	1.5	1.5	1.5	1.5	1.5	1.5	1.5	1.5	1.5	1.5					
	0	90	0	90	0	90	0	90	0	90					
5	1	1	1.1	1	1	1.1	1	1	1.1	0.7					
	0	0	90	0	0	90	0	0	90	0					
6	1	1	1.1	1	1	1.1	1	1	1.1	0.7					
	90	90	0	90	90	0	90	90	0	90					

Table 4.6 Dimensions of CFFT models

Model number	Group number	Height (mm)	Base diameter (mm)	Top diameter (mm)	Taper (%)	Concrete fill (%D)	Concrete strength (MPa)	FRP type
D1	Control	10000	1000	1000	0	50	47	FRP1
D2	1	10000	1500	1500	0	50	47	FRP1
D3		10000	500	500	0	50	47	FRP1
D4	2	5000	1000	1000	0	50	47	FRP1
D5		15000	1000	1000	0	50	47	FRP1
D6	3	10000	1000	1000	0	50	47	FRP2
D7		10000	1000	1000	0	50	47	FRP3
D8		10000	1000	1000	0	50	47	FRP4
D9	4	10000	1000	900	1	50	47	FRP1
D10		10000	1000	800	2	50	47	FRP1
D11	5	10000	1000	1000	0	50	47	FRP1
D12		10000	1000	1000	0	50	47	FRP1
D13	6	10000	1000	1000	0	50	47	FRP1
D14		10000	1000	1000	0	50	47	FRP1
D15	7	10000	1000	1000	0	50	47	FRP5
D16		10000	1000	1000	0	50	47	FRP6
D17	8	10000	1000	1000	0	100	47	FRP1
D18		10000	1000	1000	0	75	47	FRP1
D19		10000	1000	1000	0	25	47	FRP1

4.1.5 Parametric study Part B: Loading configuration

Fifteen models were tested in this section. Table 4.9 shows the geometry of the various models. The geometric shape of model L1 to L12 was the same and was selected according to the results of model D1 to D19. Parameters providing the highest load capacities in the previous study were used in this section. Model L13, L14, and L15 were larger than other models. They were simulated to extend the range of tower heights in this study and were tested under the same loading condition as model L1. All fifteen models had the same steel reinforcement ratio and prestressing level, as shown in Table 4.7, but were examined under different load scenarios, including different load distribution conditions (L1, L2, and L3), different load eccentricity conditions (L1, L4, and L5), different axial loading conditions (L6, L7, and L8), and different combined loads (L9, L10, L11, and L12), which are shown in next section. Table 4.8 and Fig. 4.6 show the different load scenarios.

Table 4.7 Steel reinforcement and prestressing details of CFFT models

Model number	Steel rebar type	Tendon type	Prestressing tendons	Prestressing level (%f_{pu})
L1 to L15	6#45M	Seven-wire strand	6	50

Table 4.8 Different loading conditions of CFFT models

Loading condition	Horizontal load distribution	Load eccentricity (mm)	Axial load (kN)
L1	Concentrated load	0	/
L2	Uniform load	/	/
L3	Triangular load	/	/
L4	Concentrated load	200	/
L5	Concentrated load	400	/
L6	/	/	100
L7	/	/	200
L8	/	/	300
L9	Concentrated load	0	200
L10	Concentrated load	200	200
L11	Concentrated load	200	300
L12	Concentrated load	400	200
L13 to L15	Concentrated load	0	/

Table 4.9 The geometric details of CFFT models

Model number	Height (mm)	Base diameter (mm)	Top diameter (mm)	Taper (%)	Concrete fill (%D)	Concrete strength (MPa)	FRP type
L1 to L12	10000	1000	800	2	50	47	FRP6
L13	25000	1500	1000	2	50	47	FRP6
L14	20000	1500	1000	2	50	47	FRP6
L15	20000	1000	800	2	50	47	FRP6

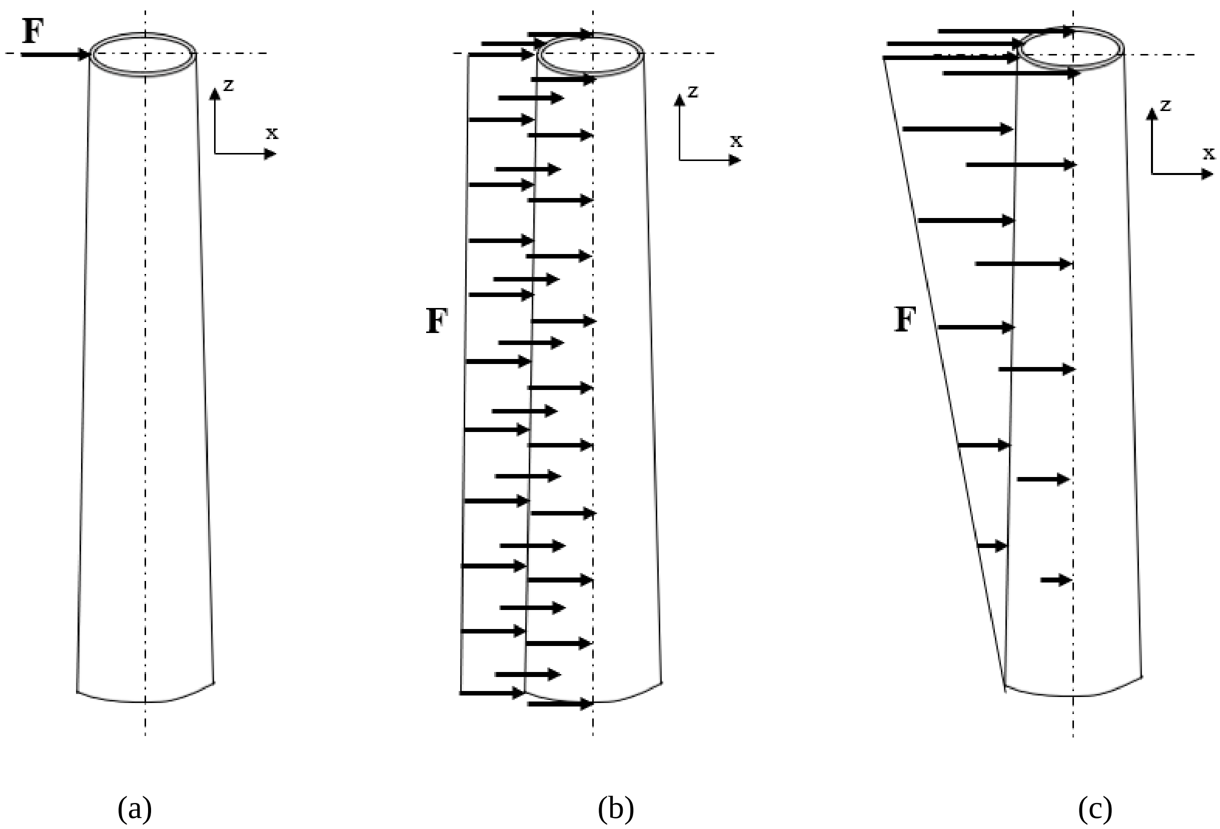

Figure 4.6 (a) Concentrated load (b) Uniform load (c) Triangular load

4.1.6 Parametric study Part C: Tower type

Two concrete wind turbine tower models (C1 and C2) with different number of prestressing tendons and three steel tubular tower models (S1, S2, and S3) with different wall thicknesses were developed, analyzed, and compared to the CFFT wind turbine tower model (L1). The concrete wind turbine tower models and the CFFT wind turbine tower model had the same steel reinforcement ratio (2.3%) and concrete filling ratio (50%). All the concrete and steel wind turbine tower models were tested under concentrated horizontal load at the top of the tower, which was the same as model L1. Table 4.10 shows the concrete and steel tubular wind turbine tower model sizes.

Table 4.10 Dimensions of concrete and steel wind turbine tower models

Model number	Tower type	Height (mm)	Base diameter (mm)	Top diameter (mm)	Taper (%)	Number of tendons	Concrete strength (MPa)	Steel wall thickness (mm)
C1	Concrete	10000	1000	800	2	6	47	/
C2	Concrete	10000	1000	800	2	12	47	/
S1	Steel	10000	1000	800	2	/	/	10
S2	Steel	10000	1000	800	2	/	/	20
S3	Steel	10000	1000	800	2	/	/	30

4.1.7 Estimated deflection limits and service loads

Deflection limits and service loads were obtained according to previous studies and guidelines mentioned in Sections 2.1.3 and 2.1.4.

The deflection limit of the wind turbine tower is 1.25% of the height, as presented in Table 4.11.

Table 4.11 Deflection limits of wind turbine tower models

Model number	Deflection limit (mm)
D1 to D3, D6 to D19, L1 to L12	125
D4	62.5
D5	187.5
L13	312.5
L14, L15	250
C1, C2	125
S1 to S3	125

The horizontal service load applied on different tower models was calculated. To obtain the service loads for different models, wind speed and wind turbine parameters are required. The average wind speed (V_{ave}) and the extreme wind speed with a 50-year recurrence time interval (V_{e50}) were obtained using wind class 2 (medium wind) defined by IEC, as shown in Table 4.12, since most remote areas in Canada had a similar wind speed. Class 2 turbines are the most common class of wind turbines available. A 5-kW small wind turbine was considered in the calculation, and the parameters are shown in Table 4.12. These values are based on a commercially available turbine that is typically mounted on a 9-m tall tower (Unplugged Power Systems 2021). For the load case D, the value of $F_{x-shaft}$ obtained was 2,713 N. The projected area of different tower models, as well as the results for load case H (Eqs. 2.2-2.4) are presented in Table 4.13.

Table 4.12 Wind speed and wind turbine sizes

V_{ave} (m/s)	8.5
V_{e50} (m/s)	59.5
A (m^3)	19.6
B	3
$A_{proj,B}$ (m^3)	0.67
$A_{proj,nacelle}$ (m^3)	0.66
R (m)	2.5

Table 4.13 Service load for load case H

Model number	$A_{proj,tower}$ (m^3)	$F_{x-shaft}$ (kN)	F_{tower} (kN)	$F_{nacelle}$ (kN)	F_{total} (kN)
D1, D6 to D8, D11 to D19	10	6.5	28.2	2.2	36.9
D2 and D5	15	6.5	42.3	2.2	51.0
D3 and D4	5	6.5	14.1	2.2	22.8
D9	9.5	6.5	26.8	2.2	35.5
D10	9	6.5	25.4	2.2	34.1
L1 to L12	9	6.5	25.4	2.2	34.1
L13	31.25	6.5	88.1	2.2	96.8
L14	25	6.5	70.5	2.2	79.2
L15	18	6.5	50.7	2.2	59.4
C1 and C2	9	6.5	25.4	2.2	34.1
S1 to S3	9	6.5	25.4	2.2	34.1

Comparing results from load case D and load case H, it is clear that load case H produces the highest horizontal load.

4.2 Finite element models

This section presents the geometric shapes, mesh size, applied load, and boundary conditions of the different models analyzed in the parametric study.

4.2.1 Parametric study Part A: Geometry and reinforcement

4.2.1.1 Models without inner confinement

Models D1 to D10 and D15 to D19 did not have steel reinforcing bars and prestressing tendons. The difference between these models includes concrete filling ratio, tube diameter, tower height, taper ratio, and fibre orientation. The finite element models of the fifteen towers were similar. Figure 4.7 (a) and (b) shows the geometric shape and boundary conditions of model D1. A [0/90] layup of FRP laminates was adopted to ensure half models can be used for the fifteen towers that were all symmetric models on which the load was applied concentrically, as shown in Fig. 4.7 (c). Symmetry was enforced along the x-z plane, by restricting translation in the y-direction as well as rotation in the x- and z-direction. The bottom surface of the tower model was fixed using reference point RP1, which means all six degrees of freedom were restricted.

Figure 4.7 (d) shows the mesh for model D1. A mesh sensitivity test was performed, the failure load, the strain at base, and the deflection at the top of the models were compared, as shown in Table 4.14. Figure 4.8 shows the load-deflection and load-strain relationships of Model D1 with different mesh sizes. The failure load, axial strain, and deflection at mid-span were calculated, and the mesh size was chosen to be 150 mm for the lower third of the model and 175 mm for the upper two-thirds of the model. In this way, computational time can be saved, while accurately capturing non-linear material behaviour in the lower portion of the tower using a finer mesh.

Table 4.14 Mesh sensitivity test for Model D1

Mesh size	Failure load (kN)	Strain	Deflection (mm)
175	301.8	0.00154	348.5
150	271.8	0.00184	343.1
100	327.1	0.00163	368.3

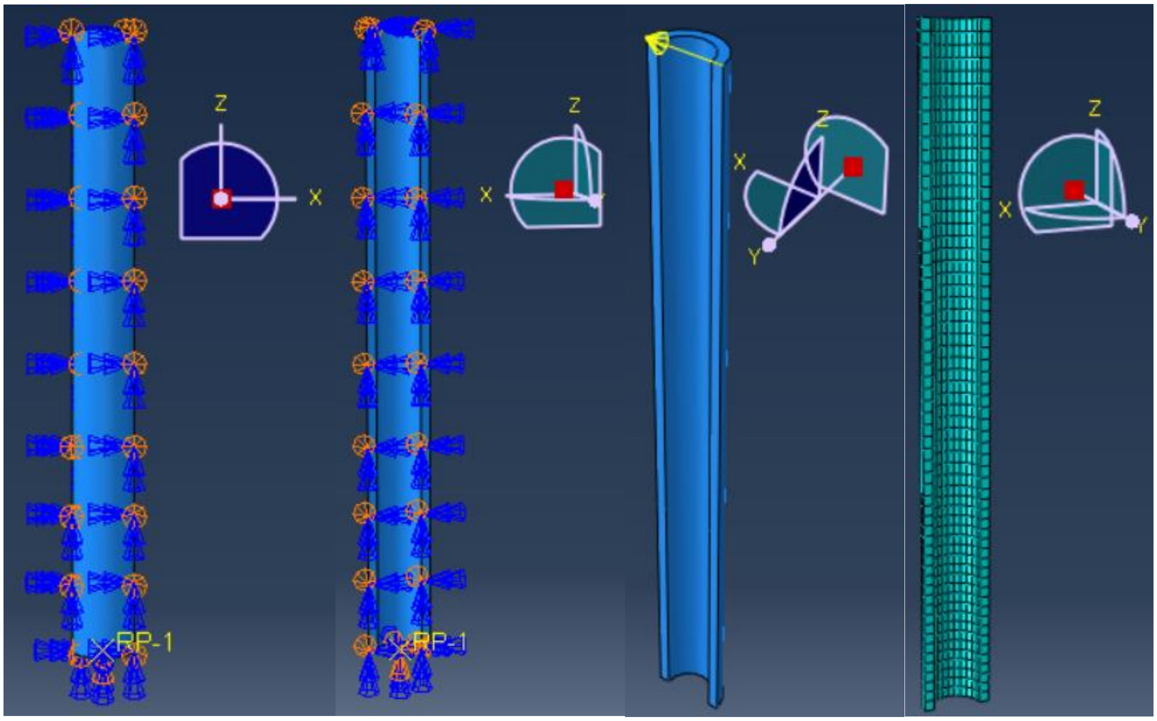

(a) (b) (c) (d)

Figure 4.7 Model D1 (a) Boundary conditions (b) Boundary conditions (c) Applied load (d) Mesh

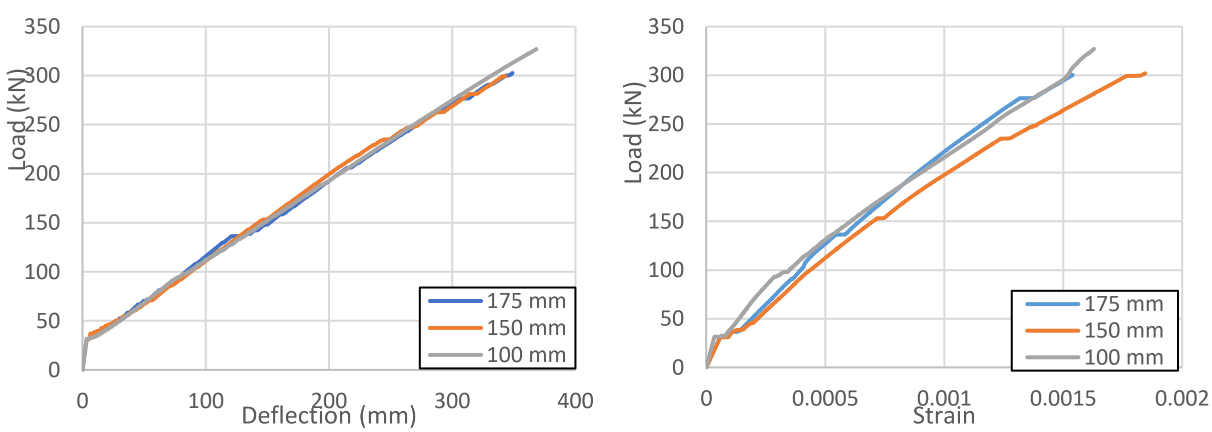

Figure 4.8 Mesh sensitivity test for Model D1 (a) Load-deflection relationship (b) Load strain relationship

The geometric shapes of model D2 to D10 and D15 to D19 were similar to model D1, and the boundary conditions and mesh sizes were the same as model D1. Model D11 to D14 also included steel reinforcement and prestressing tendons, which are further described in the following sections.

4.2.1.2 Models with steel reinforcing bars

Six steel reinforcing bars were added to model D11 and D12 to simulate steel reinforced towers with 1.07% and 2.30% reinforcement ratio. The mesh size of the FRP tubes and concrete cores of the two models were the same as model D1; the mesh size of steel reinforcement was the same as the FRP tubes and concrete cores. Figure 4.9 shows the cross-section of model D11 and D12 with steel reinforcing bars. The boundary conditions and load on model D11 and D12 were the same as model D1. Figure 4.10 presents the geometric shape and mesh for model D12. The green part is the FRP tube, the grey part is the concrete core, and the red part is the steel reinforcing bars.

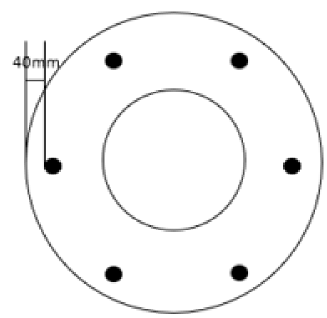

Figure 4.9 Steel reinforced tower cross-section (D11 and D12)

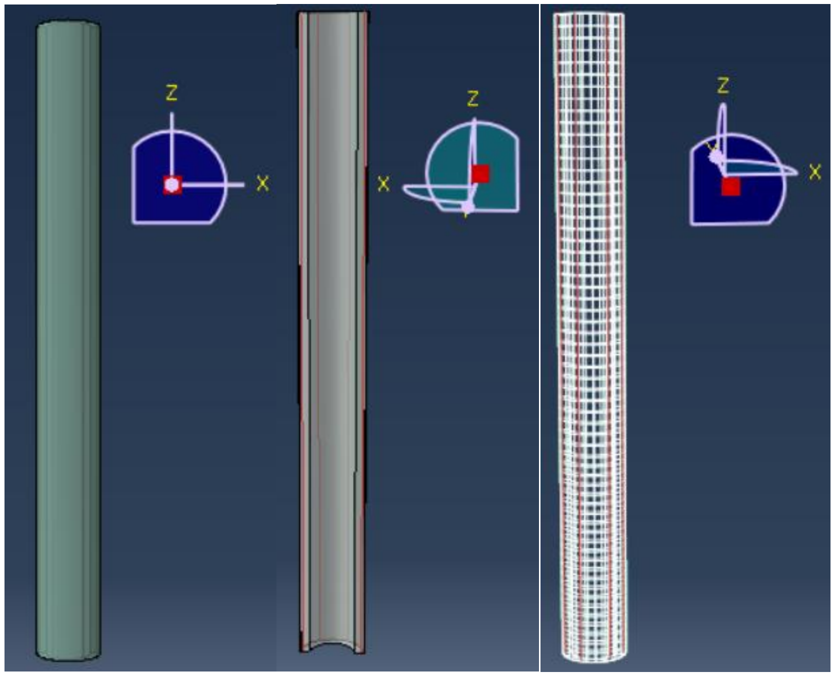

(a) (b) (c)

Figure 4.10 Model D12 (a) FRP tube (b) Concrete core (c) Mesh

4.2.1.3 Models with steel reinforcing bars and prestressing tendons

Six and twelve prestressing tendons were added to the 2.30% steel reinforced model to simulate the behaviour of prestressed tower models D13 and D14, respectively. The mesh size of models D13 and D14 was the same as model D1; the mesh size of steel reinforcing bars and prestressing tendons was 150 and 175 at lower third and upper two-thirds of the models, respectively. Figure 4.11 (a) and (b) show the cross-section of the two prestressed CFFT models containing both steel reinforcing bars and prestressed tendons. Boundary conditions and loads on the prestressed models were the same as model D1. Figure 4.12 presents the geometric shape and mesh for model D13. The green part is the FRP tube, the grey part is the concrete core, the red part is steel reinforcing bars, and the blue part is the prestressing tendons.

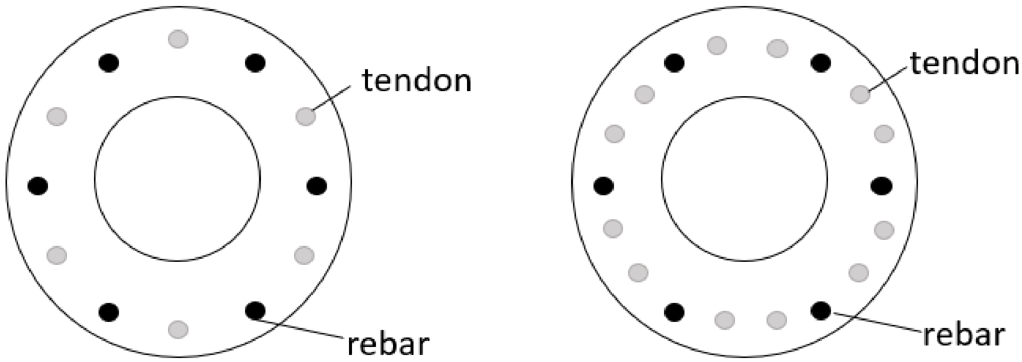

(a) (b)

Figure 4.11 Cross-section of model (a) D13 (b) D14

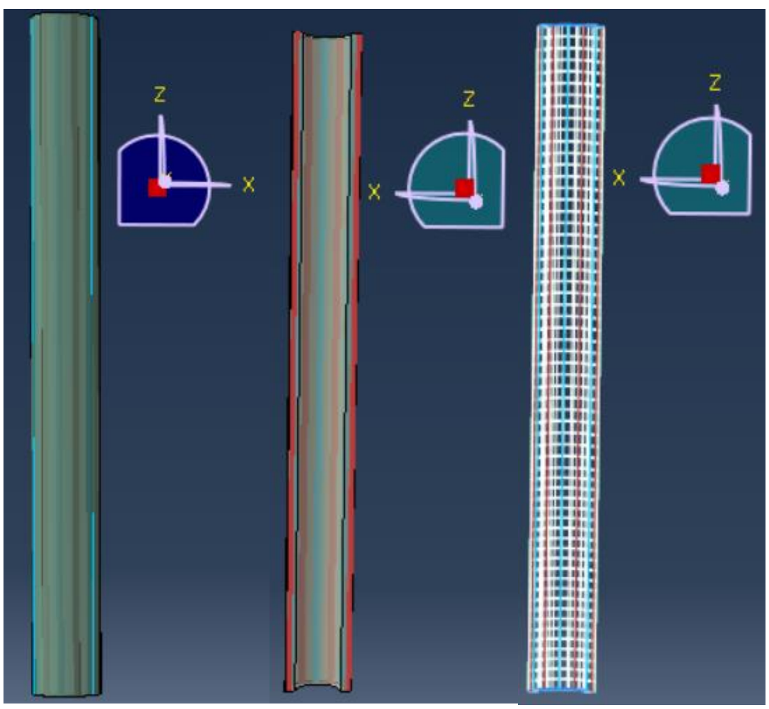

(a) (b) (c)

Figure 4.12 Model D13 (a) FRP tube (b) Concrete core (c) Mesh

4.2.2 Parametric study Part B: Loading configuration

Model L1 to L12 have the same geometric shape and reinforcement as shown in Section 4.1.4. However, the applied load is different on these twelve models.

Figure 4.11 (a) and (b) shows the geometric shape of model L1, which was the control specimen for models under different load scenarios. The model was tested under different loading conditions, which means in some conditions the applied loads were not symmetric; therefore, the entire 3D tower was modelled rather than a symmetric half tower.

The mesh sizes of model L1 to L12 were also the same. Figure 4.11 (c) shows the mesh for model L1. The model height and base diameter were the same as model D13, so the mesh size was also the same as D13: 150 mm for the lower third of the model, 175 mm for the upper two-thirds of the model.

Figure 4.13 (d) shows the boundary conditions and loading of model L1. The base of the model was fixed, so all six degrees of freedom were restricted at the bottom surface, and the load was a concentrated concentric load and was applied at the top of the tower model.

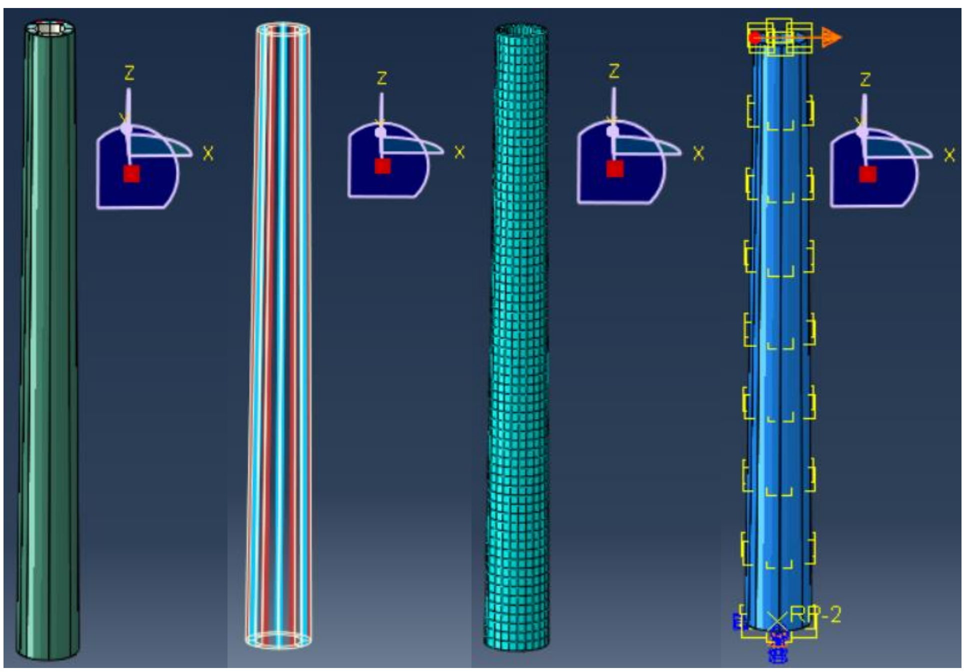

(a) (b) (c) (d)

Figure 4.13 Model L1 (a) Geometric shape (b) Geometric shape (c) Mesh (d) Boundary conditions

Figure 4.14 presents the load applied on model L2 and L3. They were compared to model L1 that was tested under concentrated load at the top of the model along x-direction, as shown in Fig. 4.11 (d).; Model L2 was tested under uniform load distribution along x-direction; model L3 was tested under triangular distributed load along x-direction, and maximum and minimum loads were applied at the top and base of the model, respectively. Figure 4.15 presents the tower models L1, L4, and L5 that examined different load eccentricities. Concentrated concentric and eccentric loads were applied at the top of the tower models. Models L6, L7, and L8 were tested under different axial loads, as shown in Fig. 4.16.

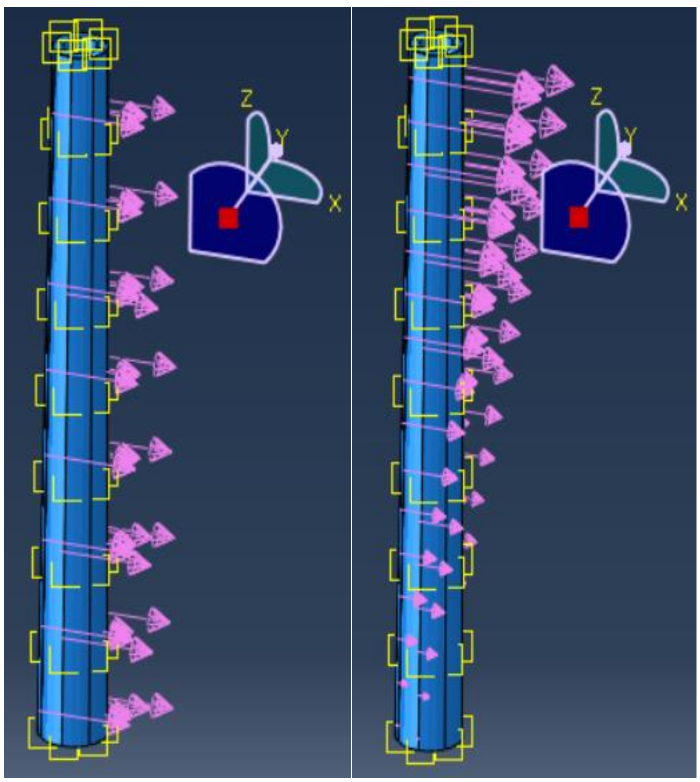

(a) (b)

Figure 4.14 Different load distribution on model (a) L2 (b) L3

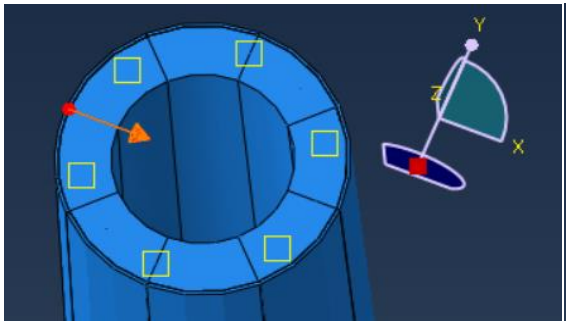

(a)

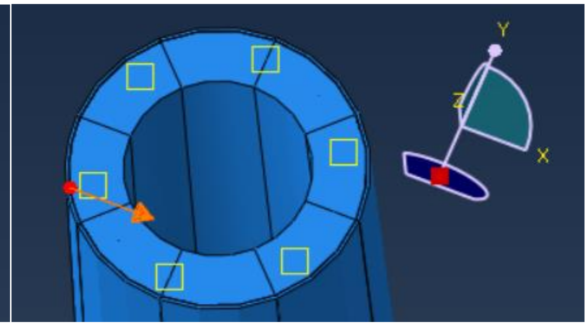

(b)

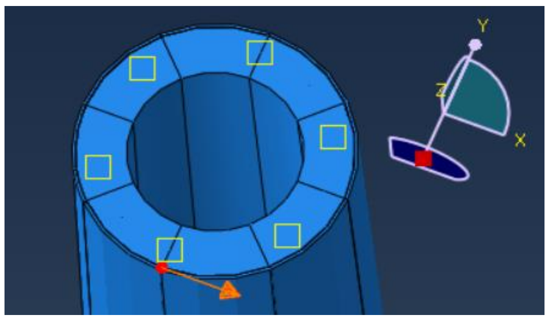

(c)

Figure 4.15 Different load eccentricities on model (a) L1 (b) L4 (c) L5

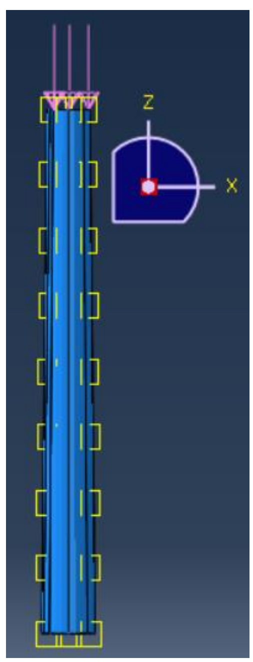

Figure 4.16 Axial load applied on models L6, L7, and L8

Figure 4.17 presents the combined load conditions of model L9 to L12. The axial load was first applied on the models, and then the horizontal load with different eccentricities was applied at the top of the tower models after the specified axial load was reached. The difference in axial loads and lateral load eccentricities were shown in Section 4.1.4.

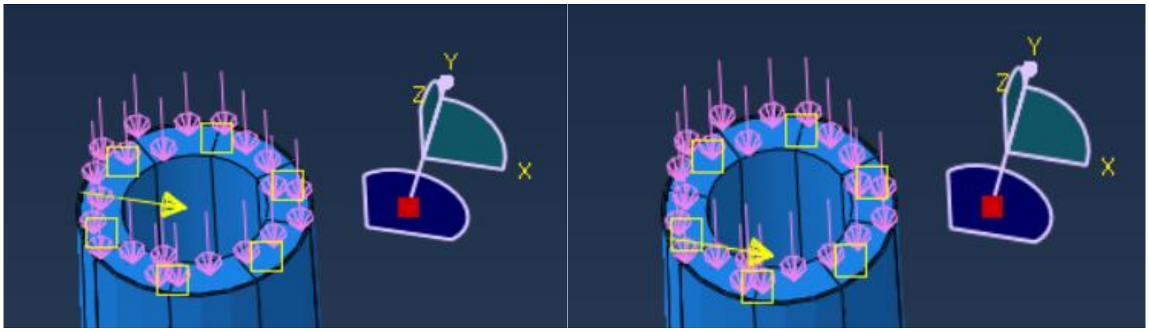

(a) (b)

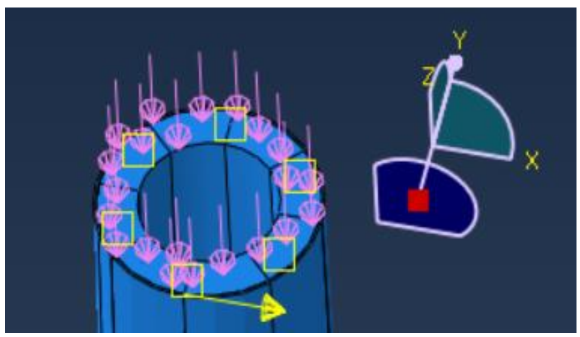

(c)

Figure 4.17 Different combined load on models (a) L9 (b) L10 and L11 (c) L12

Model L13, L14, and L15 were larger than the other models. They were tested under concentrated lateral load to compare to model L1 to further investigate the influence of tower height and base diameter. Figure 4.18 (a), (b), and (c) show the geometric shape and mesh for model L13. A mesh sensitivity test was done to obtain the mesh sizes, which were 150 mm at the lower one-fifth and 250 at the upper four-fifths. Model 13 was a symmetric model conducted under concentrated load, so it was developed as a half model. The boundary conditions and applied load are shown in Fig. 4.18 (d). The translation in the y-direction was restricted, as well as rotation in the x- and z-direction to simulate a model symmetrical with respect to the x-z plane. Model L14 and L15 had the same mesh size and boundary conditions as model L13.

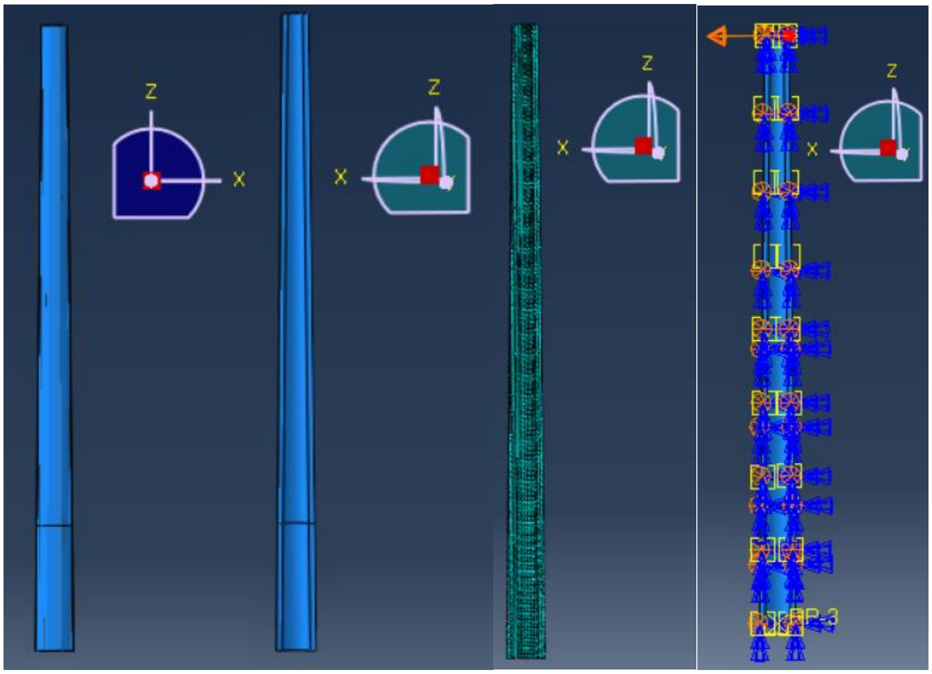

(a) (b) (c) (d)

Figure 4.18 Model L13 (a) Geometric shape (b) Geometric shape (c) Mesh (d) Boundary conditions

4.2.3 Parametric study Part C: Tower type

4.2.3.1 Concrete tower models

Concrete tower models were developed as control models for CFFT tower models; therefore, the geometric shape of models C1 and C2 were the same as the model L1. The differences between concrete models and CFFT models are the FRP outer tube and prestressing level, since model C1 had the same prestressing level as model L1, but model C2 had higher prestressing level than model L1, as mentioned in Section 4.1.4. The boundary conditions, mesh and loading were also the same as model L1.

4.2.3.2 Steel tubular tower models

Models S1, S2, and S3 had the same restrictions, loading conditions, and mesh size. Figure 4.19 (a) shows the boundary conditions and loading applied on model S2. It was a symmetric steel tower model and was constrained in the same way as the concrete tower model. The mesh for model S2 is presented in Fig. 4.19 (b). To minimize the error, the mesh size of the steel tower model was the same as concrete tower models and CFFT tower models.

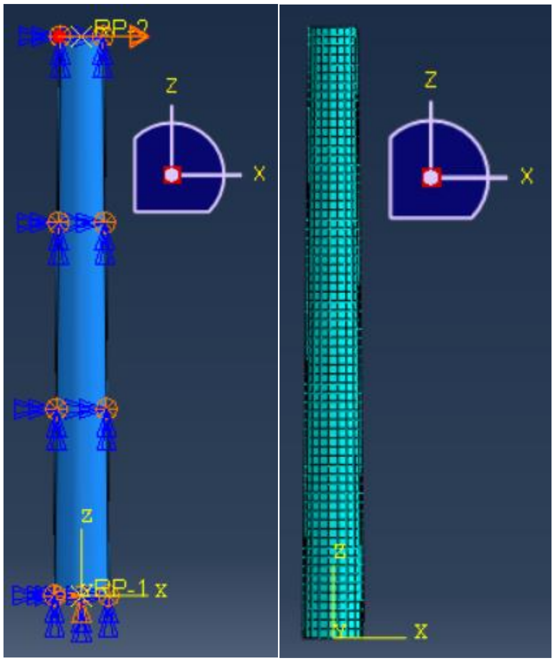

(a) (b)

Figure 4.19 Model S2 (a) Boundary conditions and loading conditions (b) Mesh

Steel tubular towers are thin-walled steel structures with the maximum wall thickness of 30 mm, so local buckling tests were conducted to avoid buckling failure. However, buckling results may be affected by the use of half models, so three full steel tower models were developed to capture the accurate buckling behaviour, as shown in Fig. 4.20 (a). The full models were fixed at the base of the tower, which were the same as CFFT full models, and the mesh sensitivity tests were done to obtain accurate results. The approximate mesh sizes of the three full steel models were all 30 mm, as shown in Fig. 4.20 (b).

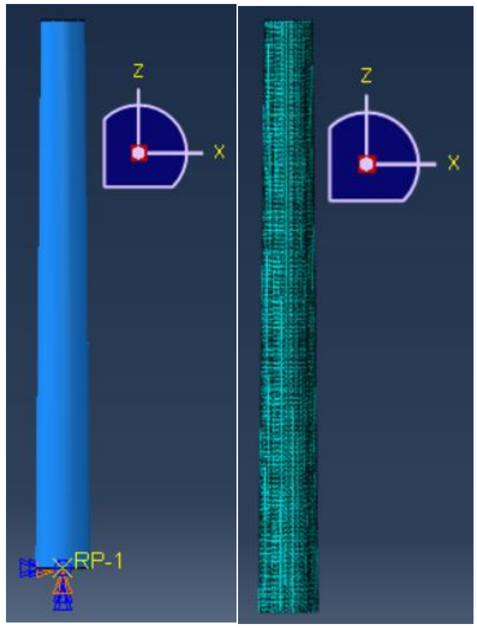

(a) (b)

Figure 4.20 20 mm wall thickness full steel tubular tower model (a) Geometric shape and boundary conditions (b) Mesh

4.3 Results

The results of models tested using different parameters were compared to each other to find out the most effective way to design the small-scale CFFT wind turbine tower. The selected tower model was then used to test the effect of different load scenarios. The concrete and steel tubular tower models were then built and tested to compare to the CFFT tower model. The weights of towers made of different materials were compared as well.

4.3.1 Results for Parametric study Part A: Geometry and reinforcement

The load-deflection curve of each model was obtained and compared to the control specimen model D1 to find out the influence of different parameters on the tower behaviour. The maximum load, displacement at the top of the tower model at failure, failure mode, deflection at service load, and the applied load at the deflection limit are discussed in this section.

Figure 4.21 shows the load-deflection curves of models from Group 1 to Group 8. Overall, a bilinear load-deflection response was obtained for CFFT tower models without inner reinforcement. With the increase of steel reinforcement ratio and prestressing ratio, the results became more non-linear, but the change in other geometric parameters only influence the slope of the load-deflection curves and thus influence the final results. The figures indicate that increasing the diameter, FRP tube thickness, steel reinforcement ratio, and prestressing ratio improve the performance of CFFT wind turbine tower models; the decrease of height and proportion of fibres in the hoop direction improve the performance of CFFT wind turbine towers; the taper ratio does not affect the load capacity but does have an effect on the deflection of the CFFT wind turbine towers. The influence of concrete filling ratio varies and seems to be significant below a certain threshold. Details are discussed below.

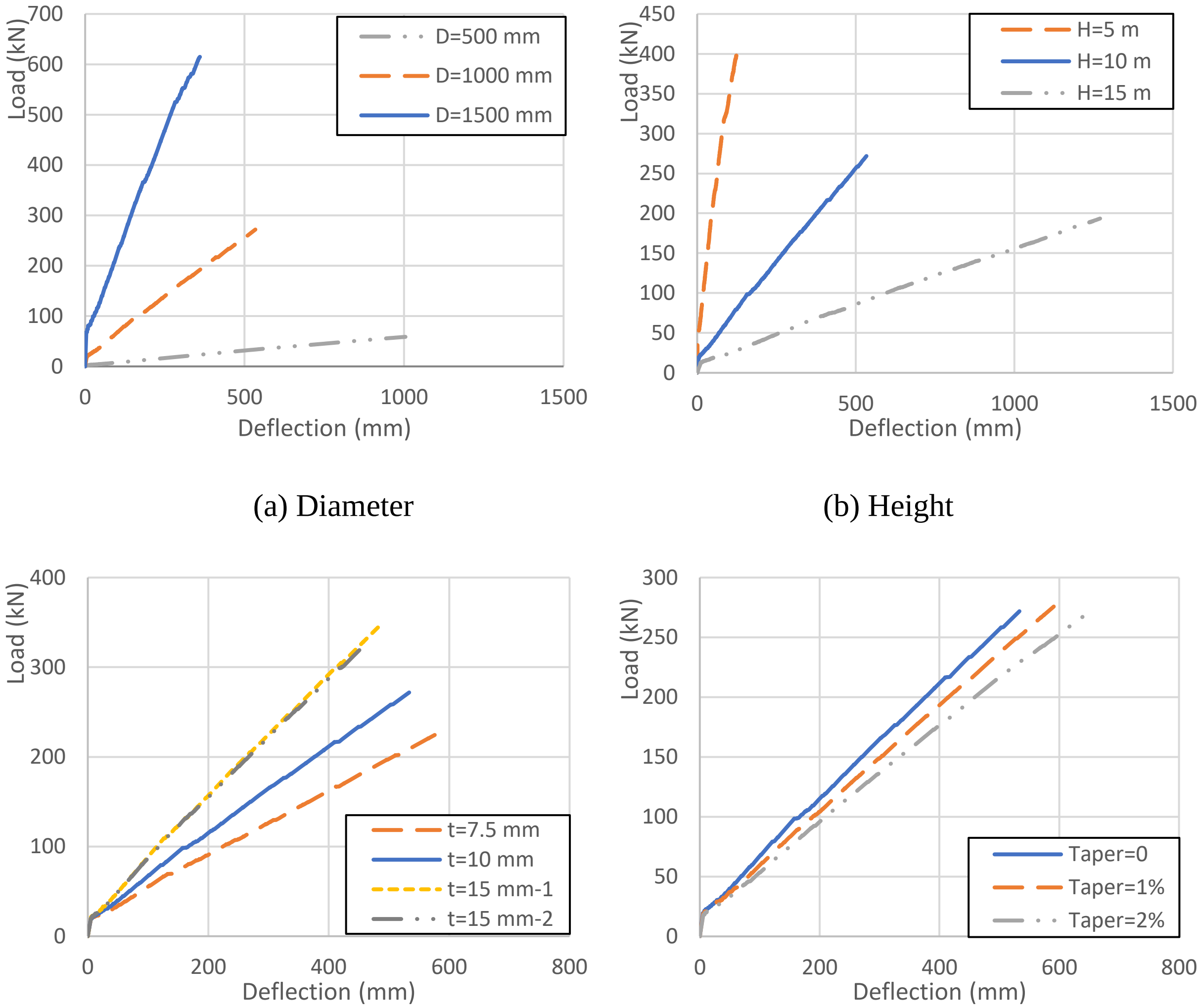

(a) Diameter

(b) Height

(c) FRP tube thickness

(d) Taper ratio

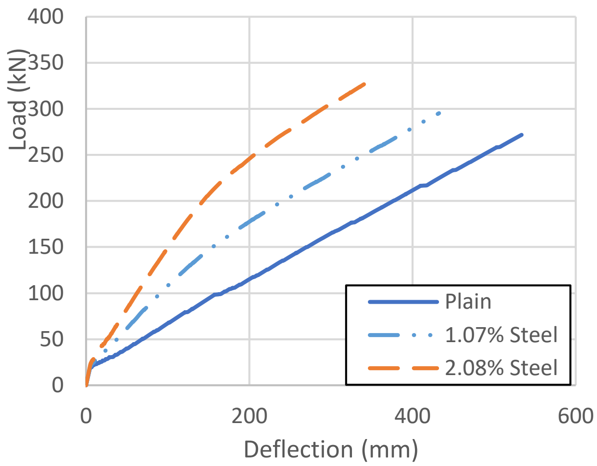

(e) Steel reinforcement ratio

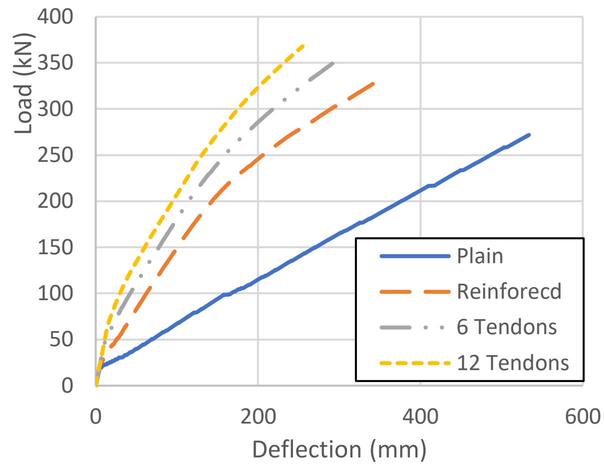

(f) Prestressing ratio

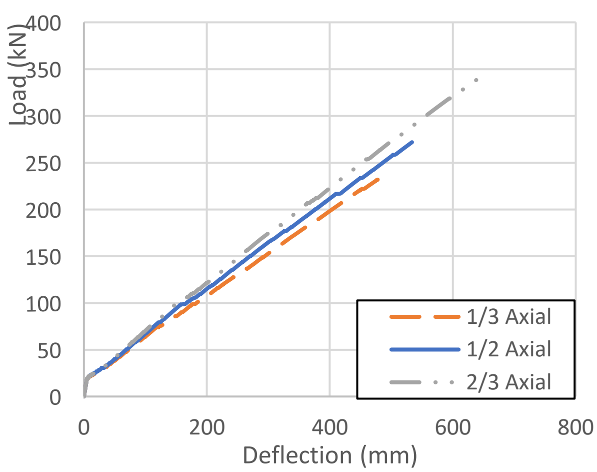

(g) Fibre orientation

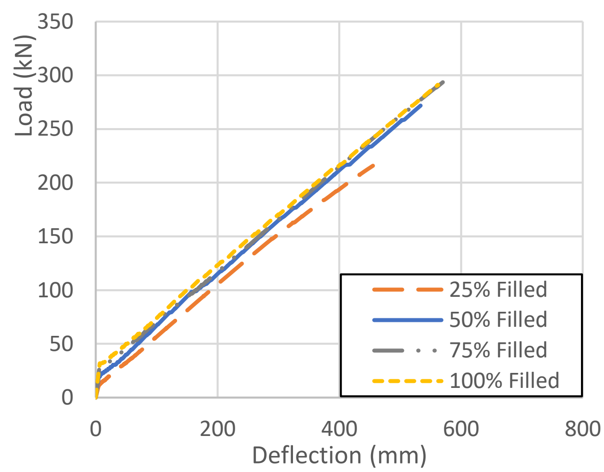

(h) Concrete filling ratio

Figure 4.21 Load-deflection relationship of models with different (a) Diameter (b) Height (c) FRP tube thickness (d) Taper ratio (e) Steel reinforcement ratio (f) Prestressing ratio (g) Fibre orientation (h) Concrete filling ratio

Figure 4.22 shows the FRP tube longitudinal strain distribution of models D1, D12, and D13 at failure. The region of high strains of the three unreinforced, steel reinforced, and prestressed models was at the tension side of all models near the base of the tower. The maximum tensile strain of model D1 is 69.4% larger than model D12 and 71.3% larger than model D13. The internal steel reinforcement is the main cause of the difference. Figure 4.23 shows the strain distribution of the same models at the deflection limit (1.25% of tower height). The maximum tensile strain of model D1 is 46.8% and 38.5% higher than model D12 and model D13, respectively, which is similar to the tensile strain at failure. It is clear that the maximum strain at the deflection limit is about 67% lower than the maximum strain at failure, while the load decreased 70.6%, 46.0%, and 39.4% for models D1, D12, and D13, respectively. At service load, the deflection decreased 92.7%, 96.4%, and 97.3% for models D1, D12, and D13. Figure 4.24 (c) - (f) presents the displacement in the z-direction at the deflection limit for models D1, D10, D12, and D13. Control model D1 and tapered model D10 had smaller z-direction displacement at the base of the tower models in the tension side, while two reinforced or prestressed models had positive displacements. The possible reason for the difference is the steel reinforcement in models D12 and D13 that enhanced the concrete core. The maximum z-direction deflection in model D1 was obtained at the centroid of the top cross-section, which means it is the average deflection, and is 8.0%, 15.3%, and 24.9% larger than models D10, D12, and D13, respectively, which indicates that the increase of taper ratio, steel reinforcement, and prestressing ratio all decrease the deflection in the z-direction. The reasons include the decrease of the cross-section area and the reinforcement of steel bars and tendons. The deflection in x-direction was similar for all the CFFT tower models, and the displacement of model D1 at the deflection limit and failure is shown in Fig. 4.24 (a) and (b). Figure 4.25 and Fig. 4.26 present the axial stress contour for steel reinforcing bars and prestressing tendons of models D12 and D13 at failure and deflection limit, respectively. At failure, two steel reinforcing bars at the tension side yielded, and one bar at the compression side also had tensile stress for both models, but at the deflection limit, only one steel reinforcing bar at the tension side yielded for both models. The prestressing tendon in model D13 placed in the tension side yielded at failure, but it did not reach the yield stress at the deflection limit.

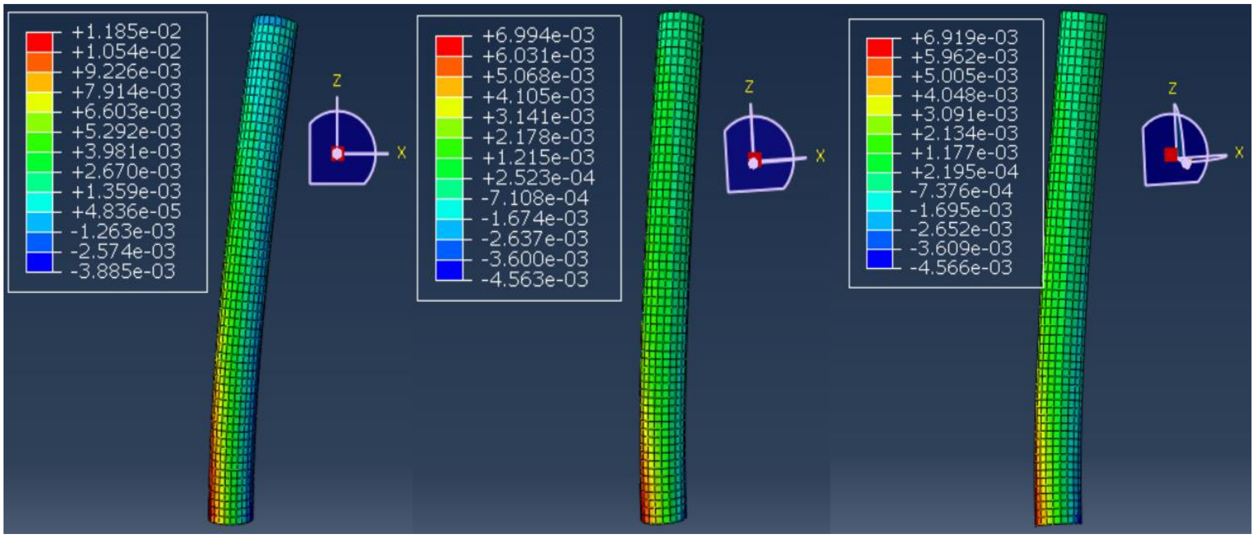

(a) (b) (c)

Figure 4.22 Strain distribution at failure for (a) Model D1 (b) Model D12 (c) Model D13

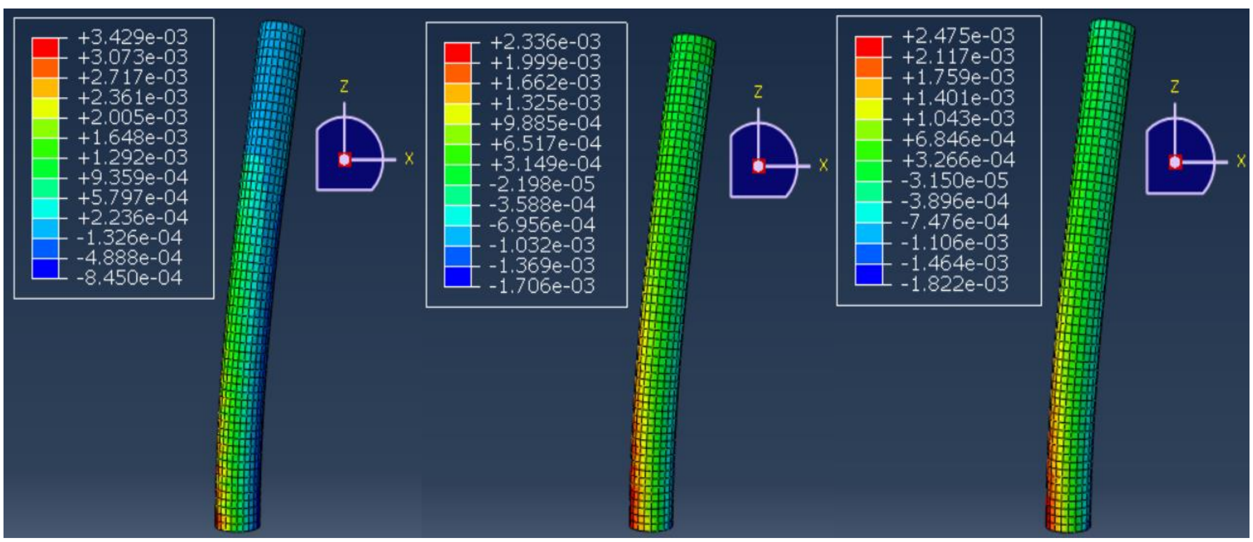

(a) (b) (c)

Figure 4.23 Strain distribution at deflection limit for (a) Model D1 (b) Model D12 (c) Model D13

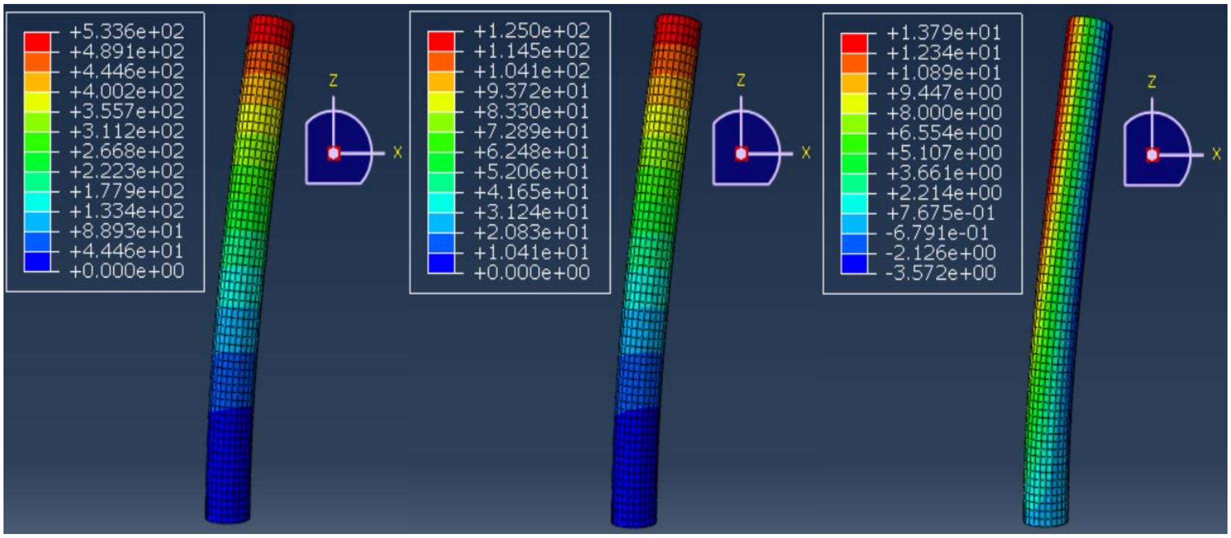

(a) (b) (c)

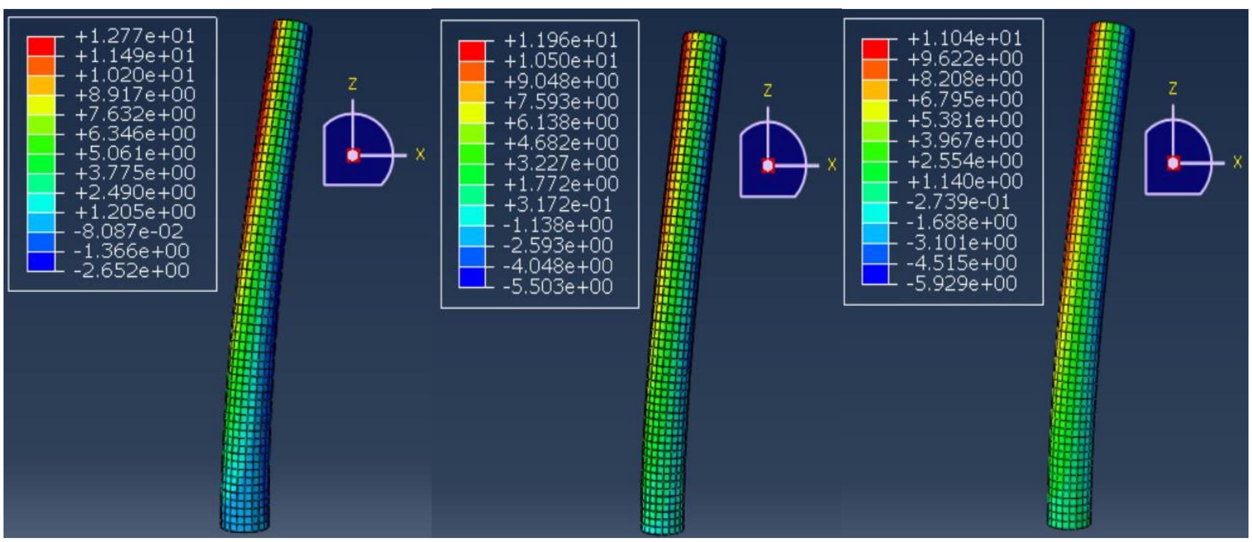

(d) (e) (f)

Figure 4.24 Displacement (mm) of (a) Model D1 in x-direction at failure (b) Model D1 in x-direction at deflection limit (c) Model D1 in z-direction (d) Model D10 in z-direction (e) Model D12 in z-direction (f) Model D13 in z-direction

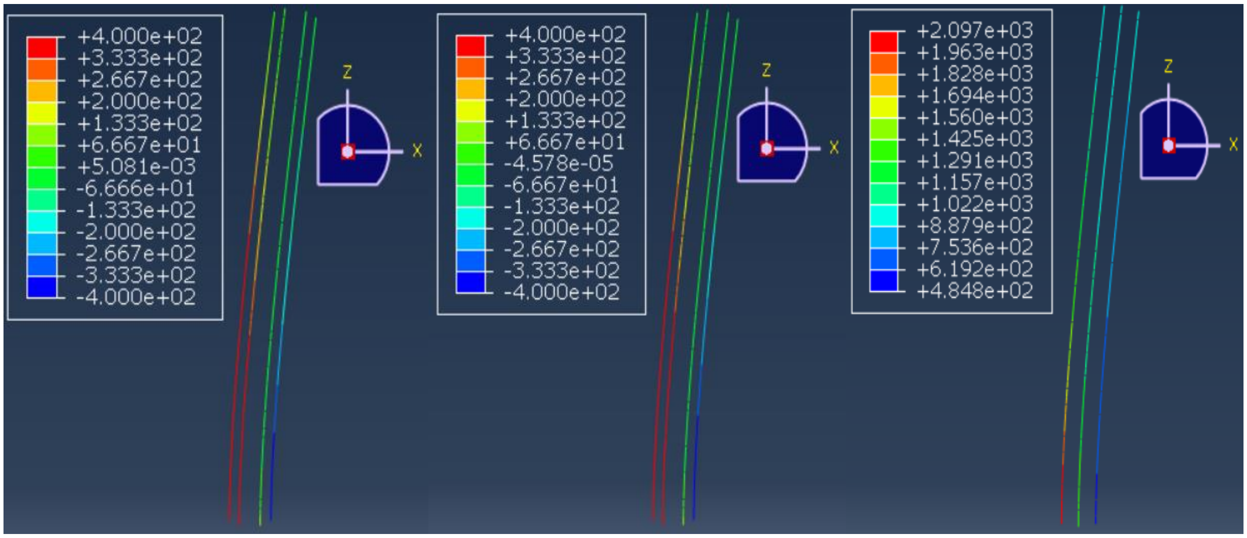

(a) (b) (c)

Figure 4.25 Contour plot of axial stress (MPa) at failure for (a) Steel reinforcing bars of model D12 (b) Steel reinforcing bars of model D13 (c) Prestressing tendons of model D13

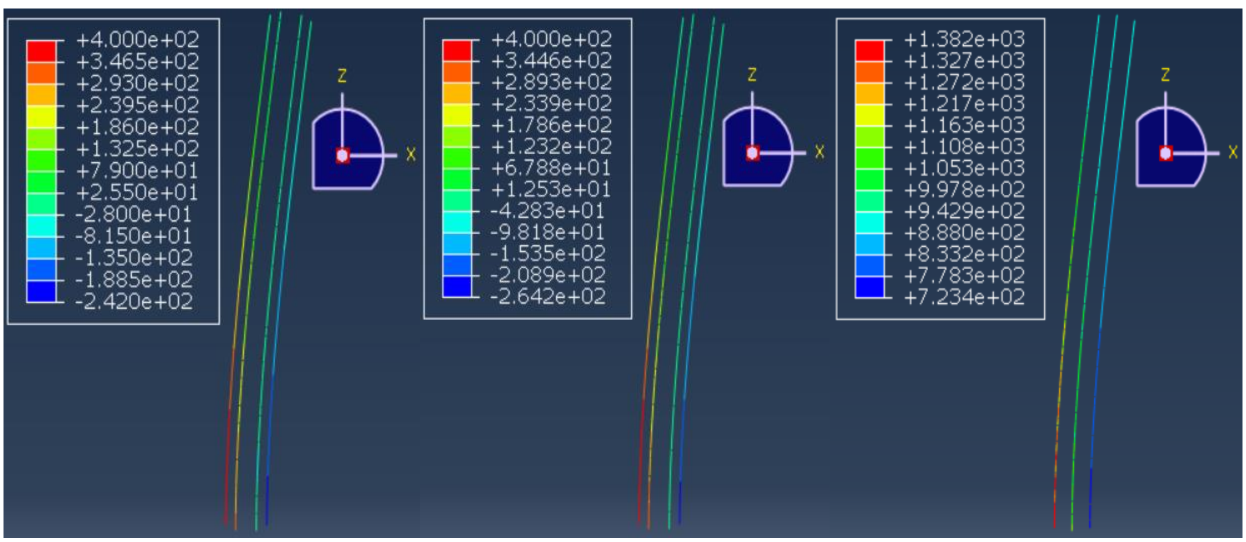

(a) (b) (c)

Figure 4.26 Contour plot of axial stress (MPa) at deflection limit for (a) Steel reinforcing bars of model D12 (b) Steel reinforcing bars of model D13 (c) Prestressing tendons of model D13

Table 4.15 shows the failure mode and maximum load (F_{max}) and deflection (D_{max}) of model D1 to D19. The results were compared to the control specimen D1. All the nineteen models failed due to FRP rupture at the tension side near the base of the tower model. Increasing the tower model diameter increased the load capacity and stiffness significantly. A 50% increase in diameter resulted in 126.2% increase in load capacity and 32.6% decrease in maximum deflection. It is noted that the change in model height had a lower influence on maximum load and a higher influence on maximum deflection. The load decreased 28.8% and the deflection increased 138% when the height increased 50%. The height of model D4 is 50% lower than model D1, but the load capacity and deflection are 50% higher and 75.7% lower than model D1, which means the effect of tower height is still significant.

Comparing models from Group 3 to the control model, it is clear that the increase in the FRP tube thickness improved the behaviour of CFFTs. A 25% decrease in FRP tube thickness leads to a 17.4% decrease in load capacity and 8% increase in deflection. Two 15 mm FRP tube CFFT models were tested, model D7 had 15 layers of FRP, and model D8 had 10 layers. The maximum load of model D8 was 9.9% higher than model D7, while the deflection was 10.2% larger than model D7. The possible reason for the increased deflection is the higher ultimate load, which means FRP tubes made of thicker FRP laminates have better load capacity, but the stiffness did not change a lot due to FRP laminate thickness.

Results of Group 4 indicate that the taper ratio does not have a significant influence on load capacity, since the load only increased 1.4% and 0.4% with a 1% and 2% taper ratio, respectively. However, the deflection increases with the taper ratio. When the taper ratio is 1% and 2%, the maximum deflection increased 10.7% and 22.9%, respectively.

The influence of steel reinforcement is also considered in this section. Compared to the unreinforced CFFT model, the steel reinforced CFFT tower model D11 with 1.07% reinforcement ratio had an 8.6% increase in load capacity and 18.9% decrease in ultimate deflection. Model D12 with 2.30% reinforcement ratio had better load capacity and stiffness as shown in Table 4.9. Comparing the two reinforced models, model D12 had 13.4% higher load capacity and 17.6% lower deflection than model D11, which means the increase in steel reinforcement ratio affected the behaviour of CFFT models.

Two prestressed models are compared to the control model D1 and steel reinforced model D12. It is noted that compared to the unreinforced model, the load capacity increased 29.9% and 35.3% for models D13 and D14, respectively. Meanwhile, compared to the steel reinforced model, the load capacity increased 5.3% and 9.7%, and deflection decreased 16.4% and 28.5% for models D13 and D14. The effect of prestressing is larger on deflection at failure.

The influence of fibre orientation was examined by applying one-third of FRP laminates in the hoop or axial direction and other two-thirds of FRP laminates in the perpendicular orientation. The decrease of proportions of fibres in the hoop direction improves the performance of CFFT models in flexure, as shown in Table 4.15. The CFFT model with two-thirds of fibres in the axial direction had 27.4% higher load capacity and 23.3% higher deflection than CFFT models with only one-half of fibres in the axial direction.

The concrete filling ratio hardly had any influence on the behaviour of the CFFT towers when it was larger than 75%, since the load capacity and deflection only increased 3.1% and 3.9% when the concrete filling ratio increased from 75% to 100%; when it was larger than 50%, the increase of concrete filling ratio only slightly improves the model behaviour, with a 7.1% increase in load and 5.4% increase in deflection as the filling ratio increased 25%. However, when it is smaller than 50%, the improvement of behaviour becomes obvious with the increase of concrete filling ratio. A 25% decrease resulted in a 20.6% and 14.7% decrease in load capacity and deflection, respectively.

Table 4.15 Load and deflection results at failure

Model number	Group	F_{max} (kN)	Compared to D1	D_{max} (mm)	Compared to D1	Failure mode
D1	Control	271.8	/	533.6	/	FRP rupture
D2	1	614.8	126.2%	359.8	-32.6%	FRP rupture
D3		58.7	-78.4%	1004.3	88.2%	FRP rupture
D4	2	407.6	50.0%	129.4	-75.7%	FRP rupture
D5		193.5	-28.8%	1270.2	138.0%	FRP rupture
D6	3	224.4	-17.4%	576.1	8.0%	FRP rupture
D7		319.0	17.4%	450.9	-15.5%	FRP rupture
D8		354.3	30.4%	497.1	-6.8%	FRP rupture
D9	4	275.7	1.4%	590.9	10.7%	FRP rupture
D10		273.0	0.4%	655.8	22.9%	FRP rupture
D11	5	295.3	8.6%	432.5	-18.9%	FRP rupture
D12		335.4	23.4%	356.4	-33.2%	FRP rupture
D13	6	353.2	29.9%	297.9	-44.2%	FRP rupture
D14		367.8	35.3%	254.8	-52.2%	FRP rupture
D15	7	239.9	-11.7%	495.0	-7.2%	FRP rupture
D16		346.2	27.4%	657.7	23.3%	FRP rupture
D17	8	291.1	7.1%	562.4	5.4%	FRP rupture
D18		300.2	10.4%	584.6	9.6%	FRP rupture
D19		215.8	-20.6%	455.3	-14.7%	FRP rupture

The load at deflection limits (F_{lim}) and deflection at service load (D_{ser}) are presented and compared to control specimen D1 in Table 4.16. In most cases, the service loads were lower than loads at deflection limits and the deflection limits were larger than the displacement at service load. The only exceptions were models D3 and D5, which are a 500-mm base diameter model and a 15-m tall model, where the load corresponding to the deflection limit was 60.5% and 25.7% lower than the service load, respectively, and the displacement at service load was 179.0% and 41.5% larger than the deflection limit, respectively. The results indicate that a 10-m model with 500-mm diameter or a 15-m model with 1000-mm diameter without any steel reinforcement does not meet serviceability criteria for a wind turbine tower. For model D1, the load at the deflection limit was 70.6% lower than the maximum load and 116.3% higher than the service load. The deflection at the service load was 91.6% and 43.6% lower than the deflection at maximum load and deflection limit, respectively. A 50% increase in diameter increased 233.5% of F_{lim}, and decreased 94.0% of D_{ser}; yet height had an opposite effect on the CFFT tower behaviour, as a 50%

decrease in model height increased the load at the deflection limit and decreased the displacement at service load 208.3% and 98.2%, respectively.

The influence of FRP tube thickness was not as significant as diameter and height. When the thickness increased 50%, the increase and decrease in F_{lim} and D_{ser} were only about 35% and 26%. The effect of taper ratio on maximum load was negligible, as shown in Table 4.15, but it had a considerable influence on the load corresponding to the deflection limit, as the load restriction decreased 10.4% and 19.2% for the 1% and 2% tapered models, respectively. A slight stiffness reduction was observed for the tapered models, as the displacement at the service load increased 0.6 mm and 4.1 mm for models D9 and D10, respectively.

Steel reinforcement and prestressing both improved CFFT model behaviour at the deflection limit and service load. A model with 2.3% steel reinforcement ratio had a 127.1% higher F_{lim} and a 67.8% lower D_{ser} than the unreinforced model D1. The application of prestressing further increased the stiffness of the CFFT towers. Compared to the steel reinforced model, the prestressed model with the same steel reinforcement ratio had a 18.1% increase in load at the deflection limit and 42.8% decrease in service load deflection. When the prestressing level increased 50%, the load and deflection also increased and decreased 13.6% and 3.8%, respectively.

The effect of fibre orientation on the CFFT tower behaviour at service is relatively small. Model D15, with one-third fibres aligned in the axial direction, only had 5.0% lower load than model D1, with one-half fibres aligned in the axial direction, when the deflection reaches the limit. For model D16 that had two-thirds fibres aligned in the axial direction, the load increased 5.6%. The deflection at service load for model D1 was 3.8% lower than model D15 and 5.6% higher than model D16.

The effect of concrete filling ratio on deflection at service load is more significant than its effect on maximum deflection. A 25% filled model had 33.1% larger deflection at service load than a 50% filled model, and the decrease is up to 50.9% in a fully-filled CFFT model. However, the load at the deflection limit only decreased 13.3% and increased 3.0% for a 25% or 75% filled model, respectively, compared to 50% filled model, which is smaller than the influence on maximum load.

Table 4.16 Load and deflection results at deflection limit and service load

Model number	Group	Deflection limit (mm)	F_{lim} (kN)	Compared to D1	Service load (kN)	D_{ser} (mm)	Compared to D1
D1	Control	125	79.8	/	36.9	45.0	/
D2	1	125	266.1	233.5%	51.0	2.7	-94.0%
D3		125	9.0	-88.7%	22.8	348.7	674.9%
D4	2	62.5	246.0	208.3%	22.8	0.8	-98.2%
D5		187.5	37.9	-52.5%	51.0	265.3	489.6%
D6	3	125	66.3	-16.9%	36.9	57.7	28.2%
D7		125	106.0	32.8%	36.9	33.4	-25.8%
D8		125	108.1	35.5%	36.9	33.4	-25.8%
D9	4	125	71.5	-10.4%	35.5	46.8	4.0%
D10		125	64.5	-19.2%	34.1	52.6	16.9%
D11	5	125	128.6	61.2%	36.9	23.2	-48.4%
D12		125	181.2	127.1%	36.9	14.5	-67.8%
D13	6	125	214.0	168.2%	36.9	8.3	-81.6%
D14		125	243.0	204.5%	36.9	8.0	-82.2%
D15	7	125	75.8	-5.0%	36.9	46.7	3.8%
D16		125	84.3	5.6%	36.9	42.5	-5.6%
D17	8	125	87.3	9.4%	36.9	22.1	-50.9%
D18		125	83.8	5.0%	36.9	29.1	-35.3%
D19		125	69.2	-13.3%	36.9	59.9	33.1%

Taking the influence of different parameters into consideration, an ideal model of a 10 m high wind turbine tower model was obtained. The concrete filling ratio was 50%, since compared to 25% filled CFFT, it had better behaviour, and compared to 75% and 100% filled CFFT, it was more economic and lighter weighted; the hollow cavity is also needed as an electrical conduit. Two-thirds of fibres were aligned in the axial direction to provide better flexural performance while still providing some confinement to the concrete core. 2.3% steel reinforcement ratio and six prestressing tendons were used in the new model to improve the performance of the CFFT tower. The increase of taper ratio did not influence the load capacity and can decrease the use of concrete and FRP materials, so a 2% taper ratio was adopted. The tower base diameter and FRP tube thickness selected were 1000 mm and 10 mm, respectively, as they both have acceptable results.

4.3.2 Results for Parametric study Part B: Loading configuration

4.3.2.1 Different load distributions

Figure 4.27 (a) and (b) show the load-deflection curves and the moment deflection curves of models tested under different loading conditions. Deflections were obtained at the top of the tower models, while moments were the magnitude reaction moment obtained at the bottom of the tower models. The steel reinforcement was considered, so non-linear behaviour was obtained, which is the same as model D11 to D14. In brief, the model can resist highest uniform load and lowest concentrated load at the top of the tower model. Details are discussed below.

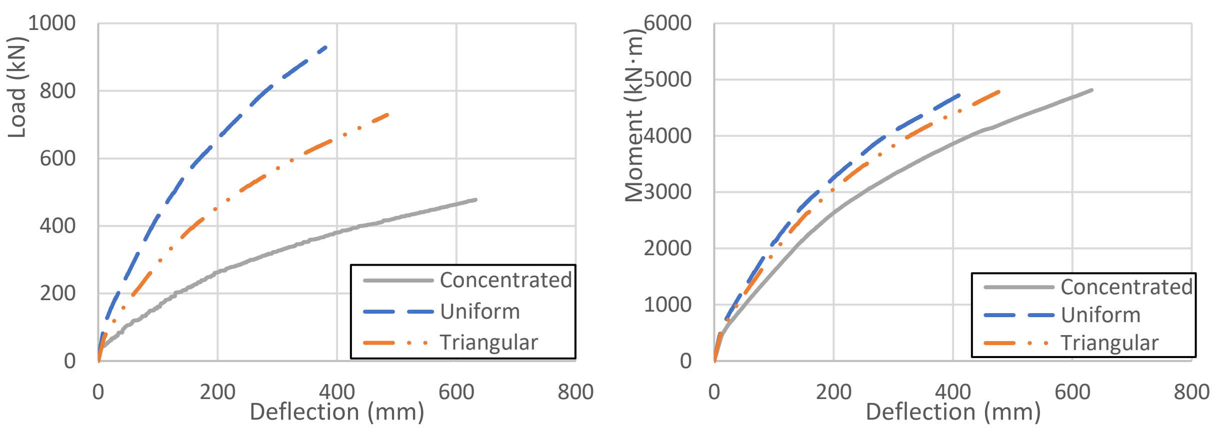

(a) (b)

Figure 4.27 Models L1, L2, and L3 (a) Load-deflection curve (b) Moment-deflection curve

The displacement distribution in the x- and z-direction was similar for models L1 to L3. Axial deflection increased at the tension side and decreased at the compression side, and the zero-deflection point was closer to the compression side, as shown in Fig. 4.28, as the positive deflection at the tension side was about two times the negative deflection at the compressive side. Figure 4.29 shows the strain distribution of models examined under concentrated load, uniform load, and triangular load. Results were obtained at the failure load. Maximum strain was observed at the tension side, and the high strain region was at the base of the tower models. The figures indicate that the model tested under concentrated load had a higher tensile strain near the mid-height of the tower than uniform loading and triangular loading models.

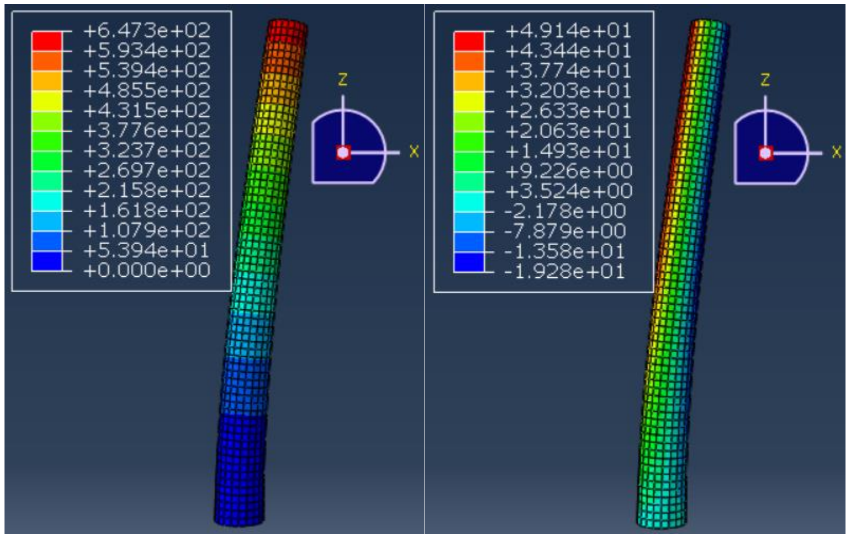

(a) (b)

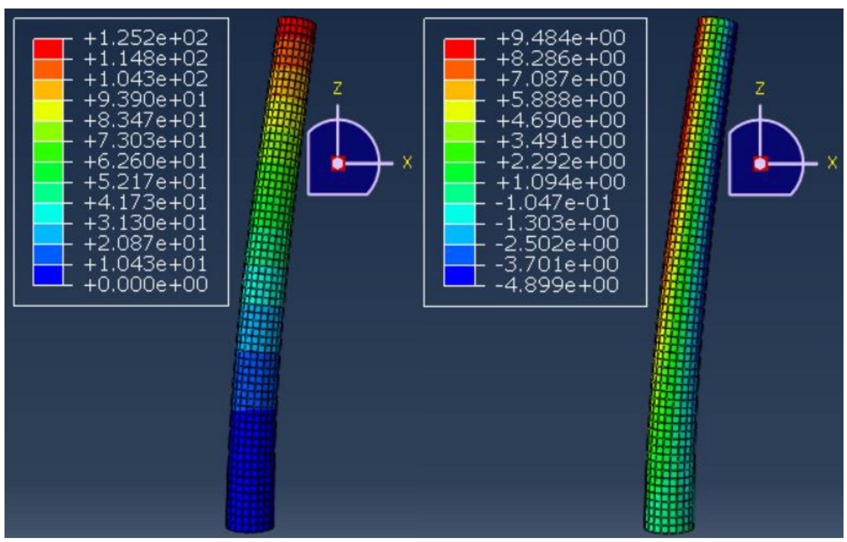

(c) (d)

Figure 4.28 Displacement (mm) distribution for model L1 (a) x-direction at failure (b) z-direction at failure (c) x-direction at deflection limit (d) z-direction at deflection limit

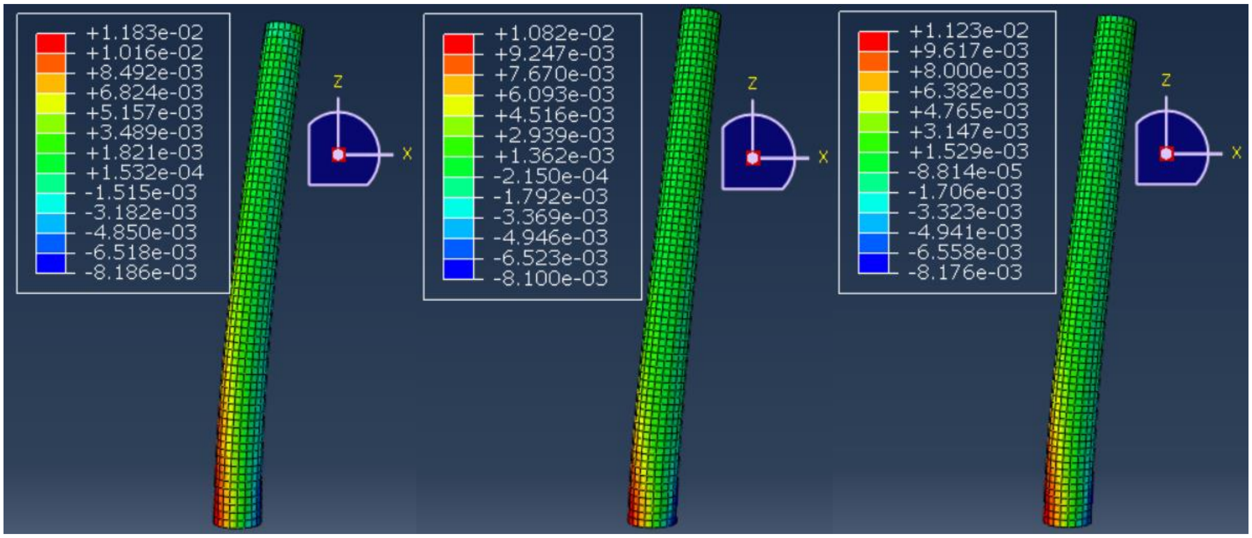

(a) (b) (c)

Figure 4.29 Strain distribution at failure for (a) Model L1 (b) Model L2 (c) Model L3

Figure 4.31 presents the strain distribution of the three tower models at the deflection limit. The distribution was similar to the results at failure, but the maximum tensile strain was about five times lower than the value at failure. Figures 4.30 (a) – (c) and (d) – (f) present the axial stress of steel reinforcing bars of models L1, L2, and L3 at failure and at deflection limit, respectively. At failure, both steel reinforcing bars at the tension side yielded for all three models. On the contrary, at the deflection limit, the bars in the models tested under uniform and triangular load still yielded, but steel bars in the model tested under concentrated load did not reach the yield stress. Moreover, for the uniform loading model, two bars yielded, but for the triangular loading model, only one bar yielded. The main reason for the difference in the three models is the applied load. Uniform or triangular applied load created higher stress in the steel reinforcing bar at the base of the tower models due to the load applied along the z-direction.

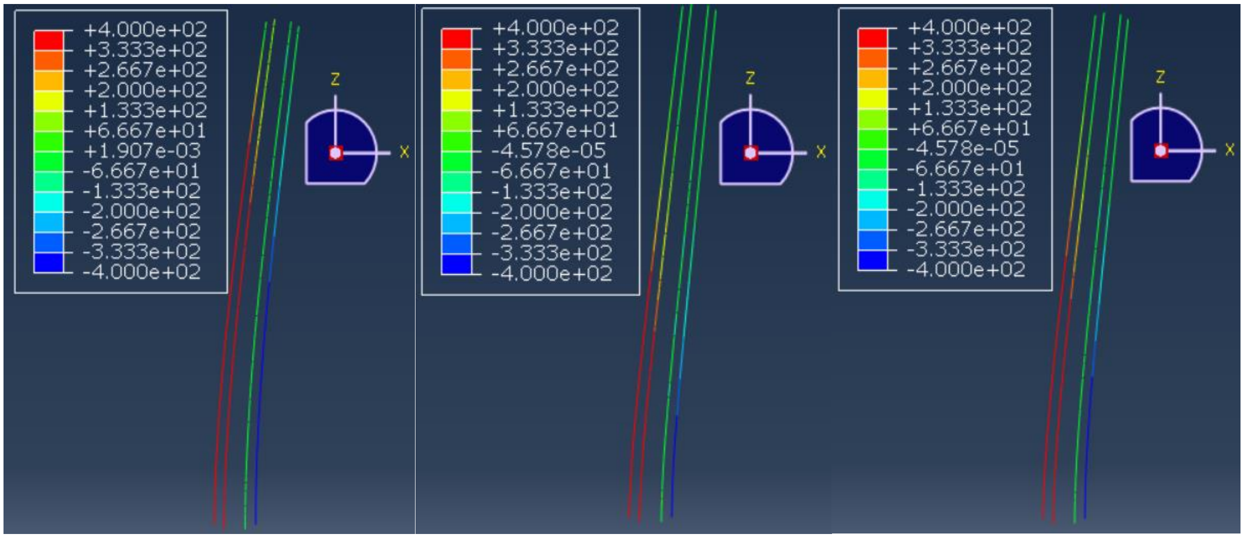

(a) (b) (c)

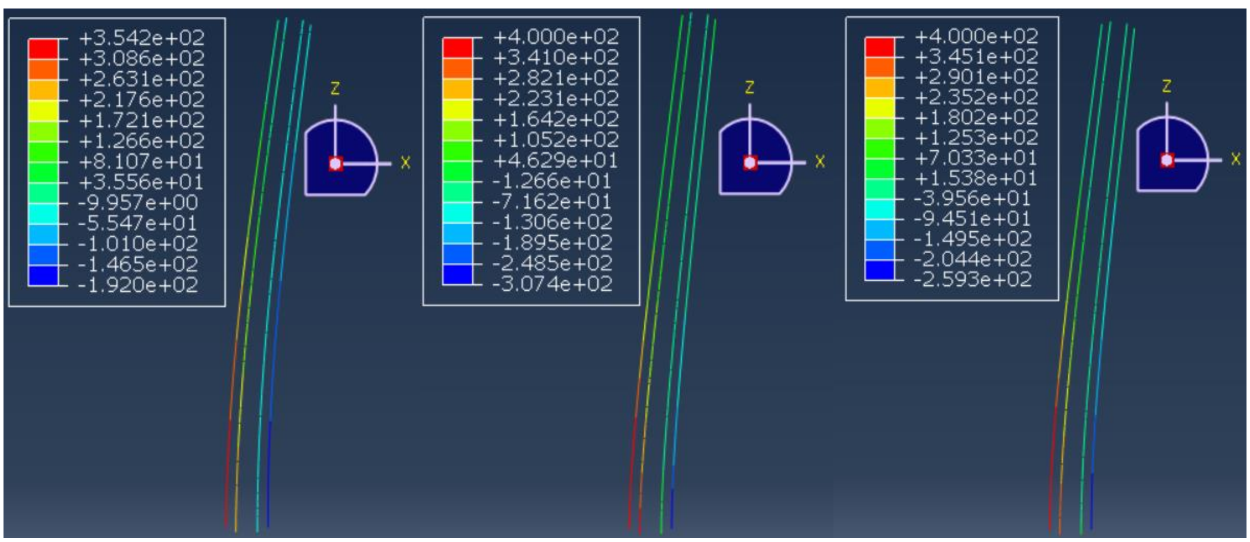

(d) (e) (f)

Figure 4.30 Axial stress (MPa) of steel reinforcing bars at failure of (a) Model L1 (b) Model L2 (c) Model L3 and at deflection limit of (d) Model L1 (e) Model L2 (c) Model L3

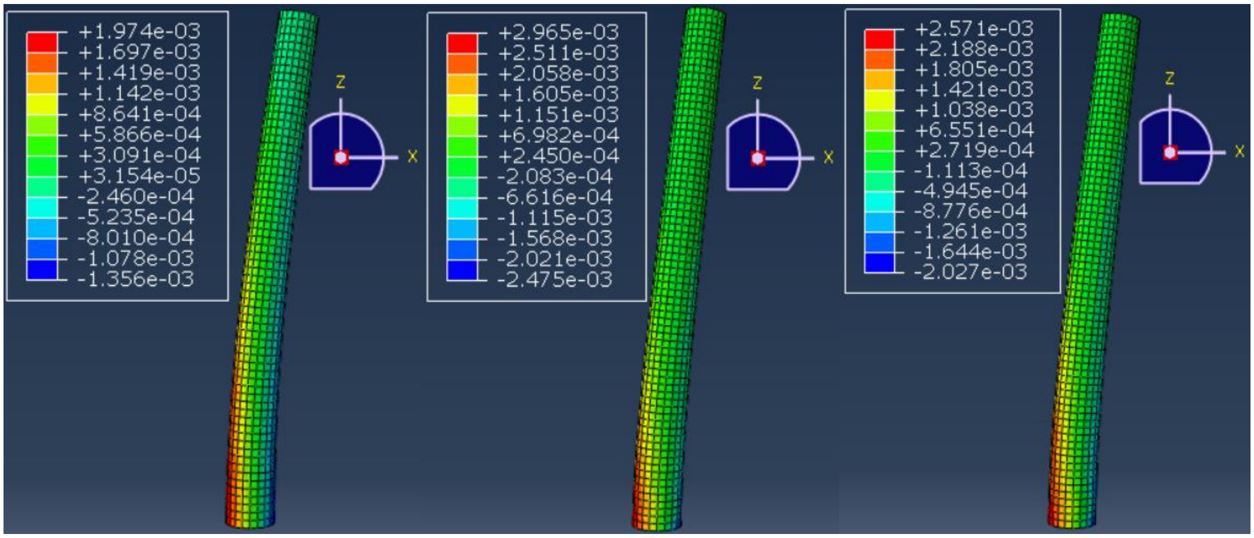

(a) (b) (c)

Figure 4.31 Strain distribution at deflection limit for (a) Model L1 (b) Model L2 (c) Model L3

Table 4.17 presents load and deflection results for models L1, L2, and L3. As presented in Fig. 4.27, model L2 under uniform load had the highest load capacity and the lowest stiffness. The load capacity of model L2 was 105.2% higher than the concentrated loaded model L1, and 34.4% higher than the triangular loaded model L3, while the maximum deflection was 33.4% and 13.0% lower than models L1 and L3. Similar trends are observed in load at deflection limit and displacement at service load. Models L2 and L3 have 160.4% and 77.9% higher load at the deflection limit, and 65.6% and 47.3% lower maximum displacement at the service load, respectively. The difference in the moment at failure for the three models is insignificant, since the increase or decrease is lower than 0.5%, but the moment of model L2 at the deflection limit is the highest, with a 28.5% and 8.3% increase, compared to models L1 and L3, respectively. The service load is much lower than loads at failure or deflection limit, so the moment at that point was not considered. To conclude, the model under concentrated loading condition had the lowest load capacity and stiffness. Although real wind turbine towers are subjected to a combination of concentrated and distributed wind loads, the concentrated load at the top of the tower is deemed more critical for design.

Table 4.17 Failure mode and details of models L1, L2, and L3

		L1	L2	L3
At failure	Load (kN)	477.5	980.0	728.9
	Compared to L1	/	105.2%	52.6%
	Def. (mm)	632.2	421.0	483.9
	Compared to L1	/	-33.4%	-23.5%
	Mom. (kN·m)	4775	4792	4825
	Compared to L1	/	-0.46%	0.23%
At deflection limit	Def. (mm)	125	125	125
	Load (kN)	190.5	496.0	338.9
	Compared to L1	/	160.4%	77.9%
	Mom. (kN·m)	1905	2448	2260
	Compared to L1	/	30.0%	20.0%
At service load	Load (kN)	34.1	34.1	34.1
	Def. (mm)	9.3	3.2	4.9
	Compared to L1	/	-65.6%	-47.3%

4.3.2.2 Different load eccentricities

Loads transferred from a wind turbine to the support tower include torsional moments that result from friction as the turbine changes directions. To investigate this effect, two eccentric load models were compared to concentric load model L1. Results confirmed that models tested under different eccentricities had similar load-deflection curves and moment deflection curves, as shown in Fig 4.32 (a) and (b). Overall, the load capacity, stiffness, and moment were similar for the three models with different load eccentricities. The moment in the z-direction (i.e. torsion) increases with the increase of load eccentricity, but the value was small enough, so the maximum magnitude bending moment of the three different tower models was still similar. Details are shown below.

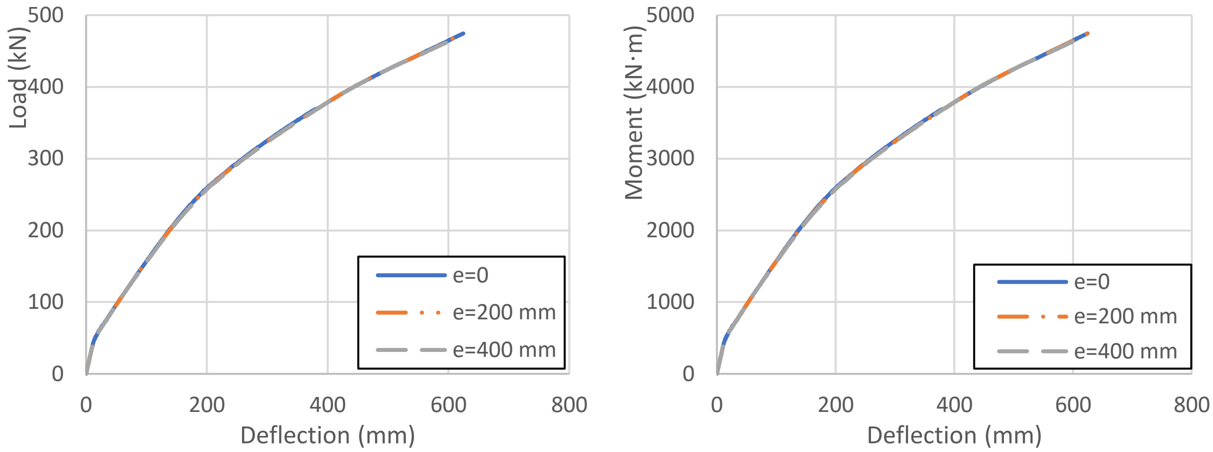

(a) (b)

Figure 4.32 Model L1, L4, and L5 (a) Load-deflection curve (b) Moment-deflection curve

The x- and z-direction displacement distribution for two eccentricity models at failure and at the deflection limit were similar to the concentricity model, L1, as shown in Fig. 4.28. The strain distribution of models with different eccentricities was similar as well. Figure 4.34 presents the strain distribution for model L5 at failure load and deflection limits. Compared to Fig. 4.29 (a) and Fig. 4.30 (a), it is clear that the model with 400 mm eccentricity had higher tensile strain at the two points. Figure 4.34 shows the axial stress of steel reinforcing bars and prestressing tendons of two eccentric models. Unlike the results for uniform or triangular loading, steel reinforcing bars in eccentric models had similar behaviour to bars in the concentric model L1. At failure, two bars in the tension side yielded, but at the deflection limit, yield stress was not reached for all the bars. Comparing Fig. 4.33 to Fig. 4.31 (a) and (d), it is clear that with the increase of load eccentricity, the maximum stress in the steel reinforcing bars decreased. 200-mm eccentric model had a 3.1% lower tensile stress, and 400-mm eccentric model had a 4.4% lower tensile stress than the concentric model.

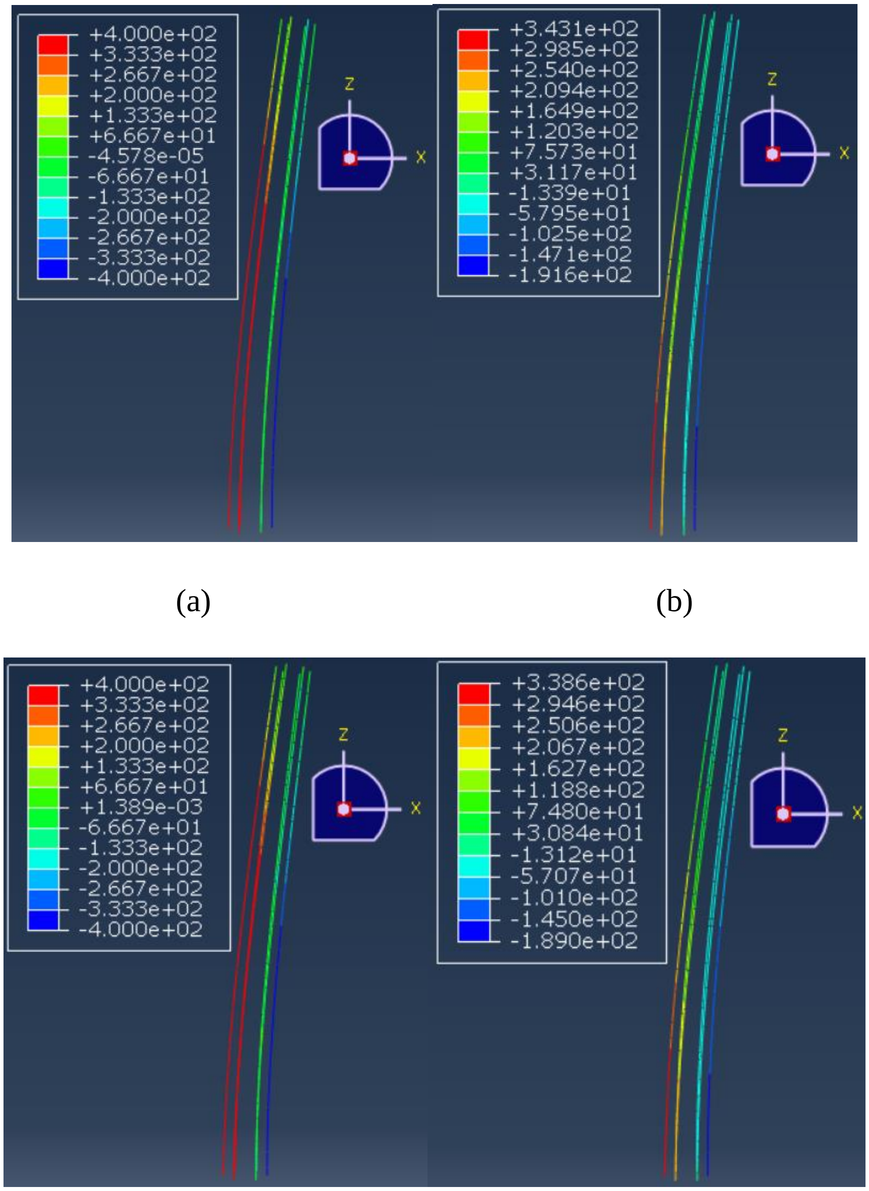

(a) (b)

(c) (d)

Figure 4.33 Axial stress (MPa) distribution of steel reinforcing bars (a) Model L4 at failure (b) Model L4 at deflection limit (c) Model L5 at failure (d) Model L5 at deflection limit

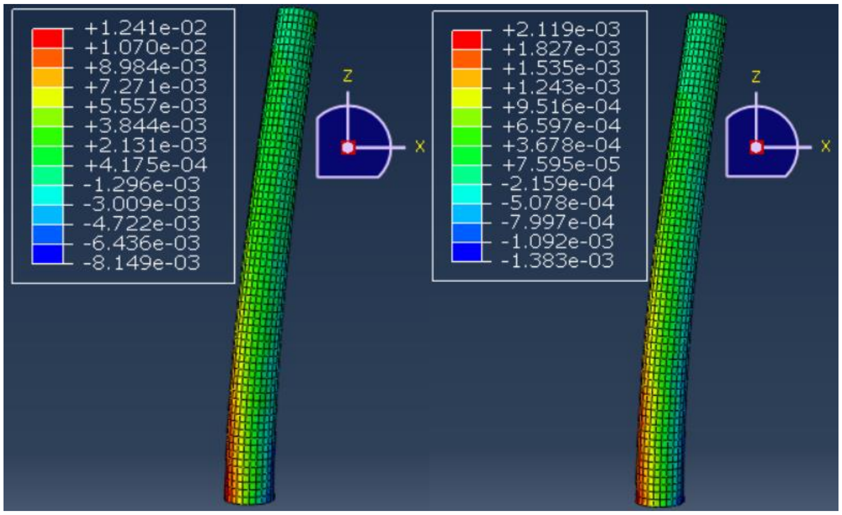

(a) (b)

Figure 4.34 Strain distribution for model L5 (a) At failure (b) At deflection limit

Though the eccentricity is different, models L1, L2, and L3 still have similar failure load, deflection, and bending moment, as shown in Table 4.18. Compared to model L1, the decline in CFFT model behaviour caused by load eccentricity is insignificant, as no more than 0.40% and 0.6% decrease is obtained in maximum load and deflection, respectively. The maximum moment also only decreased 0.3%, which is negligible. Besides, it is clear that results for models L4 and L5 are close to each other, which means, without axial load, the failure behaviour of CFFT models is not influenced significantly by small torsional moments. Table 4.18 also presents the failure mode, load and moment at the deflection limit, and deflection at the service load. Unlike the failure behaviour, eccentricity had a slight influence on CFFT models behaviour at the deflection limit and service load. A 2.7% decrease in load and moment are observed at the deflection limit when the eccentricity increased from zero to 200-mm. When the eccentricity keeps increasing, the load and moment keep decreasing. Model L5, with 400-mm eccentricity, had a 3.1% lower load moment than model L1. At the service load, deflection increased 3.2% and 4.3% for models L4 and L5, respectively. One possible reason for the different load and moment might be the deflection in y-direction that occurred due to the eccentricity. The moment in the z-direction was obtained due to the load eccentricity, but compared to the moment in the y-direction, the values are relatively small.

Table 4.18 Failure mode and details of models L4 and L5

		L4	L5
At failure	Load (kN)	475.7	475.6
	Compared to L1	-0.38%	-0.40%
	Def. (mm)	628.5	630.3
	Compared to L1	-0.59%	-0.30%
	Mom. (kN·m)	4759	4759
	Compared to L1	-1.2%	-1.2%
At deflection limit	Def. (mm)	125	125
	Load (kN)	185.4	184.6
	Compared to L1	-2.7%	-3.1%
	Mom. (kN·m)	1855	1847
	Compared to L1	-1.5%	-1.9%
At service load	Load (kN)	34.1	34.1
	Def. (mm)	9.6	9.7
	Compared to L1	3.2%	4.3%

4.3.2.3 Different axial loads

Although wind turbine towers are primarily subjected to bending from horizontal wind forces, gravity loads associated with the weight of the turbine and the tower itself should also be considered. Models tested under pure axial loads did not fail when the applied load was equal to or lower than 300 kN. Though model L8 had a 22.7% and 10.2% larger axial deflection than models L6 and L7, respectively, the axial deflection was still negligible, as shown in Table 4.19. It also shows that a 50% increase in axial load resulted in a 10% increase in the average compressive stress at the tower base. Figure 4.35 shows the displacement distribution and axial strain distribution for model L8. The figures indicate that the strain and deflection in the z-direction obtained under pure axial load are small when the load is lower than 300 kN, and thus implies that axial loading is not the main cause of failure in this study.

Table 4.19 Axial deflection of models L6, L7, and L8

	L6	L7	L8
Axial load (kN)	100	200	300
Axial deflection (mm)	0.617	0.687	0.757
Compressive stress at base (MPa)	1.87	2.08	2.30

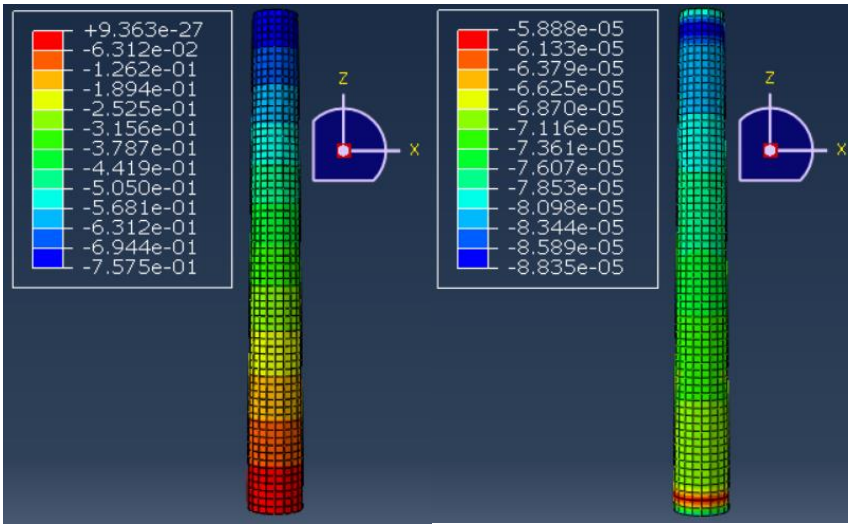

(a) (b)

Figure 4.35 Model L8 (a) Displacement distribution (mm) (b) Strain distribution

4.3.2.4 Different combined loads

Models L9 to L12 were tested under combined loads and were compared to model L1, which was tested under pure concentrated concentric horizontal load. Figure 4.36 shows the load-deflection relationships of the five models. The results for all four towers were similar, and details are presented and discussed below.

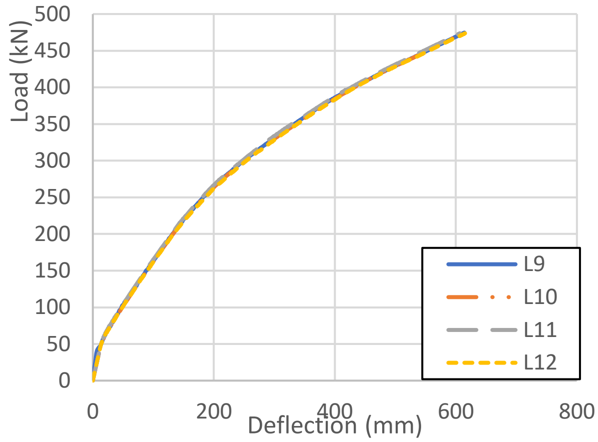

Figure 4.36 Models L9 to L12 Load-deflection relationship

The displacement distribution at failure and deflection limit for the four models were similar to model L1; details are shown in Table 4.17. Figure 4.37 shows the strain distribution of model L9 to L11 at failure load, and Fig. 4.38 shows the strain distribution at the deflection limit. The strain distribution contours were similar, and comparing models L9, L10, and L12, the increase in ultimate strain and strain at the deflection limit can be found when the eccentricity increases, and the axial load stayed the same. Comparing models L10 and L11, a 33.3% increase in axial load resulted in a 1.0% decrease in ultimate strain and a negligible change in maximum strain at the deflection limit, which again implies the change in axial load under 300 kN did not have a huge influence on CFFT tower behaviour. The four models had a similar steel axial stress distribution as model L1, which means at failure, both steel bars at the compression side yielded, and at the deflection limit, all the bars did not yield. The increase in load eccentricity decreased the steel tensile stress. Model L10 and L12 had 1.2% and 1.8% lower steel stress than model L9. The effect of axial load on steel reinforcing bar behaviour was insignificant as well. Figure 4.39 shows the steel axial stress distribution for model L9 at failure and deflection limit.

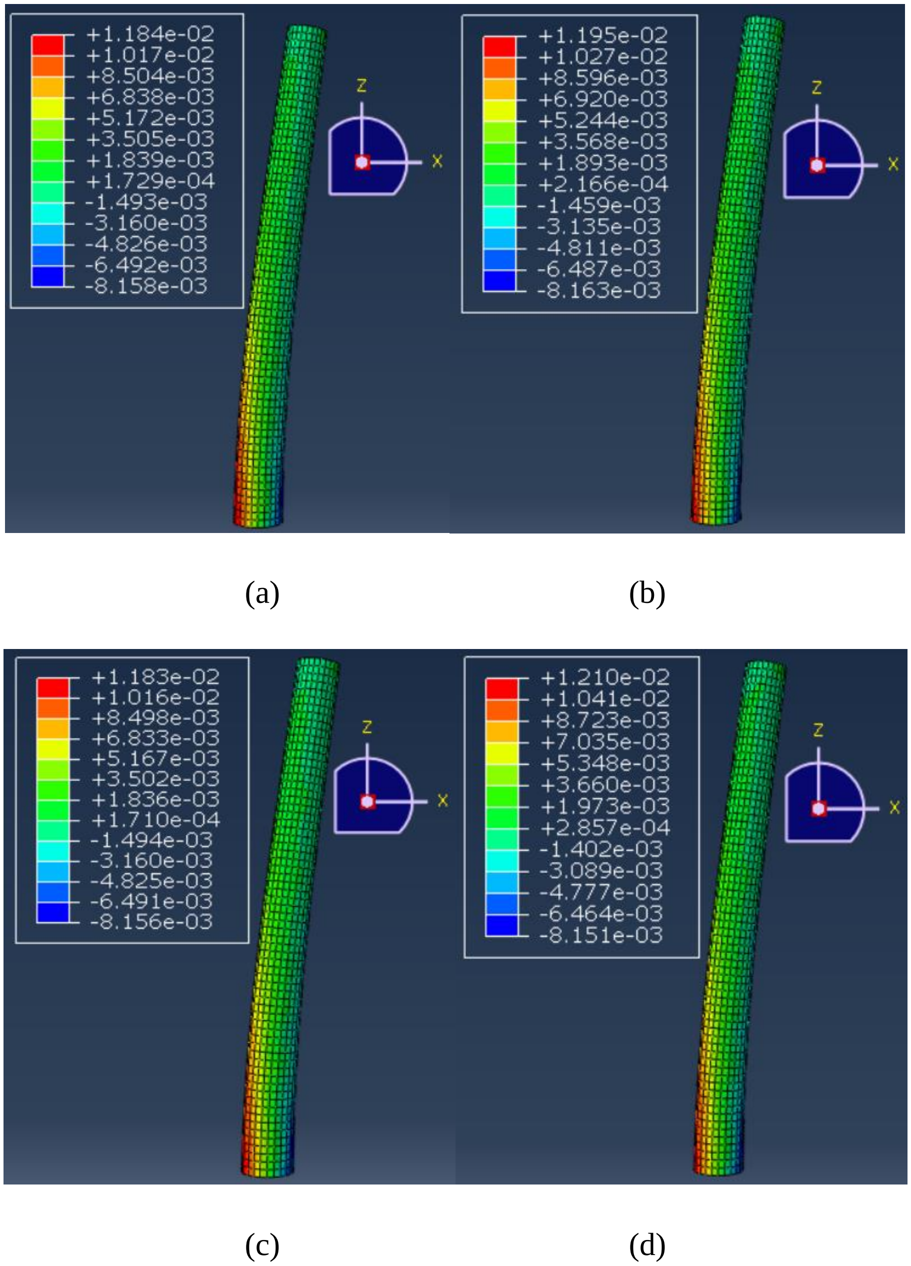

Figure 4.37 Strain distribution at failure (a) Model L9 (b) Model L10 (c) Model L11 (d) Model L12

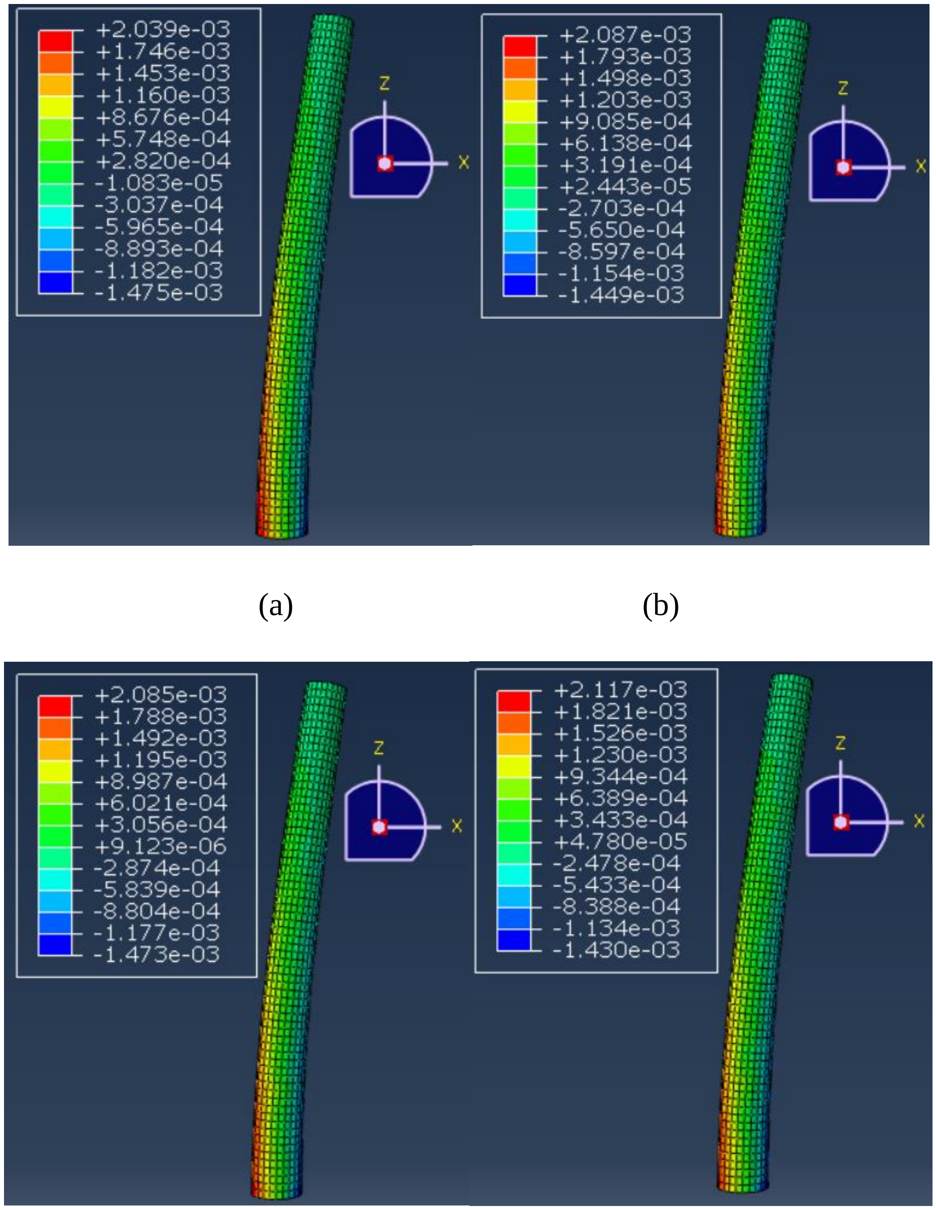

(c) (d)

Figure 4.38 Strain distribution at deflection limit (a) Model L9 (b) Model L10 (c) Model L11 (d) Model L12

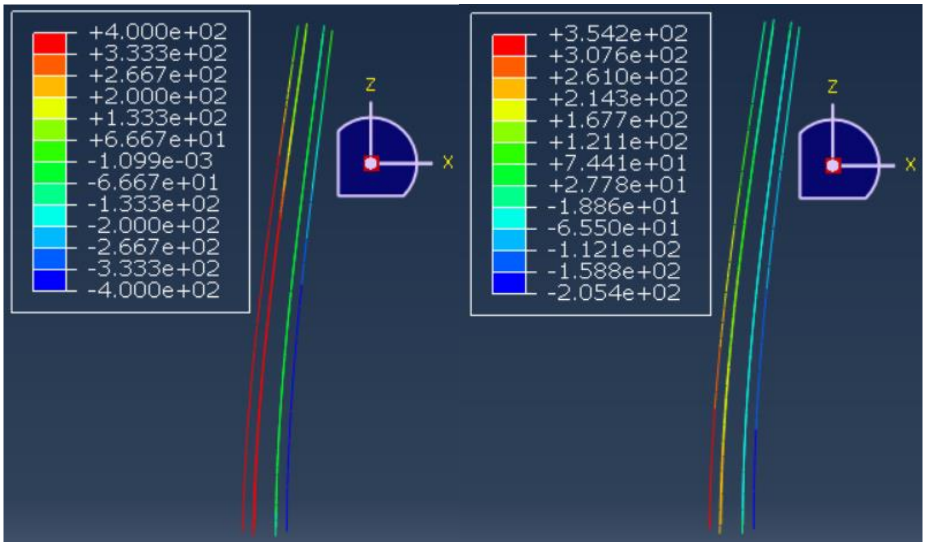

(a) (b)

Figure 4.39 Steel axial stress (MPa) distribution for Model L9 (a) at failure (b) at deflection limit

Table 4.20 presents the load and deflection results of models L9 to L12. Comparing model L9, which was tested under a 200 kN axial load as well as a concentrated concentric horizontal load, to model L1, it is found that the failure load of model L9 was only 0.59% lower than model L1, but the maximum deflection was 2.8% lower than model L1, which means the influence of axial load on load capacity was insignificant, but it had a small effect on CFFT tower deflection. The load at the deflection limit for model L9 was 0.5% higher than model L1, which indicates that at the deflection limit, with the increase of axial load, the CFFT tower model can resist higher lateral load. The same conclusion is drawn by comparing model L10 to model L11. They both had an eccentricity of 200 mm, but under 300 kN axial load, model L11 can resist 1.3% higher load than model L10 at the deflection limit. The possible reason is the extra stability and confinement provided by the axial load. Comparing models L9, L10, and L12, at failure, the load capacity and deflection did not change a lot with the increase of load eccentricity, which was the same as models tested under pure lateral load. At the deflection limit, the influence is still small, but a slight decrease in applied load was observed. At the service load, it is clear that increasing the load eccentricity increased the deflection significantly, as models L10 and L12 had 64.3% and 66.1% higher deflection than model L9, respectively. But model L11 had the same deflection as model L10, which indicates the axial load did not influence the deflection at service load. Comparing model L10 to model L11, the influence of axial load at the deflection limit can also been found. Contrary to the effect on deflection limit, the increase of axial load did not influence the deflection at service load and maximum load capacity at failure. The deflection at failure, though, decreased 0.96% with a 50% increase in axial load. Like the change in load capacity, the change in moment capacity is negligible as well. At the deflection limit, the moment capacity increased with the increase of axial load, as model L9 had 0.5% higher moment than model L1, and model L11 had 1.3% higher moment than model L10. It seems that increasing the load eccentricity will increase the effect of axial load on moment at the deflection limit. Overall, the influence of load eccentricity and axial load are not significant.

Table 4.20 Results for models under combined load

		L9	L10	L11	L12
	Axial load (kN)	200	200	300	200
At failure	Load (kN)	474.7	474.0	473.9	473.8
	Compared to L9	/	-0.15%	-0.17%	-0.19%
	Def. (mm)	614.2	612.5	606.6	615.3
	Compared to L9	/	-0.28%	-1.2%	0.18%
	Mom. (kN·m)	4747	4741	4740	4742
	Compared to L9	/	-0.1%	-0.1%	-0.1%
At deflection limit	Def. (mm)	125	125	125	125
	Load (kN)	191.4	188.6	191.1	185.8
	Compared to L9	/	-0.57%	0.31%	-1.1%
	Mom. (kN·m)	1914	1886	1911	1860
	Compared to L9	/	-1.5%	4.0%	-2.8%
At service load	Load (kN)	34.1	34.1	34.1	34.1
	Def. (mm)	5.6	9.2	9.2	9.3
	Compared to L9	/	64.3%	64.3%	66.1%

4.3.2.5 Different model sizes

Models L13 to L15 had different heights and diameters and were tested under concentrated concentric loads. Figure 4.40 shows the load-deflection relationships of these three models as well as model L1. The circular marks represent the service load, and the triangular marks represent the deflection limit. It is clear that for model L1 (h/D = 10) and L14 (h/D = 13.3), the service load was lower than the load at the deflection limit (i.e., over-designed); however, for model L13 (h/D = 16.7) and L15 (h/D = 20), the service load was larger than the load at the deflection limit (i.e., under-designed). The main reason for the difference is the different height-to-diameter ratio (h/D). Models L13 and L15 had a higher h/D ratio; in consequence, they had lower stiffness and resisted lower load at the deflection limit.

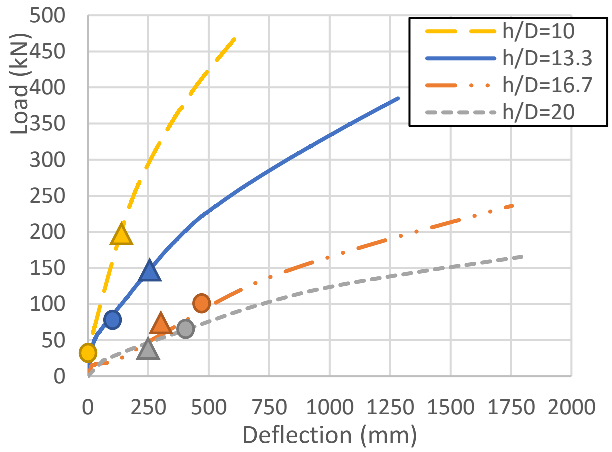

Figure 4.40 Load-deflection relationships of different model L1 and L13 to L15 (circle = service load, triangle = deflection limit)

These models were tested under the same load condition as model L1, so they had similar FRP strain distribution and steel stress distribution at failure and deflection limit, as shown in Fig. 4.41.

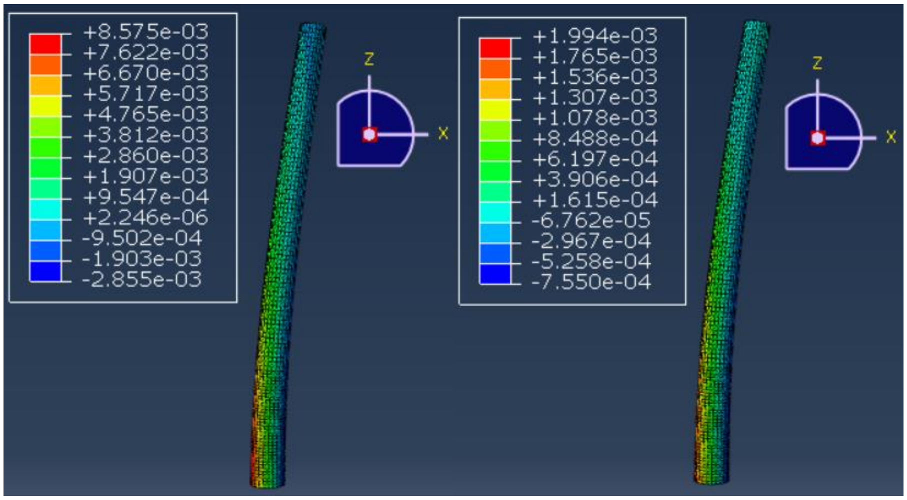

(a) (b)

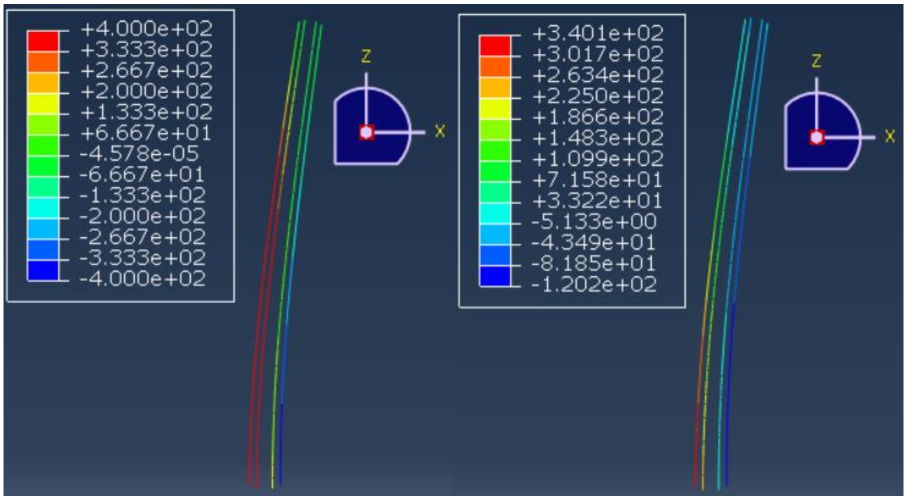

(c) (d)

Figure 4.41 model L14 (a) FRP strain distribution at failure (b) FRP strain distribution at deflection limit (c) Steel stress (MPa) distribution at failure (d) Steel stress (MPa) distribution at deflection limit

Table 4.21 presents the results for models L13, L14, and L15. With about 25% increase in h/D ratio, the failure load decreased about 32% and the maximum displacement at failure increased about 38%. At the deflection limit, the load capacity decreases with the increase of h/D ratio, though the deflection limit was only affected by the model height. Comparing the four models, the results indicated that when the h/D ratio increased 33%, 26%, and 20%, respectively, the load at the deflection limit decreased 23%, 59%, and 22%. The moment was influenced by the tower height and load capacity at the same time, so the relationship between the h/D ratio and moment is not linear. At the service load, which is influenced by the height and diameter at the same time, the increase in h/D ratio did not lead to an increase in deflection in all cases, since the service loads were different for each model.

Table 4.21 Results for models with different h/D ratio

		L13	L14	L15
	h/D ratio	16.7	13.3	20
At failure	Load (kN)	263.2	384.9	165.4
	Compared to L1	-44.6%	-18.9%	-65.2%
	Def. (mm)	1764.8	1282.4	1792.9
	Compared to L1	187.3%	108.8%	191.9%
	Mom. (kN·m)	6580	7700	3310
	Compared to L1	37.8%	61.3%	-30.7%
At deflection limit	Def. (mm)	312.5	250	250
	Load (kN)	59.3	146.3	46.3
	Compared to L1	-69.3%	-24.2%	-76.0%
	Mom. (kN·m)	1483	2926	927
	Compared to L1	-22.2%	53.6%	-51.3%
At service load	Load (kN)	96.8	79.2	59.4
	Def. (mm)	500.1	89.6	362.9
	Compared to L1	5277%	863%	3802%

4.3.3 Results for Parametric study Part C: Tower type

4.3.3.1 Concrete tower models

The reinforced concrete models experienced flexural failure near the base of the model at the tension side due to steel reinforcement yielding followed by concrete crushing. Figure 4.42 shows the load-deflection curves of two concrete tower models and the CFFT tower model L1. The difference between the two concrete models were the number of prestressing tendons, and model L1 had the same concrete and steel reinforcement parameters as model C1 but included the external FRP tube. Results of model L1 were non-linear, while results for the two concrete models were closer to bi-linear curves. The CFFT model had a higher load capacity and maximum deflection than the two concrete models.

Table 4.22 presents the failure mode and details for the two concrete models. It is clear that increasing the number of prestressing tendons can increase the load capacity as well as stiffness. Model C2 had a 2.4% higher maximum load and 29.1% lower maximum deflection than model C1. Compared to model L1, C1 and C2 had 53.7% and 52.6% lower load capacity and 44.9% and 60.9% lower deflection at failure. Both concrete models failed due to steel reinforcing bar yielding. For model C1, it resisted 22.0% lower load than model L1 at the deflection limit; for model C2, it resisted 9.2% lower load than model L1. The service load was much lower than the load capacity, but the two concrete models also had about 10% higher service deflection than the CFFT model. Model C1 and C2 had similar stress and strain distribution of concrete and steel reinforcing bars. Figure 4.43 shows the stress and strain distribution of concrete and the stress distribution of steel reinforcing bars for model C2. The concrete first cracked at the tension side, then, the tensile steel reinforcing bars yielded, finally, the concrete at the compression side crushed and the concrete failed.

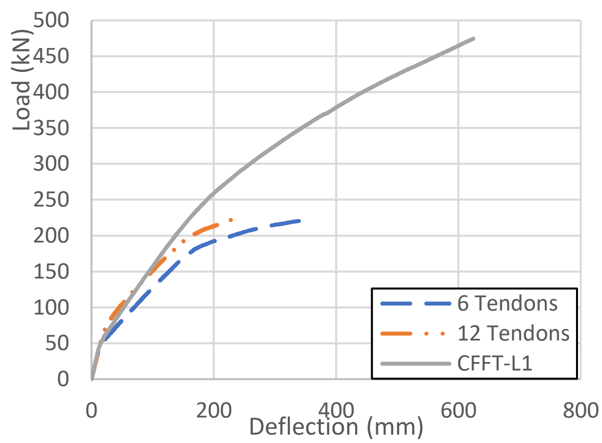

Figure 4.42 Load-deflection relationships of models L1, C1, and C2

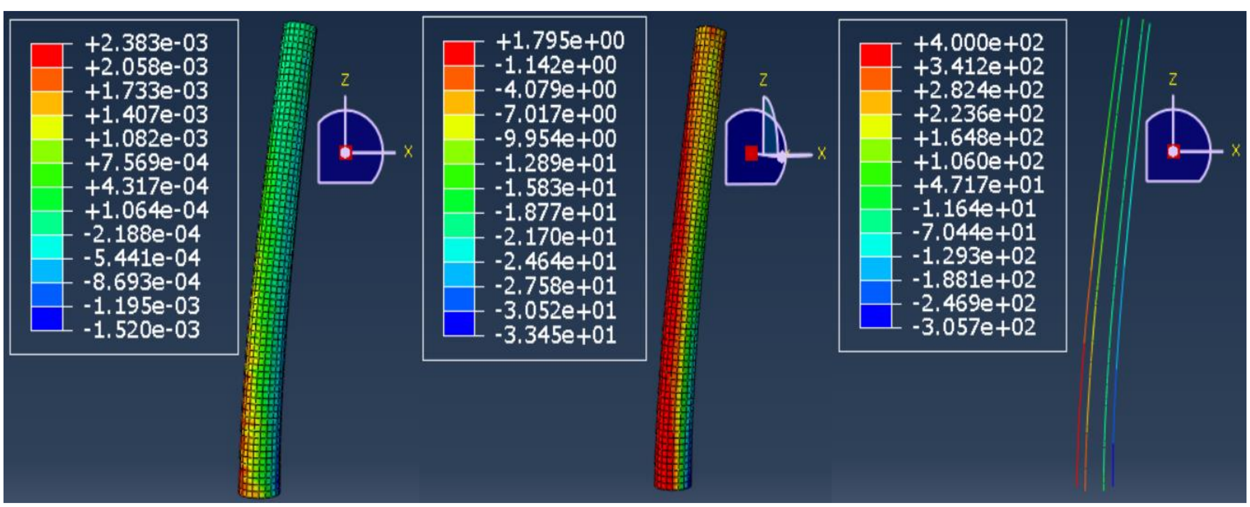

(a) (b) (c)

Figure 4.43 Model C2 (a) Concrete strain distribution (b) Concrete stress (MPa) distribution (c) Steel stress (MPa) distribution

Table 4.22 Results of concrete tower models

	C1	C2
F_{max} (kN)	221.0	226.2
D_{max} (mm)	348.4	246.9
Failure mode	Flexural failure	Flexural failure
Deflection limit (mm)	125	125
F_{lim} (kN)	148.5	172.9
Service load (kN)	34.1	34.1
D_{ser} (mm)	10.0	9.83

4.3.3.2 Steel tubular tower models

When the Von Mises stress reached the ultimate tensile strength of steel, it is considered that failure occurred. The Von Mises stress distribution of model S1 at failure is presented in Fig. 4.44 (a).

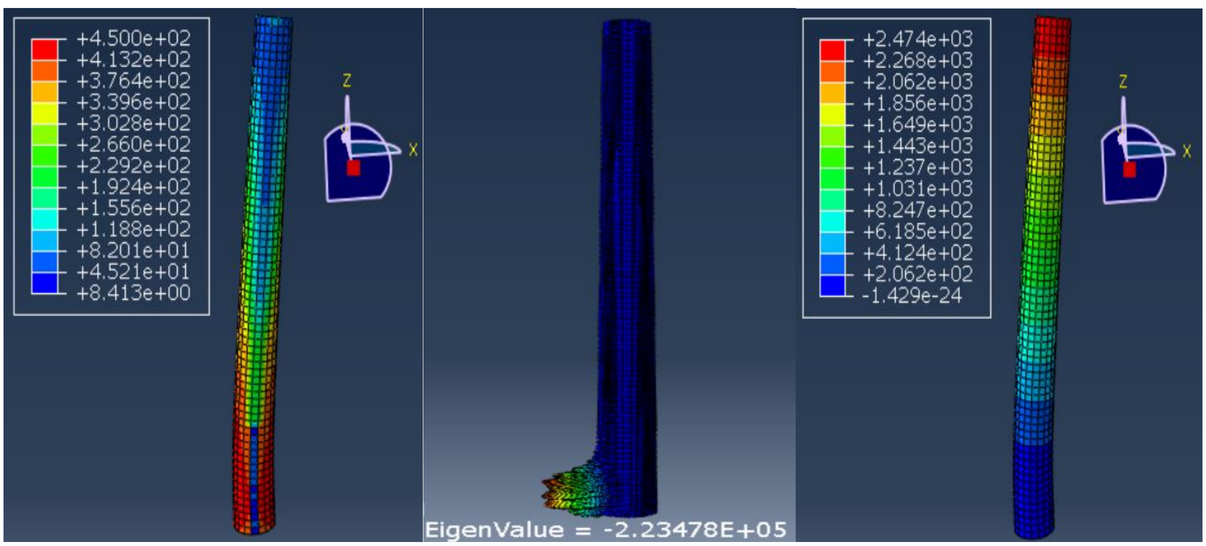

(a) (b) (c)

Figure 4.44 Model S1 (a) Von Mises stress (MPa) distribution (b) Buckling (c) Deflection (mm) in x-direction

The buckling test results of steel tower model S1 are shown in Fig. 4.44 (b). It indicated that for model S1, the local buckling load was 46.5% lower than the failure load, but for model S2, buckling load was slightly higher, and for model S3, buckling load was much higher than the failure load; this implies that model S1 failed due to buckling, while model S2 and S3 are considered to reach failure when the Von Mises stress reached the ultimate tensile strength. Figure 4.44 (c) presents the deformed shape of model S1 at the strength limit, assuming that local buckling can be prevented with the addition of transverse stiffeners (at an increased cost). Figure 4.45 shows the load-deflection curves of the steel tubular wind turbine towers with different wall thicknesses as well as the results of the CFFT tower model L1. The buckling load for models S1 and S2 is presented in the figure as well. Models with 20-mm and 30-mm wall thickness had similar maximum deflection, while the model with 10-mm wall thickness had about 34% higher ultimate deflection than the other steel tower models. Considering buckling, model S1 had 71.2% and 80.3% lower maximum load than models S2 and S3; however, the maximum load of model S2 was only 31.7% lower than model S3. At the deflection limit, model S1 had reached the buckling load already, which means the model failed before reaching the deflection limit. Before the first yielding of the steel, model S3 had higher stiffness than model S2, as the deflection at service load was 32.0% lower and load at deflection limit was 48.5% higher. After yielding, the two curves had a similar slope.

Compared to steel tubular models, the CFFT model L1 was safer than model S1 since the CFFT model did not have a local buckling problem. Comparing the CFFT model to steel tubular models, it is clear that the CFFT model had a non-linear load-deflection curve, while the steel models had bilinear load-deflection curves, which means model L1 did not have a sudden change in deformed shape before it failed. At failure, model L1 had a 114% higher load capacity than model S1, and 38.4% lower load capacity than model S2. At the deflection limit, model S1 had failed due to buckling, but the CFFT model can resist 190.5 kN load safely. At the service load, model L1 had a 50.3% lower deflection than model S1, and comparing to model S2, the deflection was only 4.3% lower. Table 4.23 shows the failure mode and details of the three steel tubular tower models.

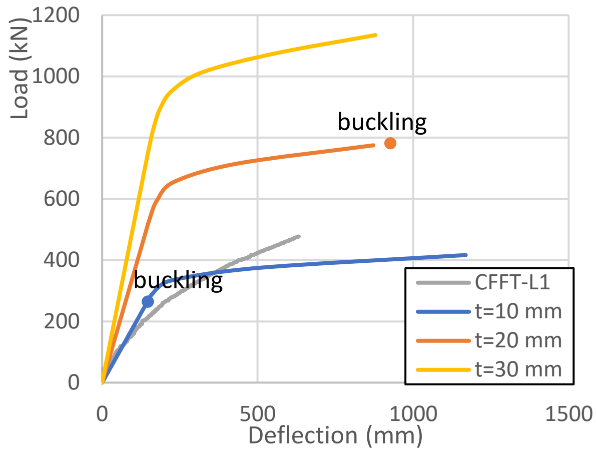

Figure 4.45 Load-deflection relationships of steel tower models and model L1

Table 4.23 Results of steel tubular tower models

	S1	S2	S3
F_{max} (kN)	417	775	1135
D_{max} (mm)	1169.0	872.0	878.8
Buckling load (kN)	223	795	1809
Failure mode	Buckling	Strength failure	Strength failure
Deflection limit (mm)	125	125	125
F_{lim} (kN)	225	431	640
Service load (kN)	34.1	34.1	34.1
D_{ser} (mm)	18.7	9.7	6.6

4.3.3.3 Tower weight calculation

The weight of concrete, steel tubular, and CFFT wind turbine towers is calculated and compared to each other. These values are relevant for transportation and erection considerations. The weight of two concrete towers and three steel tubular towers is listed below, along with the CFFT tower model L1, which had a similar geometric shape as the concrete towers.

The material weights necessary for the calculation are shown in Table 4.24.

Table 4.24 Material weights

Material	Weight
Concrete	2400 kg/m^3
30 M steel reinforcing bar	5.495 kg/m
45 M steel reinforcing bar	11.775 kg/m
Seven-wire strand prestressing tendon	1.109 kg/m
Steel	7850 kg/m^3
GFRP	2580 kg/m^3

The weights of the concrete wind turbine tower models C1 and C2 were calculated. The volume of the concrete wind turbine towers, and weights of concrete, steel reinforcing bars, and weight of prestressing tendons were required for the calculation and are listed in Table 4.25.

Table 4.25 Weights and volumes of concrete tower models

	C1	C2
Concrete volume (m^3)	3.05	3.05
Concrete weight (kg)	7320	7320
Bar’s length (m)	60	60
Bars’ weight (kg)	707	707
Tendons’ length	60	120
Tendons’ weight (kg)	67	133
Total weight (kg)	8094	8160

To obtain the weight of steel tubular towers, the volumes of steel walls of models S1, S2, and S3 were required. Table 4.26 presents the parameters necessary for the calculation.

Table 4.26 Weights and volumes of steel tower models

	S1	S2	S3
Volume (m^3)	0.29	0.56	0.83
Weight (kg)	2277	4396	6516

The weight of the CFFT wind turbine tower model L1 consists of two parts: the inner concrete core and the outer FRP tube. The inner concrete core had the same weight as concrete tower model C1, presented above. The additional weight of the GFRP tube is presented in Table 4.27.

Table 4.27 Weights and volumes of CFFT tower models

	L1
Concrete core (kg)	8094
GFRP volume (m^3)	0.28
GFRP tube (kg)	722
Total weight (kg)	8816

Figure 4.46 compares the load-deflection response for models L1, C2, and S1, which all had fairly similar overall geometries and performance at service. It is noted that the CFFT model had the highest load capacity and ultimate deflection of these selected models. Model C2 had 7.4% lower weight than model L1 but had 52.6% and 60.9% lower maximum load and deflection, respectively. At the deflection limit, though model C2 had a higher prestressing level than model L1, it still had 9.2% lower load capacity. Results indicate that CFFT is only slightly heavier than the concrete tower, and therefore the foundation requirements would be similar; however, it has better overall performance and requires less inner reinforcement. It is also important to note that the concrete cover used in the models was only 40 mm since the FRP tube provides excellent protection against corrosion. In the absence of the FRP tube, this cover may need to be increased which reduces the structural efficiency of the tower and increases the weight. Further optimization of the CFFT design for specific loading conditions is also possible. Meanwhile, model S1 failed before the deflection limit due to local buckling and had a 51.2% lower maximum load than model L1. Steel towers are lighter than concrete and CFFT towers, but they are less durable and can be difficult to transport. On the contrary, lightweight FRP tubes can be transported easier to site and work as stay-in-place formwork, so CFFTs can be filled on site and reduce the use of temporary concrete formwork.

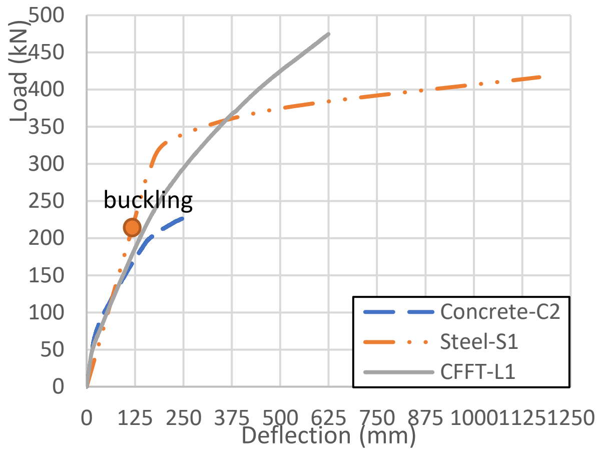

Figure 4.46 Load-deflection relationship of models L1, C2, and S1

Based on the results presented in this chapter, a preliminary design of a CFFT wind turbine tower is recommended to have the following characteristics to meet design criteria:

- h/D ratio of approximately 15
- Taper ratio of 2%
- Concrete filling ratio of 50%
- GFRP tube thickness of 10 mm
- Steel reinforcement ratio of 2%

Once the preliminary design is complete, the prestressing level and other parameters can be refined based on the calculated wind loads and other salient factors such as location and turbine size. In addition to its structural performance, the CFFT tower system is expected to be a durable and low maintenance alternative for wind energy in remote areas.

Chapter 5 Conclusions and future work

5.1 Conclusions

Two hollow tubes, four CFFT beams, and four CFFT stubs were tested by Fam (Fam, 2000). The difference between the hollow tubes were the FRP laminate structure; the difference between the beams and stubs included the tube thickness, concrete strength, laminate structure, and geometric shapes. These FRP tubes and CFFTs were modelled using commercial software ABAQUS for the validation portion of this study. A comprehensive parametric study was then conducted, and wind turbine tower models were developed to test the effect of different geometric shapes and load scenarios. This study is the first to use finite element modelling to investigate the feasibility of CFFTs for wind turbine towers.

5.1.1 Model validation

Chapter 3 provides the experimental and finite element analysis details of selected FRP tube and CFFTs. Here are the conclusions:

- Finite element results of the hollow beam models agree with experimental results well, as well as small CFFT beams under bending tests; for larger beams, the error occurred due to the concrete slip; this can be prevented in practice by using methods to add friction and therefore the results were considered satisfactory.
- For the stubs, good agreements were found using displacement-controlled models, though the strain results for hollow stubs were slightly larger than experimental results. In summary, the finite element method is capable of modeling CFFTs under axial or bending loads.

5.1.2 Models tested under different geometry and reinforcement

Chapter 4 provides the finite element analysis results of wind turbine towers with different parameters. The following conclusions were made:

- Increasing the model base diameter, FRP tube thickness, steel reinforcement ratio, prestressing ratio, and fibre orientation in the longitudinal direction can increase the load capacity and stiffness at failure, deflection limit, and service load. Decreasing the model height has the same effect on CFFT cantilever models.

- The taper ratio only influences the stiffness of CFFT models and does not affect the load capacity.
- The increase of concrete filling ratio is an effective method to improve the behaviour of CFFT models when it is lower than 50%; however, when over 50% of the CFFT is filled with concrete, the improvement in load capacity begins to decline, and only has an insignificant influence on the stiffness.

5.1.3 Models tested under different loading configurations

Chapter 4 also provides the finite element analysis results of wind turbine towers under different loading conditions. Conclusions were made as follows:

- Towers subjected to uniform load conditions can resist the highest total load, and the deflection at failure also decreased. The load case corresponding to a concentrated load applied at the top surface resulted in the lowest load capacity and the highest deflection.
- For CFFT models under pure lateral load, eccentricity does not have a huge influence on the behaviour at failure, deflection limit, and service load.
- The weight of a small wind turbine is relatively small compared to the lateral load and does not have significant influence on model behaviour under pure axial load.
- The increase of axial load improves the performance of CFFT models under combined load slightly. The load eccentricity, like models tested under pure lateral load, does not have a significant influence on model performance.

5.1.4 Models with different h/D ratio

Chapter 4 presents the finite element analysis results of wind turbine towers with different height and base diameter. Here are the conclusions:

- The increase of h/D ratio decreases the load capacity and increases the maximum displacement at failure.
- Though the deflection limit differs due to different model heights, the load at deflection limit decreases with the increase of h/D ratio.

- The service load depends on the height and the diameter at the same time, so the deflection at service load is not necessarily proportional to the increase of h/D ratio. A ratio of approximately 15 is suitable for preliminary design purposes.

5.1.5 Models using different tower types

Chapter 4 conducted the analysis for concrete and steel cantilever models under concentrated lateral load.

- With the same prestressing level and geometry, the CFFT model has better behaviour in load capacity, stiffness, and safety compared with other tower types. Thin-walled steel tubular models have local buckling problems, but the CFFT model is free from the problem, which makes the CFFT model also safer than the steel tubular model. Although durability was not explicitly considered in this study, the superior properties of FRP materials suggest that CFFT towers would also have a longer service life than other systems.

5.2 Future work

This research focused on the influence of tower and FRP wall geometric details and internal steel reinforcement. This study can be conducted in different aspects to obtain the effect on the behaviour of CFFT wind turbine towers of different variables. The possible aspects of future work are shown below:

- Future investigation on the influence of different concrete strengths on CFFT wind turbine towers. Studies can be focused on the difference of NSC and HSC under the same and different confinement ratio to examine how the concrete strength affects the CFFT wind turbine tower behaviour under different confinement ratios.
- Future investigation on the influence of different types of internal reinforcing bars. CFRP reinforcing bars, GFRP reinforcing bars, and steel reinforcing bars have different material properties and stress-strain relationship, so the reinforcing bar types may affect the performance of CFFT wind turbine towers.
- Future investigation on the influence of different FRP material types. This study focused on concrete-filled GFRP tube, but CFRP is also a widely used FRP material. Although

CFRP is more expensive than GFRP, it still has better performance and deserves to be tested. Optimization of fibre architecture (orientations other than [0/90] as well as different stacking sequences) is also recommended.

- Future investigation of wind turbine towers under complex loading systems. In this study, models were tested under different axial, horizontal and combined loads, but the real load conditions can be more complex. Studies can focus on wind turbine tower models under combined load with different load distribution and eccentricity. Models under different moments and torque can also be considered.
- Future investigation of wind turbine towers considering dynamic wind effects. This study only focused on static loading conditions, but the vibration and resonance frequencies may also influence the performance of wind turbine towers and need further study.
- Further investigation to optimize tower geometry for different sizes of wind turbines and tower heights.
- Development of design guidelines and simple analytical equations to facilitate implementation of CFFT wind turbine towers in remote areas.

References

Abdallah, M. H., Mohamed, H. M., & Masmoudi, R. (2018). Experimental assessment and theoretical evaluation of axial behavior of short and slender CFFT columns reinforced with steel and CFRP bars. *Construction and Building Materials*, *181*, 535–550. https://doi.org/10.1016/j.conbuildmat.2018.06.014

ACCIONA Windpower reaches 1,000 MW of wind turbines installed with concrete towers. (n.d.). Retrieved March 31, 2021, from https://www.acciona.com/updates/news/acciona-windpower-reaches-1000-mw-wind-turbines-installed-concrete-towers/

Ahmed, A. A., Hassan, M., & Masmoudi, R. (2020). Effect of concrete strength and tube thickness on the flexural behavior of prestressed rectangular concrete-filled FRP tubes beams. *Engineering Structures*, *205*. Scopus. https://doi.org/10.1016/j.engstruct.2019.110112

Al-Ilani, M., & Temsah, Y. (2019). Comparative study of modeling methods used to simulate initial stresses in prestressed beams towards manual analysis. *MATEC Web of Conferences*, *281*, 01014. https://doi.org/10.1051/matecconf/201928101014

Amir Mirmiran, M. S., Charle El Khoury, and Wassim Naguib. (2000). Large Beam-Column Tests on Concrete-Filled Composite Tubes. *ACI Structural Journal*, *97*(2). https://doi.org/10.14359/856

Burgoyne, C. (2009). *FIBRE REINFORCED POLYMERS – STRENGTHS, WEAKNESSES, OPPORTUNITIES AND THREATS*. 6.

Cao, Y., He, M., Ma, R., Yang, R., & Liang, F. (2020). Beam-column modeling and seismic fragility analysis of a prestressed segmental concrete tower for wind turbines. *Advances in Structural Engineering*, *23*(8), 1715–1727. https://doi.org/10.1177/1369433219900295

Chen, H., Xu, D., & Deng, X. (2021). Control for Power Converter of Small-Scale Switched Reluctance Wind Power Generator. *IEEE Transactions on Industrial Electronics*, *68*(4), 3148–3158. https://doi.org/10.1109/TIE.2020.2978689

Cole, B., & Fam, A. (2006). Flexural load testing of concrete-filled FRP tubes with longitudinal steel and FRP rebar. *Journal of Composites for Construction*, *10*(2), 161–171. Scopus. https://doi.org/10.1061/(ASCE)1090-0268(2006)10:2(161)

Dagher, H. J., Bannon, D. J., Davids, W. G., Lopez-Anido, R. A., Nagy, E., & Goslin, K. (2012). Bending behavior of concrete-filled tubular FRP arches for bridge structures. *Construction and Building Materials*, *37*, 432–439. https://doi.org/10.1016/j.conbuildmat.2012.07.067

de Lana, J. A., Júnior, P. A. A. M., Magalhães, C. A., Magalhães, A. L. M. A., de Andrade Junior, A. C., & de Barros Ribeiro, M. S. (2021). Behavior study of prestressed concrete wind-turbine tower in circular cross-section. *Engineering Structures*, *227*, 111403. https://doi.org/10.1016/j.engstruct.2020.111403

El-Nemr, A. M., Ashour, O., & Hekal, G. M. (2016). *Finite element modeling of confined concrete piles with FRP tubes in sandy soil under static loading*. 2122–2127. Scopus.

Fam, A., Cole, B., & Mandal, S. (2007). Composite tubes as an alternative to steel spirals for concrete members in bending and shear. *Construction and Building Materials*, *21*(2), 347–355. Scopus. https://doi.org/10.1016/j.conbuildmat.2005.08.016

Fam, A., & Mandal, S. (2006). Prestressed Concrete–Filled Fiber-Reinforced Polymer Circular Tubes Tested in Flexure. *PCI Journal*, *51*(4), 42–54. https://doi.org/10.15554/pcij.07012006.42.54

Fam, A., Pando, M., Filz, G., & Rizkalla, S. (2003). Precast Piles for Route 40 Bridge in Virginia Using Concrete Filled FRP Tubes. *PCI Journal*, *48*(3), 32–45. https://doi.org/10.15554/pcij.05012003.32.45

Fam, A., Schnerch, D., & Rizkalla, S. (2005). Rectangular Filament-Wound Glass Fiber Reinforced Polymer Tubes Filled with Concrete under Flexural and Axial Loading: Experimental Investigation. *Journal of Composites for Construction*, *9*(1), 25–33. https://doi.org/10.1061/(ASCE)1090-0268(2005)9:1(25)

Fam, A., & Son, J.-K. (2008). Finite element modeling of hollow and concrete-filled fiber composite tubes in flexure: Optimization of partial filling and a design method for poles. *Engineering Structures*, *30*(10), 2667–2676. Scopus. https://doi.org/10.1016/j.engstruct.2008.02.015

Fam, A. Z. (2000). *Concrete-filled fiber reinforced polymer tubes for axial and flexural structural members* [Ph.D. thesis]. The University of Manitoba.

Fam, A. Z., & Rizkalla, S. H. (2002). Flexural Behavior of Concrete-Filled Fiber-Reinforced Polymer Circular Tubes. *Journal of Composites for Construction*, *6*(2), 123. Business Source Complete.

Flisak, B., Fam, A. Z., & Rizkalla, S. H. (2001). FRP Tubes Filled with Concrete and Subjected to Combined Axial and Flexural Loads. *Construction and Materials Issues 2001*, 45–54. https://doi.org/10.1061/40591(269)6

Gwon, T. gyun (Tom). (2011). *Structural Analyses of Wind Turbine Tower for 3 kW Horizontal Axis Wind Turbine* [California Polytechnic State University]. https://doi.org/10.15368/theses.2011.159

Hadi, M. N. S., Khan, Q. S., & Sheikh, M. N. (2016). Axial and flexural behavior of unreinforced and FRP bar reinforced circular concrete filled FRP tube columns. *Construction and Building Materials*, *122*, 43–53. Scopus. https://doi.org/10.1016/j.conbuildmat.2016.06.044

Hain, A., Motaref, S., & Zaghi, A. E. (2019). Influence of fiber orientation and shell thickness on the axial compressive behavior of concrete-filled fiber-reinforced polymer tubes. *Construction and Building Materials*, *220*, 353–363. https://doi.org/10.1016/j.conbuildmat.2019.05.194

Hain, A., Zaghi, A. E., & Saiidi, M. S. (2019). Flexural behavior of hybrid concrete-filled fiber reinforced polymer tube columns. *Composite Structures*, *230*. Scopus. https://doi.org/10.1016/j.compstruct.2019.111540

Hawileh, R. A., Musto, H. A., Abdalla, J. A., & Naser, M. Z. (2019). Finite element modeling of reinforced concrete beams externally strengthened in flexure with side-bonded FRP laminates. *Composites Part B: Engineering*, *173*. Scopus. https://doi.org/10.1016/j.compositesb.2019.106952

JCSS. (2005). *Probabilistic Model Code, PART III – RESISTANCE MODELS*. Joint Committee on Structural Safety.

Khan, Q. S., Sheikh, M. N., & Hadi, M. N. S. (2017). Axial-Flexural Interactions of GFRP-CFFT Columns with and without Reinforcing GFRP Bars. *Journal of Composites for Construction*, *21*(3). Scopus. https://doi.org/10.1061/(ASCE)CC.1943-5614.0000771

Khan, Q. S., Sheikh, M. N., & Hadi, M. N. S. (2018). Concrete Filled Carbon FRP Tube (CFRP-CFFT) columns with and without CFRP reinforcing bars: Axial-flexural interactions.

Composites Part B: Engineering, *133*, 42–52. Scopus. https://doi.org/10.1016/j.compositesb.2017.09.025

Khan, Q. S., Sheikh, M. N., & Hadi, M. N. S. (2020). Experimental results of circular FRP tube confined concrete (CFFT) and comparison with analytical models. *Journal of Building Engineering*, *29*, 101157. https://doi.org/10.1016/j.jobe.2019.101157

Khedmati, M., Nouri, Z., & Roshanali, M. (2012). A comparative computational investigation on the effects of randomly distributed general corrosion on the post-buckling behaviour of uniaxially loaded plates. *Journal of Mechanical Science and Technology*, *26*. https://doi.org/10.1007/s12206-011-1222-1

Knowles, J. (2016). *Power Shift: Electricity for Canada's Remote Communities*. 76.

Mander, J. B., Priestley, M. J. N., & Park, R. (1988). Theoretical Stress-Strain Model for Confined Concrete. *Journal of Structural Engineering*, *114*(8), 1804–1826. https://doi.org/10.1061/(ASCE)0733-9445(1988)114:8(1804)

Masmoudi, R., & Abouzied, A. (2018). Flexural Performance and Deflection Prediction of Rectangular FRP-Tube Beams Fully or Partially Filled with Reinforced Concrete. *Journal of Structural Engineering*, *144*(6), 04018067. https://doi.org/10.1061/(ASCE)ST.1943-541X.0002055

Mirmiran, A., & Shahawy, M. (1996). A new concrete-filled hollow FRP composite column. *Composites Part B: Engineering*, *27*(3–4), 263–268. https://doi.org/10.1016/1359-8368(95)00019-4

Mirmiran, A., & Shahawy, M. (1997). Behavior of Concrete Columns Confined by Fiber Composites. *Journal of Structural Engineering*, *123*(5), 583–590. https://doi.org/10.1061/(ASCE)0733-9445(1997)123:5(583)

Mirmiran, A., Shahawy, M., & Beitleman, T. (2001). Slenderness Limit for Hybrid FRP-Concrete Columns. *Journal of Composites for Construction*, *5*(1), 26–34. https://doi.org/10.1061/(ASCE)1090-0268(2001)5:1(26)

Mohamed, H. M., & Masmoudi, R. (2010). Flexural strength and behavior of steel and FRP-reinforced concrete-filled FRP tube beams. *Engineering Structures*, *32*(11), 3789–3800. Scopus. https://doi.org/10.1016/j.engstruct.2010.08.023

Natural Resources, C. (2017, October 6). *Renewable-energy-facts*. Natural Resources Canada. https://www.nrcan.gc.ca/science-data/data-analysis/energy-data-analysis/energy-facts/renewable-energy-facts/20069

Nicholson, J. C. (2011). *Design of wind turbine tower and foundation systems: Optimization approach* [Master of Science, University of Iowa]. https://doi.org/10.17077/etd.bhnu76gr

Ozbakkaloglu, T. (2013a). Compressive behavior of concrete-filled FRP tube columns: Assessment of critical column parameters. *Engineering Structures*, *51*, 188–199. Scopus. https://doi.org/10.1016/j.engstruct.2013.01.017

Ozbakkaloglu, T. (2013b). Concrete-filled FRP tubes: Manufacture and testing of new forms designed for improved performance. *Journal of Composites for Construction*, *17*(2), 280–291. Scopus. https://doi.org/10.1061/(ASCE)CC.1943-5614.0000334

Ozbakkaloglu, T., & Oehlers, D. J. (2008). Concrete-filled square and rectangular FRP tubes under axial compression. *Journal of Composites for Construction*, *12*(4), 469–477. Scopus. https://doi.org/10.1061/(ASCE)1090-0268(2008)12:4(469)

Park, J.-H., Jo, B.-W., Yoon, S.-J., & Park, S.-K. (2011). Experimental investigation on the structural behavior of concrete filled FRP tubes with/without steel re-bar. *KSCE Journal* *of Civil Engineering*, *15*(2), 337–345. Scopus. https://doi.org/10.1007/s12205-011-1040-0

Popovics, S. (1973). A numerical approach to the complete stress-strain curve of concrete. *Cement and Concrete Research*, *3*(5), 583–599. https://doi.org/10.1016/0008-8846(73)90096-3

Raza, A., Rehman, A. ur, Masood, B., & Hussain, I. (2020). Finite element modelling and theoretical predictions of FRP-reinforced concrete columns confined with various FRP-tubes. *Structures*, *26*, 626–638. https://doi.org/10.1016/j.istruc.2020.04.033

Ren, W., Sneed, L. H., Yang, Y., & He, R. (2015). Numerical Simulation of Prestressed Precast Concrete Bridge Deck Panels Using Damage Plasticity Model. *International Journal of Concrete Structures and Materials*, *9*(1), 45–54. https://doi.org/10.1007/s40069-014-0091-2

Rhoads-Weaver, H., Schwartz, S. S., Zarowny, K., Weis, T., Whittaker, S., Gluckman, M., & French, M. (2013, March 2). *Small Wind TurbinePurchasing Guide*. https://web.archive.org/web/20130302211547/http://www.ontario-sea.org/Storage/39/3065_Small_Wind_Turbine_Purchasing_Guide_-_Off-grid%2C_Residential%2C_Farm_%26_Small_Business_Applications.pdf

Shafiei, A., Dehkordi, B. M., Farhangi, S., & Kiyoumarsi, A. (2016). Overall power control strategy for small-scale WECS incorporating flux weakening operation. *IET Renewable Power Generation*, *10*(9), 1264–1277. https://doi.org/10.1049/iet-rpg.2015.0409

Son, J.-K., & Fam, A. (2008). Finite element modeling of hollow and concrete-filled fiber composite tubes in flexure: Model development, verification and investigation of tube parameters. *Engineering Structures*, *30*(10), 2656–2666. Scopus. https://doi.org/10.1016/j.engstruct.2008.02.014

Tsai, S. W., & Wu, E. M. (1971). A General Theory of Strength for Anisotropic Materials. *Journal of Composite Materials*, *5*, 58–80.

Van Den Einde, L., Zhao, L., & Seible, F. (2003). Use of FRP composites in civil structural applications. *Construction and Building Materials*, *17*(6–7), 389–403. https://doi.org/10.1016/S0950-0618(03)00040-0

Veljkovic, M., Feldmann, M., Naumes, J., Pak, D., Simões, L., da Silva, & Rebelo, C. (2011). 9—Wind turbine tower design, erection and maintenance. In J. D. Sørensen & J. N. Sørensen (Eds.), *Wind Energy Systems* (pp. 274–300). Woodhead Publishing. https://doi.org/10.1533/9780857090638.2.274

Vincent, T., & Ozbakkaloglu, T. (2013). Influence of fiber orientation and specimen end condition on axial compressive behavior of FRP-confined concrete. *Construction and Building Materials*, *47*, 814–826. Scopus. https://doi.org/10.1016/j.conbuildmat.2013.05.085

Vincent, T., & Ozbakkaloglu, T. (2015a). Influence of Slenderness on Stress-Strain Behavior of Concrete-Filled FRP Tubes: Experimental Study. *Journal of Composites for Construction*, *19*(1), 04014029. https://doi.org/10.1061/(ASCE)CC.1943-5614.0000489

Vincent, T., & Ozbakkaloglu, T. (2015b). Compressive Behavior of Prestressed High-Strength Concrete-Filled Aramid FRP Tube Columns: Experimental Observations. *Journal of Composites for Construction*, *19*(6), 04015003. https://doi.org/10.1061/(ASCE)CC.1943-5614.0000556

Wang, W., Sheikh, M. N., Hadi, M. N. S., Gao, D., & Chen, G. (2017). Behaviour of concrete-encased concrete-filled FRP tube (CCFT) columns under axial compression. *Engineering Structures*, *147*, 256–268. Scopus. https://doi.org/10.1016/j.engstruct.2017.05.061

Yu, B. C., Gai, H. B., & Li, Y. Y. (2013). A Kind of New Type Composite Structure Column of Research. *Advanced Materials Research*, *634–638*, 2653–2656. https://doi.org/10.4028/www.scientific.net/AMR.634-638.2653